Doctoral Dissertation

Doctoral Program in Sustainable Materials, Processes and Systems for Energy Transition (38^{th}cycle)

Study of sustainable materials and processes for energy transmission and storage devices

"DM 352 – Italian Recovery and Resilience Plan (RRP), European Union and the NextGenerationEU initiative"

By

Umar Farooq

******

Supervisor(s):

Prof. Luciano.Scaltrito., Supervisor

Luigi Costa, Co-Supervisor

Prof. Leonardo Marchese, Co-Supervisor

Doctoral Examination Committee:

Dr. Denis Perrone, Center for Sustainable Future Technologies, (IIT), Italy

Dr. Simone Luigi Marasso, IMEM, National Research Council (CNR), Italy

Politecnico di Torino

2026

This doctoral thesis was written at the end of the PhD programme in

"Materials, Sustainable Processes and Systems for the Energy Transition"

funded on the **PNRR, Missione 4, Componente 2 "Dalla Ricerca all'Impresa" – Investimento 3.3**

"*Introduzione di dottorati innovativi che rispondono ai fabbisogni di innovazione delle imprese* e promuovono l'assunzione dei ricercatori dalle imprese",

tramite il **Decreto Ministeriale n. 352 of 9 aprile 2022.**

CUP: E12B22000920005

Developed in collaboration between:

Politecnico di Torino (DISAT) and Università del Piemonte Orientale (DiSIT),
with Mista SpA.

Declaration

I hereby declare that, the contents and organization of this dissertation constitute my own original work and does not compromise in any way the rights of third parties, including those relating to the security of personal data.

Umar Farooq
2026

* This dissertation is presented in partial fulfillment of the requirements for **Ph.D. degree** in the Graduate School of Politecnico di Torino (ScuDo).

This thesis is lovingly dedicated to my peer Ghaus-e-Azam Sheikh Abdul Qadir Jillani (R.A), to my parents and my family, whose quiet sacrifices and constant encouragement made every step of this journey possible.

Acknowledgements

I owe my most sincere thanks to **Prof. Luciano Scaltrito**, my supervisor, for his patience and liberal guidance offered during all the different stages of this work. There were points in time when he could've doubted my ideas, but he didn't, and instead encouraged me at those moments in uncertainty, which made a permanent difference.

I am also thankful to **Prof. Sergio Ferrero** and **Prof. Valentina Bertana** at Chilab-ITEM Laboratory, DISAT, Politecnico di Torino for their scientific advice and constant support throughout the development of all the research projects. Their perspectives often helped me see the work from a better and more practical angle.

My sincere thanks are directed to **Luigi Costa**, **Simone Bigaran**, **Luca Costa**, **Domenico Cantarelli**, and **Roberto Meda** at **Mista S.p.A., Italy**, for their generous contributions in terms of technical support and willingness to share their hands-on experience during the research studies. It was thanks to their cooperation that it became possible to link laboratory research and industrial reality. I am equally grateful to the engineers and technicians at **Microla Optoelectronics Srl** whose assistance in the execution of many of the experimental tests was critical to the advancement of this work.

I would like to also thank **Prof. Davide Beneventi** from the **LGP^2 laboratory, Université Grenoble Alpes, France**, for hosting me during my stay in his group and for acting as the advisor during this period. The months that I spent at LGP^2 working on bio-based graphene electronics were both scientifically rewarding and/or personally memorable.

Lastly, I would like to thank all my colleagues and friends at Chilab - ITEM, Politecnico di Torino for the conversations, the challenges shared and the moments of encouragement that made these years a lot easier by making demanding phases of research much easier to cope with.

Abstract

The shift towards sustainable electric mobility has further increased the efforts in research in advanced materials and integrated component design in electric vehicle (EV) battery systems. This doctoral work examines four interrelated subsystems in the EV battery pack taking into consideration materials and design strategies that improve structural, electrical, as well as environmental performance.

The first investigation (https://doi.org/10.3390/polym17081056) involved modification of lightweight carbon fiber composite (CFRP) using multi-walled carbon nanotubes (MWCNTs) treated with an ionic liquid as an additive process to the structure. Two forms of MWCNTs (Pristine, and nickel coated) were used; each was mixed into the resin in the amount of one to three percent by weight. Before mixing, both types of nanotubes were treated with 5 wt% of ionic liquid dissolved in ethanol to enhance the level of their interaction with the material around them. The sample with 3 wt% of ionic liquid treated pristine MWCNTs exhibited the optimum mechanical response and the closest values for flexural strength, nearly 803 MPa and modulus, at nearly 88 GPa, while its storage modulus was close to 18 GPa. During testing, a slight non-linear response was observed at mid-span deflection, suggesting more effective load transfer across the fiber–matrix interface. The reduced electrical resistance of approximately 29 Ω indicates the formation of conductive networks, confirming the multifunctional potential of the developed laminates.

The second project (https://doi.org/10.1016/j.est.2025.120036) focused on copper busbars role to enhance the safety of energy transmission and storage devices. Electric-vehicle batteries rely on current-carrying components that are expected to be kept safe in situations requiring fast charging and rapid acceleration, which are factors that lead to elevated temperature, increased mechanical loading and the straining of electrical joints. A single digital model was developed to understand these effects in combination of electrical, thermal, magnetic and structural behavior. The model was used with copper busbars that operated from 100 to 500 A and were supported by finite element simulations and experimental measurements. The results showed stable behavior till approx. 200 A, voltage drops between 0.009 and 0.047 V, contact resistance between 12.4 and 18.7 micro-ohms and magnetic fields between 8 and 40 mT, all within the limits stated in IEC 60269-1, IEC 61439-1 and CISPR 25. High current loads (500 A) resulted in localized heat in the vicinity of 273 °C, as well as permanent deformation in excess of 1 mm, that indicated demands for thicker sections, integrated cooling and laminated layouts. Three sizes of copper

busbars were investigated, and both the simulations and experimental tests proved that all designs fulfilled the structural and working requirements. The work provides an evaluated digital model associating simulations with physical behavior and potentially helping to determine busbars for safer and more reliable battery system designs for use in future electric vehicles.

The third study (https://doi.org/10.3390/s25216778) examined the performance of reed sensors designed for vibration-prone environments . Reed sensors are used widely in electric vehicles because they can help to enhance safety and operative stability, and the performance is impacted by how they react to magnetic fields during movement and vibration. A set of tests were conducted to determine the switching distances of the sensor when placed in front of five different positions of a cylindrical magnet using a test fixture made with 3D printing. From the analysis it was concluded that the right and slightly upward position of the magnet gave the most favorable result, as the release distance was reduced and the switching was more even. A housing prototype was then produced using Selective Laser Sintering using polybutylene terephthalate and a stainless steel spring was incorporated to increase sensitivity and provide a stable operation. The spring reduced the activation distance to around 2.3 mm, which was up to sixty-percent improvement, and it also made the measurements more repeatable. The results indicate a realistic path for the development of reed sensors that can be used more reliably in challenging automotive applications.

The final investigation was a sustainable approach to creating simple electronic component by forming laser-induced graphene on a layer of paper coated with a thin layer produced from Lignin. The coating mixtures were made with softwood kraft lignin grades EKWZ and SWWZ from Lignoboost AB as a main source of carbon and nine different mixtures were made by varying the amount of 4-hydroxymethylfurfural, urea, propylene glycol and formaldehyde. Each of the additives had a specific function for, assisting removal of water during the heating process, bonding within the coating, flexibility, and making the mixture stable during the processing. When a low-power CO_2 laser ran over the coated paper, the surface layer turned into a conductive porous carbon pattern. Optimized mixture and laser settings were able to print patterned tracks with a sheet resistance lower than one hundred ohms per square of material, and the tracks were set into the shapes of an interdigitated array that functioned as small capacitors. The coated paper also remained smooth after processing, and there were no apparent cracks in the smeared regions, which indicates that the method may extract a wider area and more complicated layouts. This approach opens a route to the simple and flexible electronics from natural sources, and may benefit future applications of paper-based sensors, miniaturized energy storage components and inexpensive circuit elements on which environmental impact is of little concern.

The above four investigations are a unified path for developing battery systems with high performance, combined with modular architecture and low environmental. The outcomes indicate a use of lighter structural parts, more stable sensing parts, better current-carrying parts and electronics manufactured out of renewable sources, providing support for current objectives within the electric-vehicle sector. The results also demonstrate how material selection, device

architecture, and digital modeling can work together to increase the reliability while being able to reduce the overall footprint of the 3D fabrications for battery systems used in the future.

Contents

List of Figures **xiii**

List of Tables **xvii**

List of Abbreviations **xviii**

1 Introduction and Theoretical Scope **1**

1.1 Global Energy Transition and Electric Mobility 1

1.2 Problem Statement 2

1.3 Research Objectives 2

1.4 Literature Review 3

1.4.1 Materials for Lightweight, Functional Enclosures 3

1.4.2 Power Distribution and Electromagnetic Compatibility 5

1.4.3 Sensing in Vibration-Prone Environments 6

1.4.4 Low-Impact Flexible Electronics 8

1.5 Thesis Structure 8

2 Experimental Methods and Instrumentation **10**

2.1 Fabrication and Characterization of CFRP Nano-composites (*Project 1*) 10

2.1.1 Materials 10

2.1.2 Ionic Liquid Functionalization of MWCNTs 11

2.1.3 Laminate Fabrication via Vacuum Bagging 11

2.1.4 Characterization Techniques 12

2.2 Digital Twin Modeling and Experimental Evaluation of Copper Busbar (*Project 2*) 13

2.2.1 Materials and Busbars Configurations 13

2.2.2 Laser Welding and Metallurgical Characterization 13
2.2.3 Digital Twin Model Construction 14
2.2.4 Experimental Characterization 14
2.2.5 Data Correlation and Model Verification 15
2.3 Reed Sensor Fabrication and Testing (*Project 3)* 16
2.3.1 Design Concept and Materials 16
2.3.2 Fabrication Process 16
2.3.3 Performance Testing Protocol 17
2.4 Laser-Induced Graphene (LIG) on Bio-polymer Coated Substrates (*Project 4*) . 19
2.4.1 Materials and Coating Formulation 19
2.4.2 Laser Processing Parameters 20
2.4.3 Electrical and Micro-structural Characterization 20
2.4.4 Device Fabrication and Performance Testing 20
2.4.5 Environmental and Process Considerations 21

3 Results and Discussion 22
3.1 Mechanical and Functional Evaluation of CFRP Nanocomposites) 22
3.1.1 Flexural Performance 22
3.1.2 Dynamic Mechanical Analysis (DMA) 23
3.1.3 Electrical and Thermal Transport Behavior 26
3.1.4 Microscopic and Spectroscopic Analysis 29
3.1.5 Multifunctional Implications and Mechanistic Considerations 30
3.1.6 Summary 31
3.2 Electrical, Thermal, and Mechanical Analysis of Copper Busbars 31
3.2.1 Electrical Characterization and Voltage Distribution 32
3.2.2 Thermal and Thermo-Mechanical Behavior 33
3.2.3 Mechanical Testing and Microscopy 34
3.2.4 Contact Resistance 37
3.2.5 Summary 38
3.3 Evaluation and Optimization of Reed Sensors 38

3.3.1 Magnet Orientation and Switching Behavior . . . 39
3.3.2 Prototype Testing and Spring Integration . . . 40
3.3.3 Practical Integration and Design Considerations . . . 41
3.3.4 Summary . . . 42
3.4 Functional Evaluation of Laser-Induced Graphene (LIG) on Bio-Polymer Substrates . . . 43
3.4.1 Optimization of Laser Processing Parameters . . . 43
3.4.2 Influence of Coating Formulation on Conductivity . . . 44
3.4.3 Fabrication of LIG-Based Interdigitated Capacitors (IDC) . . . 46
3.4.4 Mechanistic Interpretation . . . 46
3.4.5 Summary . . . 47
3.5 Chapter 3 Summary . . . 47

4 System-Level Integration and Discussion 48
4.1 Functional Coupling Across Subsystems . . . 48
4.2 Comparative Performance Assessment . . . 48
4.2.1 Structural Integrity . . . 48
4.2.2 Electrical Efficiency . . . 49
4.2.3 Sensing and Control . . . 49
4.2.4 Sustainable Electronics . . . 49
4.3 Contribution in Modular Battery-Pack Architecture . . . 49
4.4 Durability, Reliability, and Scalability . . . 50
4.5 Sustainability and Life-Cycle Considerations . . . 50
4.6 Limitations and Opportunities . . . 51
4.7 Broader System Perspective . . . 51

5 Conclusions and Future Work 52
5.1 Overview . . . 52
5.2 Summary of Key Findings . . . 52
5.3 Integrated Contributions . . . 53
5.4 Limitations . . . 54

5.5 Recommendations for Future Work 54
5.6 Final Remarks 55

References **56**

List of Figures

2.1 Schematic of the fabrication route for CFRP nanocomposites showing ionic-liquid modification of MWCNTs, dispersion into the epoxy matrix, and subsequent laminate formation through vacuum-assisted resin infusion and curing. . 12

2.2 Type III copper busbars used for electromagnetic analysis, illustrating the three structural configurations (A–C) that vary in cavity placement and cross-sectional narrowing to influence magnetic-flux concentration and current distribution. . . 13

2.3 Experimental setup for magnetic-flux density measurements, showing the fixed-position Hall-effect sensor used to capture the field generated by Type III busbars carrying a controlled DC load. 15

2.4 FDM-printed prototype used for reed-sensor characterization, including the (a) magnet, (b) reed sensor, (c) linear sliders for displacement control, (d) & (e) the assembled test fixture designed for repeatable switching-distance measurement. 17

2.5 Spring-integrated reed-sensor testing setup: (a) UTM-based control of magnet displacement for precise switching-distance acquisition, (b) electrical verification circuit confirming contact closure and release, and (c) schematic of the reed sensor actuation and relaxation mechanism. 17

2.6 Five magnet-orientation configurations used in reed-switch evaluation, showing variations in (a) center-aligned (b) center-angled (c) center upward (d) right-shift-aligned (e) right-shift-upward, relative to the sensor to quantify alignment-dependent switching behavior. 18

2.7 Experimental arrangement for LIG formation on lignin-based coatings, showing the (a) air brush (b) bio polymers (c) masking system (d) air compressor, and (e) CO_2 laser etching process for formation of laser induced graphene on bio polymer coatings. 20

2.8 Process flow illustrating spray-coating of lignin formulations onto paper substrates, laser-induced graphitization, and post-treatment steps required to develop conductive LIG patterns. 21

3.1 Flexural strength and modulus values for all CFRP nanocomposites, highlighting the influence of ionic liquid treated pristine and nickel-coated MWCNTs content on stiffness and load-bearing capacity: (a) flexural strength; (b) flexural modulus. 23

3.2 Storage and loss modulus curves obtained from DMA, showing temperature-dependent viscoelastic response and the effect of IL-modified MWCNTs on the stiffness of CFRP laminates: (a) storage modulus (E'); (b) loss modulus (E''). . 24

3.3 Damping behavior of CFRP nanocomposites showing tan δ profiles and shifts in glass-transition region associated with nanotube dispersion and matrix–filler interactions. 25

3.4 Impedance spectroscopy results depicting (a) resistance, and (b) inductance, of CFRP samples alongside the (c) equivalent R–L circuit model, used to interpret frequency-dependent conduction behavior. 26

3.5 Thermal conductivity of CFRPs containing ionic-liquid-treated pristine MWCNTs measured at multiple temperatures, illustrating the effect of filler content on heat-transfer efficiency. 27

3.6 Thermal conductivity of CFRPs reinforced with IL-treated nickel-coated MWCNTs, showing how metal-coated nanotubes influence phonon transport within the composite. 28

3.7 SEM micrographs of fractured CFRP specimens showing voids at high filler loadings, improved resin wetting at optimal concentrations, and visible agglomerates of MWCNTs contributing to stiffness and conductivity variations: (a) voids in CFRPINi-3.0 wt%; (b) uniform epoxy impregnation in CFRPINi-1.5 wt%; (c) MWCNT agglomerates in CFRPIP-2.5 wt%; (d) magnified view of entangled MWCNTs within agglomerates. 29

3.8 FTIR spectrum of IL-treated MWCNTs showing characteristic absorption bands associated with the imidazolium cation, confirming successful surface functionalization. 30

3.9 Multiphysics simulation of the Type I laser-welded copper busbar showing (a) electric-potential distribution along the conductor and the resulting (b) magnetic-flux density generated under current loading. 32

3.10 Simulated magnetic-flux density maps for Type III busbars (A–C) at 40 A, illustrating the impact of cavity insertion and cross-section changes on field intensity near the surface: (a) Sample A with central cavity; (b) Sample B with solid geometry; (c) Sample C with narrowed solid geometry. 33

3.11 Thermal and thermo-mechanical responses of the Type I busbar under high-current operation showing localized Joule heating and resulting deformation predicted by the digital-twin model: (a) temperature rise due to Joule heating; (b) thermally induced deformation. 34

3.12 Three-point bending tests of Type I busbars comparing structural performance between unwelded and laser-welded regions, including differences in maximum load and yield behavior: (a, b) test setup; (c, d) comparison of maximum and yield forces for flat and welded regions. 35

3.13 Torsional loading of laser-welded busbars showing the test configuration and recorded torque–rotation response used to assess rotational stiffness and weld integrity. 36

3.14 Edge-bending experiment on laser-welded sections of the busbar showing load–displacement response and the influence of the weld zone on local flexibility: (a) test in progress; (b) bar chart comparing bending force required in welded sections. 36

3.15 Optical microscopy of etched Type I busbar cross-sections showing grain structures, small voids in the fusion line, and surface oxide features highlighted by differential-interference contrast imaging: (a, b) bright-field image shows grains and voids; (c) DIC image shows oxide layer. 37

3.16 Two-probe and four-probe measurements of Type II busbars, showing the experimental arrangement used to quantify contact resistance under standardized torque conditions: (a) experimental test setup; (b) two- and four-probe results. . 37

3.17 Activation and release distances of reed sensors tested under five magnet orientations, including statistical separations obtained through one-way ANOVA to identify orientation-dependent behavior. Letters indicate statistical groupings for (a) “On” (one-way ANOVA, $p > 0.05$) and (b) “Off” distances (one-way ANOVA, $p < 0.05$). Data are mean ± SD (n = 10). 39

3.18 Switching-distance results for reed sensors incorporating straight or bent terminals and two spring orientations, demonstrating the effect of mechanical preloading on sensitivity: (a) straight and (b) bent terminals under aligned and rotated spring orientations. 41

3.19 Fully assembled spring-integrated reed-sensor prototype designed for EV applications, showing the compact PBT housing and protected internal components. 42

3.20 Laser-power optimization for lignin-based LIG, showing differences in pattern uniformity and substrate stability across single- and multi-pass irradiation sequences from 20% to 1% power at 450 DPI, 5 kHz, and 200 mm/s. 44

3.21 Sheet-resistance comparison of LIG films produced using three laser-power protocols across nine lignin-based formulations, illustrating the combined influence of coating chemistry and energy input: (a) LIG 1 (3% + 1%), (b) LIG 2 (1% + 3% + 1%), and (c) LIG 3 (1% + 1% + 1%). 45

3.22 Surface morphology of a 10 mm × 10 mm LIG pattern produced under optimized low-power conditions, showing continuous and well-defined graphitized regions. 46

3.23 Visual comparison of LIG traces before and after water-washing for two formulations, showing improved surface clarity and structural retention following removal of unconverted coating. (a) before water washing of H (b) after water washing of H, and (c) formulation I. 46

List of Tables

2.1 Details of lignin-based coating formulations 19

3.1 Flexural properties of hybrid nanocomposites. 24

3.2 Glass transition temperatures (T_g) of CFRP nanocomposites. 25

3.3 Impedance spectroscopy results for CFRPs: resistance, inductance, percent error, and equivalent circuit model. 27

3.4 Comparison of simulated and measured magnetic flux density values at 1.6 mm from the center of small copper busbars (Type III) under 40 A current. 33

List of Abbreviations

Abbreviation	Meaning
EV	Electric Vehicle
CFRP	Carbon Fiber Reinforced Polymer
MWCNT	Multi-Walled Carbon Nanotube
P-MWCNT	Pristine Multi-Walled Carbon Nanotube
Ni-MWCNT	Nickel-Coated Multi-Walled Carbon Nanotube
IL	Ionic Liquid
[BMIM][Tf_2N]	1-Butyl-3-Methylimidazolium bis(Trifluoromethylsulfonyl)imide
CFRPIP	CFRP with IL-treated Pristine MWCNTs
CFRPINi	CFRP with IL-treated Nickel-Coated MWCNTs
LIG	Laser-Induced Graphene
DT	Digital Twin
COMSOL®	COMSOL Multiphysics Simulation Software
DMA	Dynamic Mechanical Analysis
FTIR	Fourier Transform Infrared Spectroscopy
SEM	Scanning Electron Microscopy
UTM	Universal Testing Machine
Tg	Glass Transition Temperature
TC	Thermal Conductivity
ASTM	American Society for Testing and Materials
IEC	International Electrotechnical Commission
ISO	International Organization for Standardization
CISPR	Comité International Spécial des Perturbations Radioélectriques
EMI	Electromagnetic Interference
BMS	Battery Management System
SOC	State of Charge
EOL	End of Life
BOL	Beginning of Life

PAN	Polyacrylonitrile
SS	Stainless Steel
$\mu\Omega$	Micro-Ohm
GPa	Gigapascal
MPa	Megapascal
°C	Degree Celsius
W/m·K	Watt per Meter–Kelvin
A	Ampere
kN	Kilonewton
Nm/rad	Newton Meter per Radian
V	Volt
mT	Millitesla

Chapter 1

Introduction and Theoretical Scope

Global efforts to decarbonize transport have intensified interest in electric vehicles (EVs), placing renewed emphasis on battery systems that are lighter, safer, and more sustainable. The present thesis investigates four component-level domains that are related to EV battery performance: (i) multifunctional structural enclosures based on carbon-fiber nanocomposites, (ii) copper busbar design for efficient current distribution, (iii) mechanically stabilized reed switches for reliable sensing under vibration, and (iv) low-impact electronics fabricated as laser-induced graphene (LIG) on lignin-based substrates. The motivation for this is to demonstrate how material selection choices converge and design practices can lead to gain a system level solution for durability, electrical efficiency and environmental compatibility.

1.1 Global Energy Transition and Electric Mobility

The shift towards electrification of transport policy and industrial roadmaps can be attributed to the energy transition. Battery packs are now electromechanical assemblies as an integral part of the functional system where the battery enclosure, metallic components for high current transmission, sensors and embedded circuits interact using coupled mechanical, thermal and electromagnetic loads. Design choices that were previously made with a single attribute including, mass reduction, or thermal stability or corrosion resistance are now increasingly looked at in terms of their cross-effects in terms of safety, re-recyclability and manufacturing throughput.

Within this context, carbon fiber reinforced polymers (CFRPs) promise high specific stiffness and strength, however, the use in enclosure applications may be dependent on impact resistance, heat management adjacent to cells and/or compatibility of such materials with sensing or shielding functions. Power routing through copper busbars should have low resistive losses and local heating during fast charge events while having low electromagnetic compatibility. Sensing subsystems tend to cause reliability problems in vibrations and thermal cycling as well. Similarly, the environmental footprint of printed wiring and complex circuit fabrication through

materials with low solvent content to ease recycling is also very important in future applications. The present work addresses these requirements by a combination of experimental methods and a modeling approach and by a focus on scalable fabrication methods.

1.2 Problem Statement

Despite rapid advances in the automobile sector, several gaps still persist at the component and system level:

1. **Structural enclosures :** Conventional metallic housings provide high strength and thermal conductivity but at the cost of high mass and complicate electrical isolation. To resolve the weight issue, unmodified CFRP composites are also utilized but may lack multi-functionality, such as, limited damping, and/ or challenging thermal pathways.

2. **Power distribution :** Copper busbars are key components in power distribution. But, their geometry and joining methods such as welding are often optimized empirically. Study on predictive framework, localized heating at welds, stress accumulation near fasteners, and non-uniform magnetic fields due to current still needs to be addressed.

3. **Sensing reliability :**Reed switches/ sensors are helpful for low-power position and/ or interlock functions in automobile. However, their switching repeatability could be degraded due to misalignment, shock, and high-frequency vibration. Minor geometric changes in the housing or actuation magnet can also change the hysteresis and switching time of reed sensors.

4. **Sustainable electronics :** Most flexible circuits rely on petrochemical substrates and solvent-intensive processes. For sustainability and CO_2 footprint, bio-based substrates are the most feasible option due to their environmental friendly properties. Nevertheless, for consistent conductivity, and mechanical integrity after laser conversion, careful tuning of both chemistry and process parameters are important aspects which require further investigations.

1.3 Research Objectives

The thesis pursues four interlinked objectives:

- **O1–Multifunctional CFRP nanocomposites:** Fabricate and characterize CFRP laminates incorporating ionic-liquid-modified multi-walled carbon nanotubes (MWCNTs) for balance among flexural strength, storage modulus, electrical resistance, and thermal characteristics. Targeted outcome: a composition that achieves high flexural strength

($\approx$ 803 MPa) and modulus ($\approx$ 88 GPa) while reducing electrical resistance to the percolation regime.

- **O2–Digital-twin-guided busbar design:** Develop a coupled electromagnetic–thermal–mechanical model for copper busbars to assess the performance between 100 A and 500 A. Conduct experimental test to evaluate structural and functional performance. Targeted outcome: voltage drop ($\approx$ 0.009 V to 0.047 V), magnetic field distributions, hot-spot formation at welds, and thermally induced deformation.
- **O3–Mechanically stabilized reed sensors:** Redesign reed switch housings using sustainable materials and advanced fabrication techniques. Evaluation of switching dynamics under different orientations of magnet. Incorporate spring to reduce switching distance and improve damping capability under extreme conditions. Targeted outcome: activation of reed sensor near 2.3 mm with reduced variance.
- **O4–LIG on lignin substrates:** Establish a low-power CO_2-laser process for converting lignin-based coatings to conductive graphene-like networks. Targeted outcome: fabricate interdigitated capacitors, and achieve sheet resistances below 100 Ω sq^{-1} with minimal substrate damage.

1.4 Literature Review

1.4.1 Materials for Lightweight, Functional Enclosures

Electric-vehicle (EV) battery systems require materials that combine low density with multifunctional performance for efficient heat dissipation, electromagnetic shielding, and structural integrity. CFRP composites have emerged as leading candidates within both automotive and aerospace sectors because of their high strength-to-weight ratio, corrosion resistance, and tunable mechanical characteristics [1–3]. Incorporating nanomaterials e.g multi-walled carbon nanotubes (MWCNTs) into CFRP composites further enhances structural and functional performance of composites making them suitable for multifunctional battery enclosures in advanced automobiles [4–6].

Ren et al. [4] reported tensile strengths close to 1200 MPa under corrosive conditions to draw attention on durability of CFRP composites in chemically aggressive environments. Good results (close to 0.8 W m^{-1} K^{-1}) were obtained by Moyer et al. [5], who confirmed the possibilities of such composites for the treatment of passive heat in compact assembly. Performance optimization can be achieved by adjustment of fiber orientation, surface treatment and resin chemistry when reinforced with functional nanofillers [7–9]. Responding to the international demand for sustainable, high-strength materials, in recent studies the focus has been laid on hybrid systems and energy-efficient processing strategies [10–14]. Increasing

industrial implementation of CFRP hybrid composites is also a way forward to minimize energy consumption and life cycle emissions without compromising the mechanical excellence.

Embedding nanoscale reinforcements such as particles, tubes or fibers have significant improving composite stiffness, conductivity and toughness [15–18]. Among them, MWCNTs can be the most effective ones, which have dedicated to their excellent aspect ratio and the inherent electrical and thermal properties. When treated with environmental friendly modifiers, they disperse homogeneously and have an interfacial compatibility, which allows their use in sustainable automotive structures [19–21]. Experimental data clearly illustrate measurable improvements. Wu et al. [19] about 30% of higher tensile strength and enhanced thermal transport with 1 wt% functionalized MWCNTs. Dhanaraju et al. [22] considerable flexural-strength and modulus enhancements. Brown et al. [23] increased dynamic-mechanical-response. Similar results were obtained by Kumar et al. [24] and Chen [25] who achieved high thermal conductivity at low nanotube loadings, while Spinelli et al. [26] and Zhang et al. [27] demonstrated large conductivity gains with small filler content.

Interfacial modification is very important to get better performance. Polymeric, metallic and silane-based coatings have been developed to enhance the nanotube dispersion and adhesion [28–33]. Contemporary research in this field also considers the assessment of the environmental and economical significance from the experience of modified MWCNTs, highlighting the need of scalable, and low impact routes [34]. Functionalization approaches ranging from acid oxidation, plasma treatment to solvent-based functionalization are done to attain higher surface reactivity and compatibility with polymer matrices [35–43]. However, aggressive chemistries can affect the graphitic structure of MWCNTs [30, 30, 44]. Consequently, there has been a virtual shift towards eco-friendly surface treatments which maintain structure and provide better dispersion in a number of matrices [45–47]. The green solvents used include plant extracts, ionic liquids (ILs), and biodegradable polymers are nowadays preferred because of their capacity to be recycled and have a low environmental impact, and thus they are being used more and more in different areas of energy, electronics, and biomedicine [46–50].

Among these approaches, ionic liquids have been of specific interest in view of their use as surface modifiers for carbon-based nanomaterials [51–53]. Their low volatility, chemical tunability and thermal stability ease uniform nanofiller dispersion and strong interfacial coupling in matrix material [53]. Avoiding usage of conventional volatile organic solvents the IL based processing is in agreement with sustainable nano-technology principles [54]. Carbon nanotubes treated with ILs typically have improved mechanical integrity and increased thermal stability [55]; Imidazolium-based ILs in particular have superior characteristics in use, as they improve the colloidal stability of the nanotubes and enhance conductivity and reinforcement [55–57]. Moreover, IL treatment can be be done at room temperature, which is convenient for reducing the energy input and minimizing the degradation of the nanotubes.

Parallel to these composite developments, attention has shifted to bio-derived carbon sources like lignin which is an abundant by-product of pulp and paper production with a high content

of aromatic carbon [58–60]. Once rejected as a waste product, lignin has now been identified as a sustainable source material to make conductive materials. Once coated with flexible substrates and locally converted by laser irradiation, it will create porous laser induced graphene (LIG) foam. This conductive foam provides an avenue towards biodegradable and recyclable electronics [61–63].

LIG allows direct and mask-free production of conductive networks on the lignin-coated papers at a low cost. Recent research showed that LIG that derived from lignin, had a high electrical conductivity, mechanical flexibility and strong adhesion [64–67]. Additives can be added, such as borax or mild solvents, to increase the flame resistance performance of the coatings, graphitic quality, and simple exchange or in situ patterning can be ensured in miniaturized systems [68, 69]. The combination of low sheet resistance and foldability as well as durability makes LIG based on lignin attractive for wearable sensors and flexible circuits [70–72]. Its porous morphology is also a benefit as its high electrochemical activity will prove advantageous in supercapacitors and biosensors [71, 73, 74].

Practical demonstrations are presented for LIG-based chemical and motion sensors, micro supercapacitors, and heaters with high areal capacitance (up to 136 mF cm^{-1}, exceptional cycling endurance (> 10000 cycles), and high mechanical resilience [75–78]. Simple methods of transferring patterns simplify integration into soft or wearable devices [72, 79]. Environmentally, LIG derived from lignin offers a great benefit over petroleum-based materials because it valorizes an industrial waste stream, cuts life cycle emissions [80]. Remaining challenges include aspects of scaling, uniformity of conductivity over large areas, and compatibility with more traditional electronic packaging [78, 81]. In short, lightweight CFRP compounds reinforced with functional nanostructures and bioderived carbon systems such as lignin-based LIG together are a dual approach towards high-performance, and sustainable materials for EV battery enclosures.

1.4.2 Power Distribution and Electromagnetic Compatibility

An electric-vehicle (EV) battery pack is a highly integrated electro-mechanical system which consists of hundreds of individual cells connected in series and parallel arrangements [82]. This architecture offers the voltage and energy capacity that is needed, whereas it also brings large challenges in terms of thermal management and power distribution. Effective current management is therefore a key for maintaining safety, stability of operation and long operational life. Electrical interconnections between cells are usually achieved with the use of busbars, which will allow high currents to be transported with little loss of energy due to resistive losses and/or localized heating [83, 84].

Busbars have two roles both as current distributors between cells and modules on the one hand and as conduction paths of heat between the cells on the other. Their material composing, their cross-sectional geometry and the joining method affect directly both the energy efficiency and the durability of the systems [85–87]. Material selection is based on conductivity, weight

and corrosion resistance requirements [88–92]. Of these, copper is currently the most popular, owing to its high conductivity of electricity and stable oxidation behavior [93–98]. Modern busbar configurations include solid, laminated and flexible busbars which are designed to have a balance between electrical, mechanical and packaging requirements [99, 100].

Traditional prototyping of busbar assemblies has depended upon primary physical investigation that is alternatively costly, time-consuming, and cannot completely outline coupled thermal-electrical interactions [101, 84]. To overcome these limitations, a concept to form a trans-formative tool for designing and performance optimization; namely, the Digital Twin (DT) has come into existence. A DT is an ever-changing digital replica of a physical system combining real-time operational data to stimule behaviour under different conditions [102–104]. This approach opens up the possibility of predictive maintenance and designing and optimising products without repeatedly fabricating them [105–107].

Digital twins enable fast assessment of material and geometry selection, and assist engineers in simulating multi-physical interactions between the components like Joule heating, magnetic field distribution and structural deformation [107, 108, 83]. For example they have been successfully used to analyse the current distribution and the formation of hot spots during fast charging operations [109, 110]. DT-based topology optimization offers functionalities that allow further material savings and maintenance or improvement of electrical and thermal functionality [111–116]. These capabilities make digital twins an invaluable asset for improved safety margins as well as energy efficiency for the modern EV battery systems.

The overall reliability and safety of high capacity EV batteries relies on continuous monitoring and the accurate interpretation of the data and results of the operation. As both primary current carrying elements, a busbar, has a direct impact on the electrical efficiency, thermal equilibrium and mechanical integrity of the battery pack. However, even within the currently available literature, the treatment of these domains remains independent of one another with no consideration of the interdependence of electrical, magnetic, and mechanical phenomena. Solving this gap means need to develop an integrated multiphysics models which can of simultaneously solving electrical, thermal, magnetic, and structural effects. Such unified modeling frameworks would provide a more realistic insight of busbar behavior under dynamic loading, and provide a guiding line for the design of safer, long lasting and more energy-efficient battery systems for the next generation of EVs.

1.4.3 Sensing in Vibration-Prone Environments

Sensors are important components in electric-vehicle (EV) architectures which provide realtime data to monitor the health of the batteries, the operational status and safety-critical conditions [117]. A wide range of sensors is implemented in the area of battery management system (BMS), including temperature sensors for thermal-runaway prevention, current/voltage sensors

for estimating the charge state and strain sensors for detecting mechanical deformation or impact event [118–121].

Among these, reed sensors have seen a broad adoption in automotive systems due to their non-contact actuation, mechanical simplicity and robust performance in harsh service conditions like vibration, dust exposure and temperature conditions [122–125].The compactness and passiveness of the sensor lend it to a special adaption in space limited and safety critical sub-system of EVs.

A typical reed sensor consists of a pair of ferromagnetic contact blades made hermetically sealed in a glass capsule which closes when exposed to an external magnetic field. This configuration provides high switching response speed, high insulation resistance and long service life, which are the advantages for EV safety applications [126–128]. Continued improvement of current precision manufacturing practices has led to miniaturised and more reliable reed switches that are used in fluid level sensing, proximity sensing and current measurement [127]. However, performance degradation can be caused by high-temperature or high-vibration conditions where degradation can be caused by mechanical wear, contact deformation and electromagnetic interference which add electrical noise or contact bounce [126, 129, 130]. Furthermore, the combination of the reed sensors with complicated electronic structures may have packaging and shielding requirements that prevent from high integrated compactness systems [131].

In order to overcome these challenges recent research centers have gone toward materials and fabrication innovations to promote robust sensors. Hybrid composites with transition metal dichalcogenides (TMDs) and graphene-based nanomaterials have been shown to possess enhanced magnetic sensitivity, mechanical stability and environmental stability [132–134]. Similarly, the use of high-performance polymers and fibre reinforced thermosets for encapsulation of the sensors has led to increased resistance against thermal cycling and fatigue and fatigue [135, 136]. Parallel advances in the fabrication of microelectromechanical systems (MEMS) and additive manufacturing have allowed for the miniaturization of sensors and the ability to add geometric customization that is required for the complex geometrical topologies occurring in EV battery packs [128, 136–138].

While these developments have greatly improved the reliability and adaptability of industrial automotive sensing systems, there has always been a gap between the model-based predicted sensing system performance and its validation under actual operating conditions. Bridging this divide will require comprehensive experimental campaigns with replicates of the combined effects of temperature, vibration, and electromagnetic stress of the type common to vehicular environments.

1.4.4 Low-Impact Flexible Electronics

Recent research has focused more on the use of sustainable materials in design of next-generation sensing platforms. Alongside traditional technologies (reed switches), using laser-induced graphene (LIG) material developed directly on lignin-based biopolymer substrates, provides flexible, conductive, and environmentally compatible sensor architectures [139]. The combination of the electrical functionality of graphene and the renewability of lignin allows LIG to make low-cost and solventless electronic patterns without any metallization or chemical treatment.

Experimental demonstrations of LIG-based sensors have shown them to have high gauge sensitivity, strong mechanical flexibility, and good mechanical stability and trustworthy performances at persistently bending or thermal cycling, which makes them suitable candidates to be incorporated into electric vehicle components and battery monitoring modules [140, 141]. Their light weight and conformability also help to embed them in curved or irregular surfaces without causing extra wirings and system mass.

Despite all these advantages, there are still challenges related to the large area manufacturing and guaranteeing uniformity of the patterns over extended surfaces. Good adhesion of the laser-converted conductive traces to different polymer substrates has to be improved. Besides, design of integration with existing automotive electronic architectures, impedance matching and environmental sealing have to be carefully considered.

Even cooperating with these limitations, LIG-enabled sensing platforms are a technically and environmentally feasible direction for the progress of diagnostic and monitoring systems for electric-mobility applications. Their correspondence with the principles of circular manufacturing brings up the potential of bio-derived, laser-processed materials for next generation of low-impact flexible electronics.

1.5 Thesis Structure

The thesis is arranged to follow the chronological development of materials to system aspects:

- **Chapter 1** sets up context, objectives, and reviews the relevant literature in much of the areas of materials, power distribution, sensing and sustainable electronics.
- **Chapter 2** describes experimental approaches and modeling tools for various projects noting the fabrication of composites, set up of digital twins for busbars, reed switch prototyping and testing protocols, and LIG processing on lignin based bio polymer coatings.
- **Chapter 3** presents results and analysis for each domain with a focus on the quantitative performance (e.g., flexural strength approx. 803 MPa with voltage drop 0.009–0.047 V,

100–500 A, reed sensor activation 2.3 mm, sheet resistance less than 100 Ω sq^{-1} and explaining the interpreting mechanism where such data is possible.

- **Chapter 4** is an integration of results at the pack level of the battery pack in discussion of these trade-offs between structural, electrical and environmental criteria and outlining feasible module architectures.
- **Chapter 5** summarizes contributions, acknowledgment to limitations (e.g. long-term durability and full module integrates) and proposes future working such as life-cycle evaluation and obtain pack-scale digital-twin extensions.

Chapter 2

Experimental Methods and Instrumentation

2.1 Fabrication and Characterization of CFRP Nano-composites (*Project 1*)

2.1.1 Materials

The matrix system used in this study was based on a two-component epoxy resin (Araldite® 5052, Huntsman, USA) cured with the corresponding hardener (Aradur® 5052). The reinforcement was a plain-weave carbon-fiber fabric (Toray 3K, 0° / 90° orientation, 200 g m^{-2} areal density). Multi-walled carbon nanotubes (MWCNTs) were introduced as nano-scale reinforcements to enhance both mechanical and electrical properties. Two grades were used: pristine MWCNTs (outer diameter between 20 and 40 nm, length between 5 and 15 μm, > 95 % carbon purity) and nickel-coated MWCNTs (outer diameter between 5 and 15 nm, length > 50 μm, 60 wt % Ni). Pristine MWCNTs were supplied by Chengdu International, China, and nickel-coated MWCNTs were purchased from US Research Nanomaterials Inc., Houston, TX, USA.

To improve dispersion and interfacial characteristics of MWCNTs in the epoxy matrix, the ionic liquid *1–butyl–3–methylimidazolium bis (trifluoromethylsulfonyl) imide* ([BMIM][Tf_2N], > 99 % purity, Sigma-Aldrich, Germany) was used as a surface modifier. Absolute ethanol (analytical grade) served as a solvent medium during functionalization. All materials were handled and stored in a desiccated environment at 25 ± 2 °C to prevent moisture absorption prior to processing.

2.1.2 Ionic Liquid Functionalization of MWCNTs

Functionalization of both pristine and nickel-coated MWCNTs was carried out to improve their wetting and compatibility with the epoxy system while preserving their intrinsic structure. Approximately 3 g of MWCNTs were dispersed in 50 mL of a 5 wt % [BMIM][Tf_2N] solution prepared in ethanol. The suspension was magnetically stirred for 15 min and subsequently sonicated for 30 min at 60 °C in an ultrasonic bath (Elmasonic P60H, Elma GmbH). Following sonication, the mixture was vacuum-filtered and dried in an oven at 60 °C for 1 h under -1 bar to remove residual solvent.

This non-covalent treatment allowed adsorption of the ionic liquid on the nanotube surface through π–π bond and electrostatic interactions, thereby enhancing dispersion without disrupting the graphitic network. The treated powders were stored in sealed amber vials until composite fabrication to avoid contamination or moisture uptake. The whole process is shown in Phase-I of Figure 2.1.

2.1.3 Laminate Fabrication via Vacuum Bagging

The fabrication of nanocomposite laminates was performed using a vacuum-assisted resin infusion process to ensure uniform impregnation of the carbon-fiber reinforcement and to minimize void formation. The whole process is shown in Phase-II of Figure 2.1. The epoxy matrix was prepared by dispersing the functionalized MWCNTs into the Araldite® 5052 resin at filler loadings of 1.0, 1.5, 2.0, and 3.0 wt %. Each dispersion was initially mixed by mechanical stirring at 600 rpm for 20 min and subsequently ultrasonicated for 45 to 60 min at 60 °C using an ultrasonicator.

After homogenization, the stoichiometric amount of Aradur® 5052 hardener was then added (100 : 40 resin-to-hardener ratio by weight), and the mixture was stirred gently to prevent re-entrainment of air bubbles. The mixtures were degassed under a vacuum of -1 bar for 15 min to remove entrapped air.

Four plies of carbon-fiber fabric were cut into 200×200 mm sheets and stacked in a 0° / 90° lay-up sequence on a flat mold coated with release film. The prepared resin was poured onto the stack, and the assembly was enclosed in a vacuum bag with breather and sealant tapes. Infusion was carried out under full vacuum pressure of -1 bar for 30 min to ensure complete impregnation. Curing proceeded at ambient temperature for 24 h, followed by post-curing at 100 °C for 4 h in an oven. The resulting laminates were approximately 1.0 ± 0.1 mm thick and exhibited a glossy, void-free surface finish.

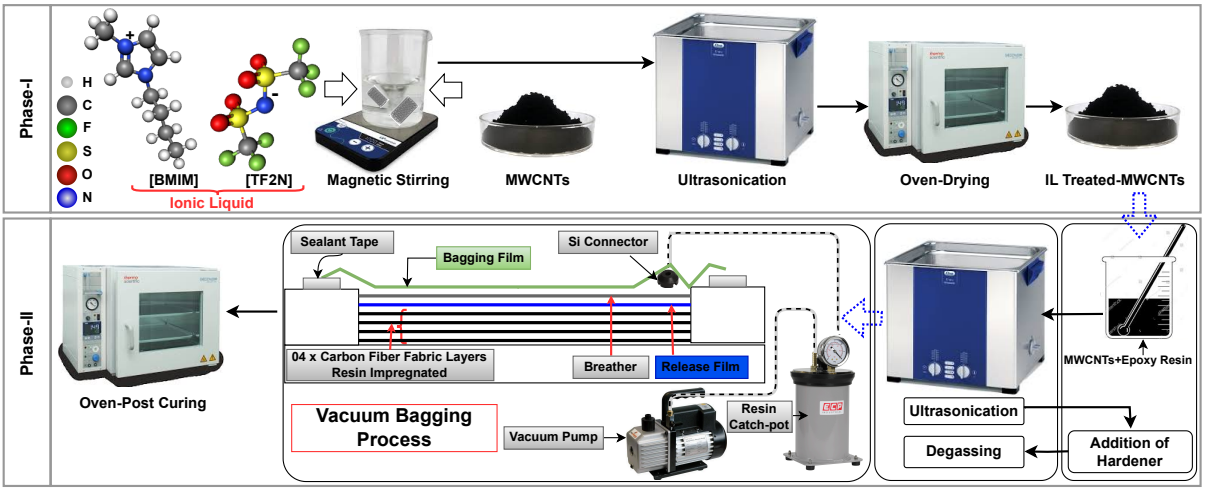

Fig. 2.1 Schematic of the fabrication route for CFRP nanocomposites showing ionic-liquid modification of MWCNTs, dispersion into the epoxy matrix, and subsequent laminate formation through vacuum-assisted resin infusion and curing.

2.1.4 Characterization Techniques

Mechanical Testing

Flexural properties were determined according to ASTM D7264 using a universal testing machine (Galdabini, 30 kN load cell). Test specimens (60 × 13 × 1 mm) were cut using a diamond saw to avoid edge damage. The three-point bending configuration employed a support span of 40 mm and a crosshead speed of 2 mm min^{-1}. Five specimens were tested for each formulation, and mean values with standard deviations were calculated.

Dynamic Mechanical Analysis (DMA)

Viscoelastic behavior was evaluated with a Hitachi DMA7100 operating in dual-cantilever mode. Samples (50 × 10 × 1 mm) were scanned from 25 °C to 2500 °C at a heating rate of 10 °C min^{-1} and an oscillation frequency of 1 Hz. Storage modulus (E'), loss modulus (E''), and damping factor (tan δ) were recorded to assess matrix stiffness and energy dissipation.

Electrical and Thermal Measurements

Electrical resistance was measured using a two-probe impedance setup over the 10 Hz to 1 MHz frequency range. For thermal conductivity, a Thermtest GHFM-01 guarded heat-flow meter was used following ASTM E1530-19. Measurements were performed at mean temperatures of 30 °C, 60 °C, and 90 °C using stainless-steel reference disks for calibration.

Morphological and Structural Characterization Surface and fracture morphologies were examined using a Thermo Fisher Phenom XL G2 scanning electron microscope operating at 10 kV. Samples were sputter-coated with gold for 30 s to prevent charging. Chemical characterization of ionic-liquid adsorption was verified by Fourier-transform infrared spectroscopy (FTIR)

using a PerkinElmer Spectrum Two spectrometer over the 400–4000 cm^{-1} range with 4 cm^{-1} resolution.

2.2 Digital Twin Modeling and Experimental Evaluation of Copper Busbar (*Project 2*)

2.2.1 Materials and Busbars Configurations

Copper busbars of > 99.9 % purity were sourced from MISTA S.p.A., Italy, and machined into three representative configurations for analysis:

- **Type I** – Large-format, laser-welded busbar (216 × 14 × 3 mm) intended for high-current applications.
- **Type II** – Medium rigid busbar (108 × 14 × 3 mm) for contact-resistance evaluation.
- **Type III** – Small geometry variants (83 × 64 × 3 mm) fabricated in three forms: A (central cavity), B (solid block), and C (narrowed solid geometry). The difference in geometries is illustrated in Figure 2.2.

All specimens were cleaned ultrasonically in ethanol for 10 min and air-dried to remove machining residues prior to joining or testing.

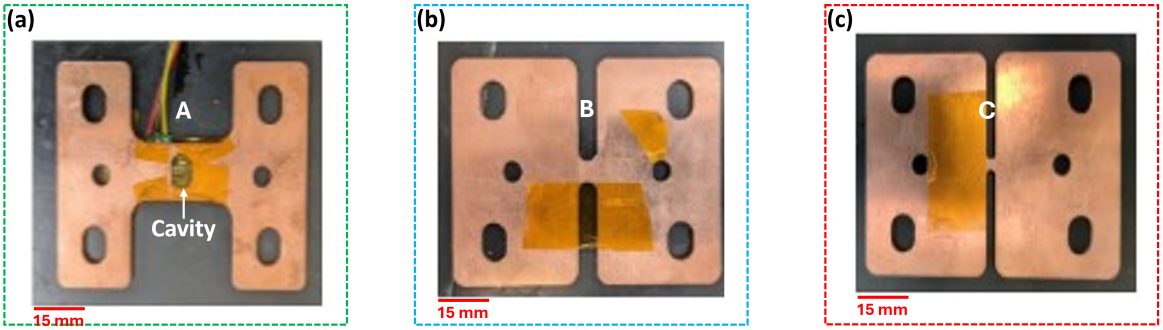

Fig. 2.2 Type III copper busbars used for electromagnetic analysis, illustrating the three structural configurations (A–C) that vary in cavity placement and cross-sectional narrowing to influence magnetic-flux concentration and current distribution.

2.2.2 Laser Welding and Metallurgical Characterization

Laser welding of Type I samples was performed with a fiber-laser system (FL 8000 – ARM 100 / 290, IPG Photonics) operating at 8 kW, 0 mm focal offset, and a scan speed of 50 mm s^{-1}. The process complied with BS EN ISO 13919-1:2019 standards for weld quality.

Cross-sectional samples were prepared by sequential grinding with SiC papers (grit 120 $\rightarrow$ 2000) and etched in 10 % $FeCl_3$ for 15 s. Optical micrographs were captured using an Olympus DSX 1000 digital microscope to assess penetration depth, fusion uniformity, and porosity. Preliminary inspection revealed complete fusion with minor grain coarsening near the heat-affected zone, characteristic of rapid thermal cycling during high-energy welding.

2.2.3 Digital Twin Model Construction

A three-dimensional multiphysics model was developed in COMSOL Multiphysics 6.3, coupling the following physics interfaces:

- *Magnetic Fields (no currents)* and *Electric Currents* for electromagnetic simulation,
- *Heat Transfer in Solids* to capture Joule-heating and conductive losses,
- *Solid Mechanics* to resolve thermally induced stress and deformation.

These modules were linked through electromagnetic-heating and thermal-expansion couplings. Each busbar geometry was discretized with fine tetrahedral elements, refined around weld and bolt zones to improve convergence. Boundary conditions included fixed mechanical supports at bolt locations, an ambient temperature of 25 °C, and applied direct currents from 100 A to 500 A.

Outputs from the model comprised:

- Electric-potential and current-density distributions,
- Resistive heat generation and temperature fields,
- Magnetic-flux density mapping, and
- Thermo-mechanical deformation contours.

Preliminary convergence tests confirmed mesh independence when element counts exceeded 1.2×10^5 *nodes, ensuring numerical stability without excessive computation time.*

2.2.4 Experimental Characterization

Mechanical Evaluation
Mechanical integrity of welded Type I busbars was assessed by:

- **Three-point bending tests** (ASTM E143; support span 100 mm) on Galdabini universal testing machine,

- **Torsion testing** using an Instron 8850 rotational rig, and
- **Edge-bending tests** to evaluate local compliance and weld ductility.

Peak load, yield force, and deflection at failure were recorded to evaluate structural performance of the laser welded busbars.

Electrical Characterization
For Type II busbars, contact resistance was measured according to IEC 60269-1 using both two- and four-probe configurations on a Hioki RM3545A micro-ohmmeter. Tests were conducted at torques of 3.2 Nm and currents of 1 A and 10 A to replicate operational conditions. Average resistance values ranged between 12 and 19 $\mu\Omega$.

Magnetic Flux Mapping
Type III geometries were tested under 40 A DC using ACS37612 Hall-effect sensors positioned 1.6 mm above the surface. The experimental set-up is shown in Figure 2.3.

Metallurgical Analysis
Post-test microscopy confirmed weld integrity and revealed limited micro-voiding (< 2 %) within the fusion line. Grain-size variation was consistent with heat-input gradients predicted by the simulation, validating the thermal model.

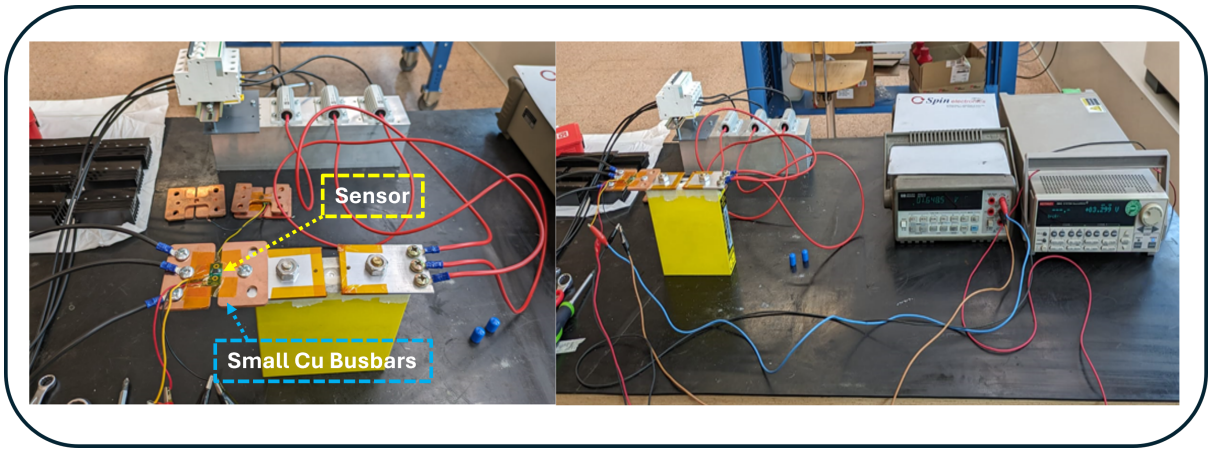

Fig. 2.3 Experimental setup for magnetic-flux density measurements, showing the fixed-position Hall-effect sensor used to capture the field generated by Type III busbars carrying a controlled DC load.

2.2.5 Data Correlation and Model Verification

Simulation results showed voltage drops increasing linearly from 0.009 V (100 A) to 0.047 V (500 A), matching experimental trends within ± 5 %. Peak temperature rise at 500 A was approximately 273 °C, concentrated at weld and bolt regions. Corresponding thermal expansion produced a maximum displacement near 1.1 mm, closely replicating measured deformation.

Magnetic-field magnitudes ranged between 8 and 40 mT, remaining below electromagnetic-compatibility limits specified in CISPR 25. The lowest field intensity (≈ 0.43 mT) occurred in cavity design A, whereas the narrowed geometry C produced the highest (≈ 0.69 mT). These findings validated the sensitivity of flux distribution to geometric constraints and confirmed the predictive accuracy of the digital-twin framework.

2.3 Reed Sensor Fabrication and Testing (*Project 3)*

2.3.1 Design Concept and Materials

The reed-switch system investigated in this study was designed to operate reliably under mechanical vibration and thermal fluctuation typical of electric-vehicle (EV) battery environments. The base element was a KSK-1A66-1530 normally-open reed switch (Standex-Meder Electronics, Germany) rated at 200 V DC, 1.2 A, and a switching power of 10 W. Magnetic actuation was provided by a cylindrical iron-based permanent magnet (⌀ 10 mm $\times$ 4 mm), producing a surface magnetic field between 30 mT and 50 mT as verified using a Lake Shore 475 DSP Gaussmeter.

Sensor housings were fabricated through additive manufacturing to assess the influence of mechanical constraints and alignment on switching behavior. Initial prototypes (Figure 2.4) were printed by fused deposition modeling (FDM) using polylactic acid (PLA), which allowed rapid dimensional verification. Final enclosures (Figure 2.5) were produced via selective laser sintering (SLS) in polybutylene terephthalate (PBT) powder (EOS PA 2200 grade), chosen for its enhanced mechanical strength, dimensional accuracy, and heat resistance up to 120 °C.

To stabilize the reed terminals and mitigate contact fatigue, a miniature stainless-steel compression spring was integrated within the housing cavity. The spring orientation was varied at 0° and 90° relative to the reed terminals, while terminal geometry was tested in both straight and bent configurations. The assembly ensured a controlled mechanical preload on the contact blades, thereby improving response consistency and resilience against vibration-induced misalignment.

2.3.2 Fabrication Process

Each reed switch and magnet pair were first characterized magnetically to determine the baseline activation distance under ideal alignment using the FDM manufactured test case as shown in Figure 2.4. The sensors were then mounted within the SLS-fabricated housings (Figure 2.5) according to four design variants:

1. Straight terminals + aligned spring
2. Straight terminals + rotated spring

3. Bent terminals + aligned spring

4. Bent terminals + rotated spring

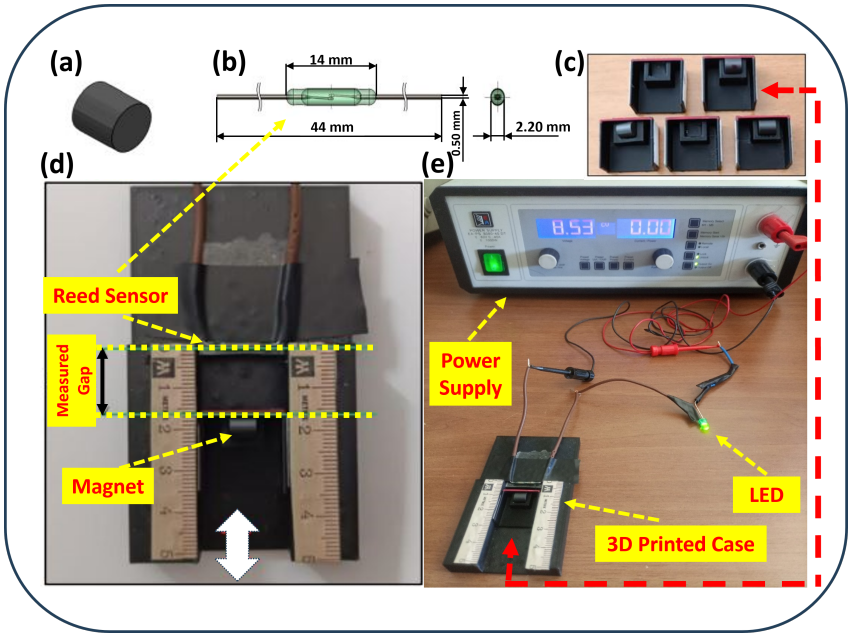

Fig. 2.4 FDM-printed prototype used for reed-sensor characterization, including the (a) magnet, (b) reed sensor, (c) linear sliders for displacement control, (d) & (e) the assembled test fixture designed for repeatable switching-distance measurement.

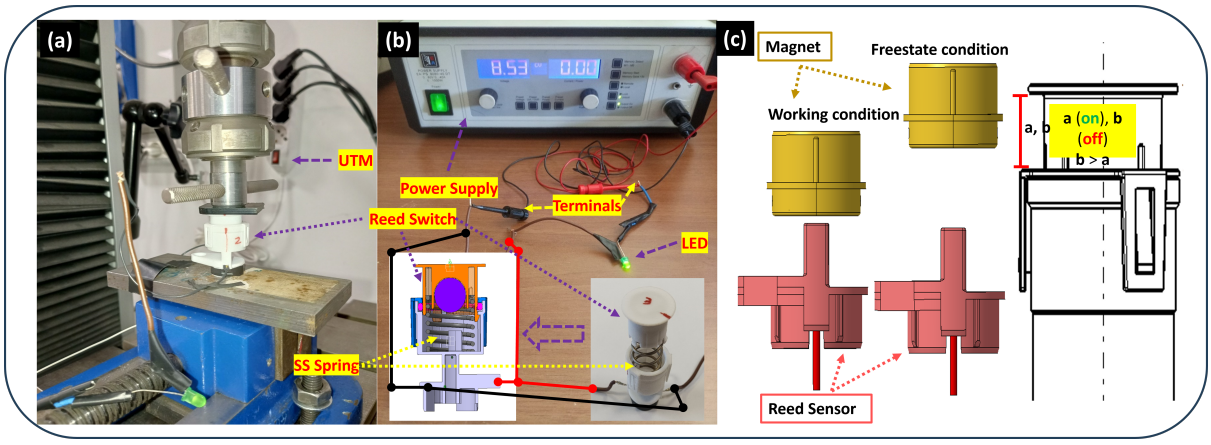

Fig. 2.5 Spring-integrated reed-sensor testing setup: (a) UTM-based control of magnet displacement for precise switching-distance acquisition, (b) electrical verification circuit confirming contact closure and release, and (c) schematic of the reed sensor actuation and relaxation mechanism.

2.3.3 Performance Testing Protocol

Switching distances were measured using a linear scale and LED-based circuit indicator, recording activation (“ON”) and release (“OFF”) points across different orientations of the magnet.

Schematics of different orientations of the magnet used during the experiments is also shown in the Figure 2.6.

Five magnet orientations were examined:

- Center – aligned,
- Center – angled (15°),
- Center – upward (+ 2 mm offset),
- Right-shift – aligned (+ 3 mm lateral offset), and
- Right-shift – upward (+ 3 mm, + 2 mm).

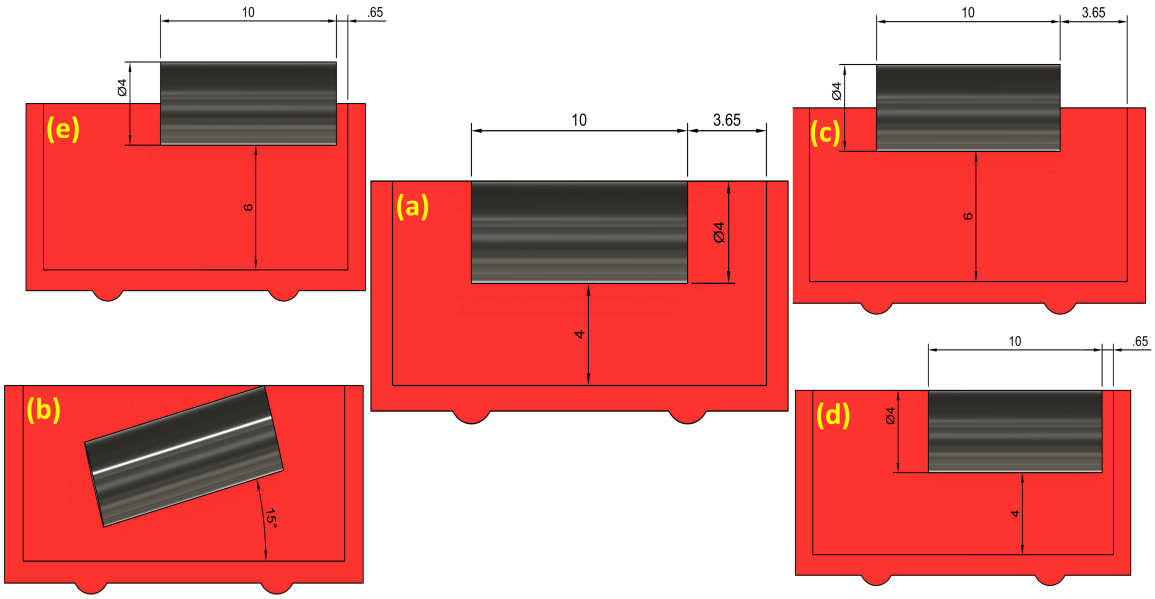

Fig. 2.6 Five magnet-orientation configurations used in reed-switch evaluation, showing variations in (a) center-aligned (b) center-angled (c) center upward (d) right-shift-aligned (e) right-shift-upward, relative to the sensor to quantify alignment-dependent switching behavior.

Each configuration was tested in ten trials. Final prototypes were evaluated with spring orientations of 0° and 90° and terminal geometries (straight and bent). The optimized configuration achieved consistent activation at 2.3 mm and release at 2.7 mm, demonstrating improved sensitivity and repeatability over standard designs.

Table 2.1 Details of lignin-based coating formulations

Formulation	Lignin Type	Additives	Spray duration (s)	Pressure (bar)
A	EKWZ	4HMF	5	1
B	EKWZ	Phenolic (10%) + 4HMF	60	1
C	EKWZ	Urea (10%) + Formaldehyde (90%)	5	1
D	EKWZ	Urea (20%) + Formaldehyde (50%)	30	2
E	EKWZ	Urea (26%) + 4HMF	20	1
F	EKWZ	4HMF + PG (30%) + Formaldehyde	5	1
G	EKWZ	4HMF + PG (20%)	5	1
H	EKWZ	4HMF + PG (70%)	5	1
I	SWWZ	4HMF + PG (10%)	5	1

2.4 Laser-Induced Graphene (LIG) on Bio-polymer Coated Substrates (*Project 4*)

A sustainable method was developed to fabricate conductive graphene patterns (alternative to traditional printed electronics) from lignin-based bio-polymer coatings using low-power CO_2 laser irradiation.

2.4.1 Materials and Coating Formulation

The substrates used for LIG fabrication were 170 GSM CONDAT MATT PERIGORD paper sheets, chosen for their uniform surface finish and dimensional stability under laser irradiation. Lignin-based coating solutions were prepared using softwood kraft lignin (EKWZ and SWWZ grades, Lignoboost AB) as the principal carbon precursor. Nine formulations (A–I) were produced by varying the ratios of 4-hydroxymethylfurfural (HMF), urea, propylene glycol (PG), and formaldehyde. The additives served, respectively, as dehydration catalysts, cross-linking agents, plasticizers, and stabilizers.

Each formulation contained 10 wt % total solids dispersed in distilled water and was homogenized using a IKA RW 20 Digital overhead stirrer at 800 rpm for 20 min. The resulting suspensions were sprayed onto the paper substrate using an airbrush Timbertech operated at 1 to 2 bar pressure as shown in the experimental setup (Figure 2.7). Deposition time was adjusted between 5 s and 60 s to obtain coatings between 25 μm and 40 μm thick. The coated samples were dried at 80 °C for 24 h in an oven before laser processing. The formulations used in the current project are listed in Table 2.1.

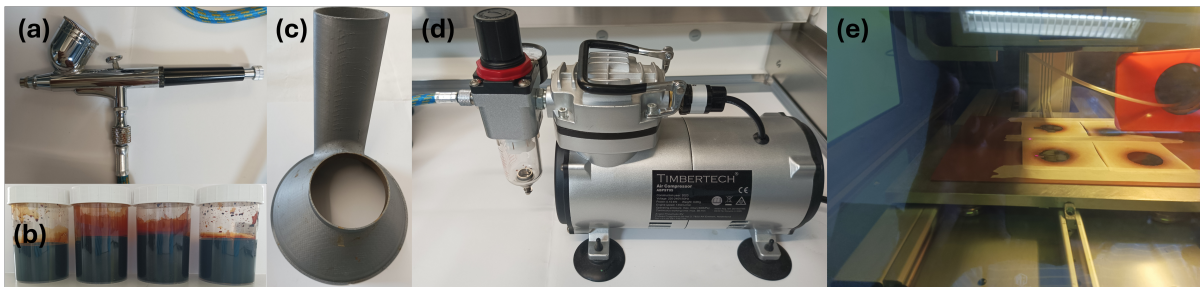

Fig. 2.7 Experimental arrangement for LIG formation on lignin-based coatings, showing the (a) air brush (b) bio polymers (c) masking system (d) air compressor, and (e) CO_2 laser etching process for formation of laser induced graphene on bio polymer coatings.

2.4.2 Laser Processing Parameters

Laser graphitization (Figure 2.7e) was carried out with a CO_2 laser (30 mm, λ = 10.6 μm). The scan resolution was fixed at 450 DPI, frequency 5 kHz, and traverse speed 200 mm^{-1}. Three power sequences were examined:

- LIG–1: 3 % + 1 % (two-pass)
- LIG–2: 1 % + 3 % + 1 % (three-pass)
- LIG–3: 1 % + 1 % + 1 % (three-pass, equal power)

Preliminary trials showed that power levels $\geq$ 10 % ablated the substrate, whereas lower settings yielded incomplete conversion. The LIG–1 condition produced continuous, well-adhered films with minimal discoloration and was therefore adopted for subsequent device fabrication. All patterns were generated in ambient air without inert-gas shielding to maintain process simplicity.

2.4.3 Electrical and Micro-structural Characterization

Sheet resistance was measured using a four-point probe, and micro-structural quality was verified via optical microscopy. Formulations G, H, and I, especially when processed under LIG–1 conditions, exhibited the lowest sheet resistances (below 100 Ω sq^{-1}). Samples were rinsed with de-ionized water for 30 s and dried at 60 °C to remove loosely bound residues before electrical testing.

2.4.4 Device Fabrication and Performance Testing

To demonstrate circuit functionality, interdigitated capacitors (IDCs) were patterned using the LIG–1 sequence on optimized lignin formulations (G, H, I). Electrode spacing was maintained at approximately 0.1 mm to prevent short circuit after expansion or micro fracture during laser

etching. Optical microscopy verified clean electrode edges and absence of thermal ablation beyond the laser path. The complete process flow diagram is shown in Figure 2.8.

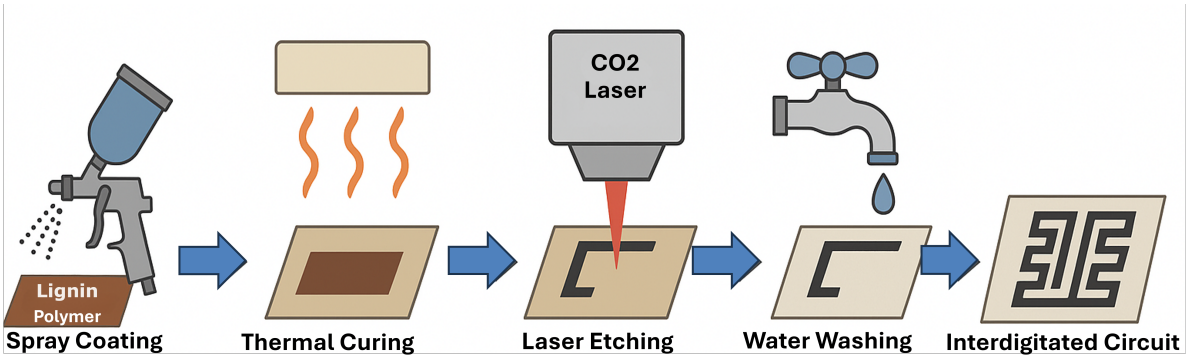

Fig. 2.8 Process flow illustrating spray-coating of lignin formulations onto paper substrates, laser-induced graphitization, and post-treatment steps required to develop conductive LIG patterns.

2.4.5 Environmental and Process Considerations

All laser writing and post-processing steps were solvent-free and produced no hazardous materials. The use of renewable lignin feedstock aligns with circular-economy objectives for disposable or biodegradable electronics. The low-power laser operation (< 1 W) translates into minimal energy consumption of processed area, which illustrates the scalability of the method for low-cost manufacturing.

The combination of lignin-derived coatings and controlled laser graphitization provides an accessible route to environmental friendly flexible electronic components suitable for sensing and energy-storage applications in electric-vehicle systems.

The methodologies developed across these four projects represent a comprehensive experimental platform for advancing sustainable EV battery systems. The combination of ionic liquid-treated nanocomposites, digital twin-based copper conductors, additively manufactured sensors, and bio-derived graphene circuits provides a scalable and environmental friendly route towards high-performance vehicle components.

Chapter 3

Results and Discussion

Chapter 3 will present the experimental results and analysis of all four projects. The first section will explain hybrid nanocomposites of CFRPs. The second section comprises analysis of copper busbars. The third section includes reed sensors, and the forth section will highlight laser-induced graphene on lignin-based polymers.

3.1 Mechanical and Functional Evaluation of CFRP Nanocomposites)

The first experimental study examined the effects of incorporating ionic-liquid-treated multi-walled carbon nanotubes (MWCNTs) on the structural, thermal, and electrical performance of carbon-fiber-reinforced polymer (CFRP) laminates. Particular attention was given to dispersion quality, fiber–matrix interaction, and multifunctional behavior under coupled mechanical and thermal loading. The results are discussed in relation to representative stress–strain curves, storage-modulus trends, and microscopy findings (see Figures 3.1–3.8 and Tables 3.1–3.3).

3.1.1 Flexural Performance

Representative three-point-bending curves for neat and nanofilled laminates are presented in Figure 3.1. All compositions exhibited a linear elastic region followed by a gradual non-linearity preceding catastrophic failure. The incorporation of pristine MWCNTs produced a pronounced stiffening effect, with the 3.0 wt % formulation reaching a flexural strength of $\approx$ 803 MPa and a modulus near 88 GPa, compared with 319 MPa and 36.6 GPa for the unmodified control. The enhancement, exceeding 150 %, indicates efficient stress transfer through a well-developed interphase network.

Intermediate concentrations (between 1.0 and 2.0 wt %) showed progressive increases in both strength and modulus, suggesting a percolative dispersion threshold near 1.5 wt %. At loadings beyond 3 wt %, marginal strength reductions were observed, likely due to partial agglomeration and void formation within the resin. Table 3.1 summarizes the statistical distribution of flexural parameters across all batches, confirming repeatability (standard deviation < 3 %).

During testing, a mild deviation from linearity appeared in the mid-span deflection of the 3 wt % sample, consistent with localized matrix yielding and interfacial shear relaxation. Such behavior implies partial toughening of the matrix owing to ionic-liquid plasticization at the nanotube surface. Failure surfaces (see Figure 3.7) revealed clean fiber pull-out zones and river-mark morphologies typical of energy-absorbing fracture.

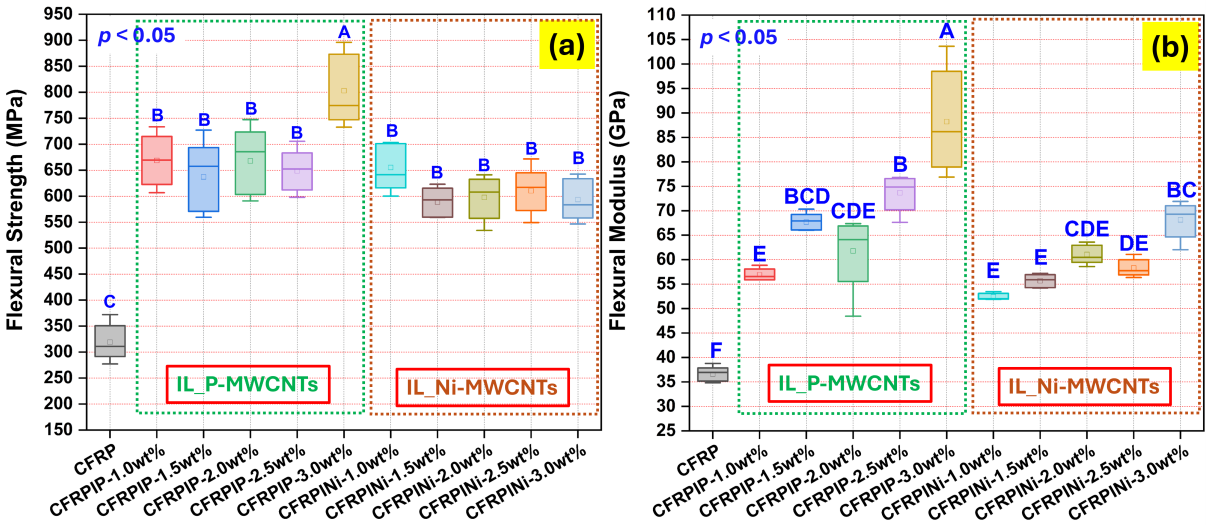

Fig. 3.1 Flexural strength and modulus values for all CFRP nanocomposites, highlighting the influence of ionic liquid treated pristine and nickel-coated MWCNTs content on stiffness and load-bearing capacity: (a) flexural strength; (b) flexural modulus.

3.1.2 Dynamic Mechanical Analysis (DMA)

The temperature-dependent viscoelastic response of the laminates was obtained using a Hitachi DMA7100 in dual-cantilever mode. As shown in Figure 3.2, the storage modulus (E') of nanocomposites consistently exceeded that of the reference sample throughout the 25 to 250 °C range. The 3.0 wt % MWCNT laminate recorded $E' \approx 18$ GPa at room temperature and retained over 60 % of this stiffness at 200 °C, demonstrating improved load transfer and restricted molecular mobility within the epoxy phase.

Table 3.1 Flexural properties of hybrid nanocomposites.

Sample ID	Flexural Strength (MPa)	S.D.	Flexural Modulus (GPa)	S.D.
CFRP	319	35	36.6	1.5
CFRPIP-1.0 wt%	668.7	49.3	56.89	1.2
CFRPIP-1.5 wt%	637.1	67.2	67.71	1.7
CFRPIP-2.0 wt%	667.8	63.7	61.78	7.6
CFRPIP-2.5 wt%	648.5	40.2	73.67	3.7
CFRPIP-3.0 wt%	802.8	67.7	88.21	1.0
CFRPINi-1.0 wt%	655.0	44.6	52.41	6.8
CFRPINi-1.5 wt%	588.5	28.4	55.67	1.3
CFRPINi-2.0 wt%	597.5	41.8	61.05	1.9
CFRPINi-2.5 wt%	610.3	44.2	58.29	1.7
CFRPINi-3.0 wt%	593.2	39.5	68.13	3.7

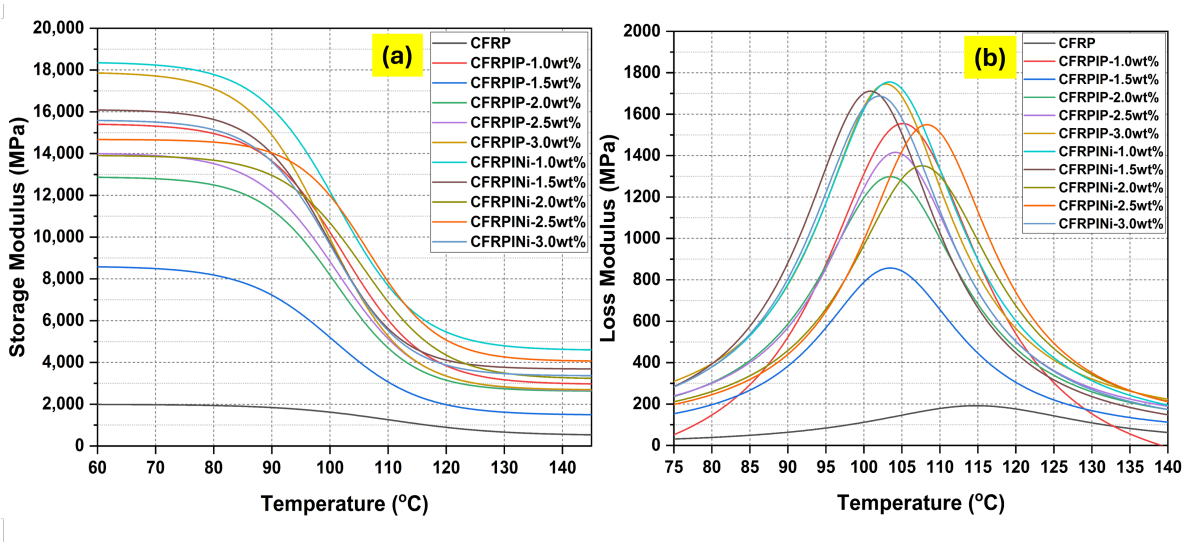

Fig. 3.2 Storage and loss modulus curves obtained from DMA, showing temperature-dependent viscoelastic response and the effect of IL-modified MWCNTs on the stiffness of CFRP laminates: (a) storage modulus (E'); (b) loss modulus (E'').

The corresponding loss modulus (E'') and damping factor (tan δ) curves (Figure 3.3) indicated enhanced energy-dissipation capacity, with modest broadening of the glass-transition region. The overall increase in tan δ amplitude further implies that a fraction of absorbed vibrational energy is dissipated through interfacial sliding which is a desirable attribute for enclosure panels subjected to mechanical vibration in electric-vehicle service.

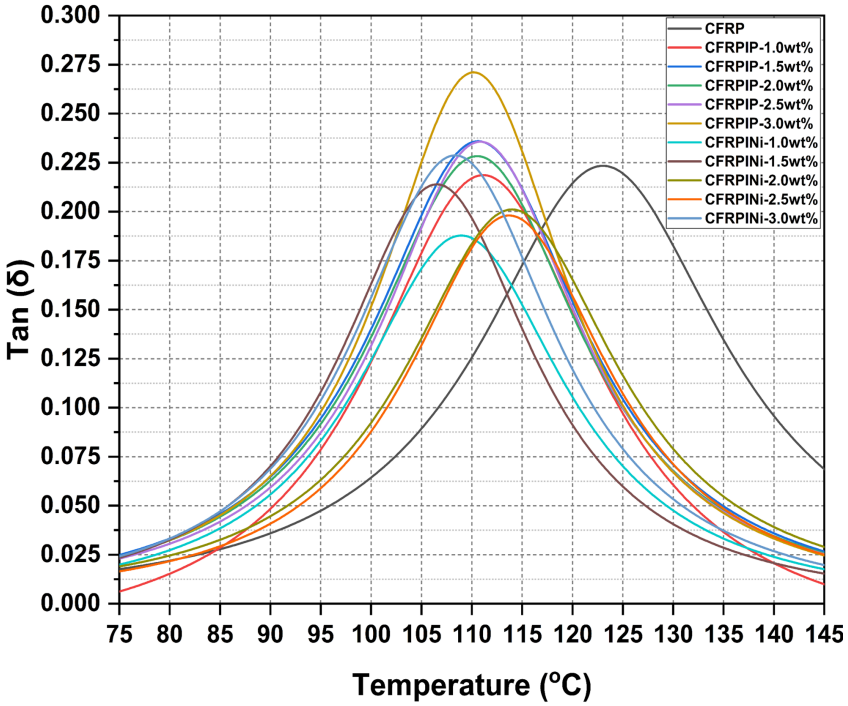

Fig. 3.3 Damping behavior of CFRP nanocomposites showing tan δ profiles and shifts in glass-transition region associated with nanotube dispersion and matrix–filler interactions.

The glass-transition temperature (T_g) showed moderate decrease from 123 °C (neat CFRP) to $\approx$ 110 °C for nanotube-modified systems (Table 3.2). Decrease in the T_g can also be attributed to the increased amount of MWCNTs as well as presence of ionic liquid.

Table 3.2 Glass transition temperatures (T_g) of CFRP nanocomposites.

Sample ID	**T_g (°C)**
CFRP	123
CFRPIP - 1.0 wt %	111
CFRPIP - 1.5 wt %	110
CFRPIP - 2.0 wt %	110
CFRPIP - 2.5 wt %	110
CFRPIP - 3.0 wt %	110
CFRPINi - 1.0 wt%	108
CFRPINi - 1.5 wt %	106
CFRPINi - 2.0 wt %	113
CFRPINi - 2.5 wt %	113
CFRPINi - 3.0 wt %	108

3.1.3 Electrical and Thermal Transport Behavior

Impedance spectroscopy confirmed a sharp drop in electrical resistance upon nanotube incorporation (Table 3.3). The minimum resistance, 29.9 Ω, occurred at 1.5 wt% P-MWCNTs, corresponding to the formation of a conductive network (percolation threshold). Above this concentration, further filler addition produced negligible improvement. This could be attributed to formation of agglomerates of MWCNTs and it is also consistent with percolation theory. Ni-MWCNT composites showed higher resistances (Figure 3.4a) but improved magnetic responsiveness (Figure 3.4b) due to their ferromagnetic properties, which could be beneficial for applications like inductive sensing or EMI-shielded enclosures. The frequency response followed a typical two-region behavior. A plateau at low frequencies corresponds to DC-like conduction. The second shows a dispersive tail at higher frequencies, where interfacial polarization dominates. These features may indicate that ionic-liquid-modified MWCNTs provide efficient charge pathways while maintaining dielectric integrity.

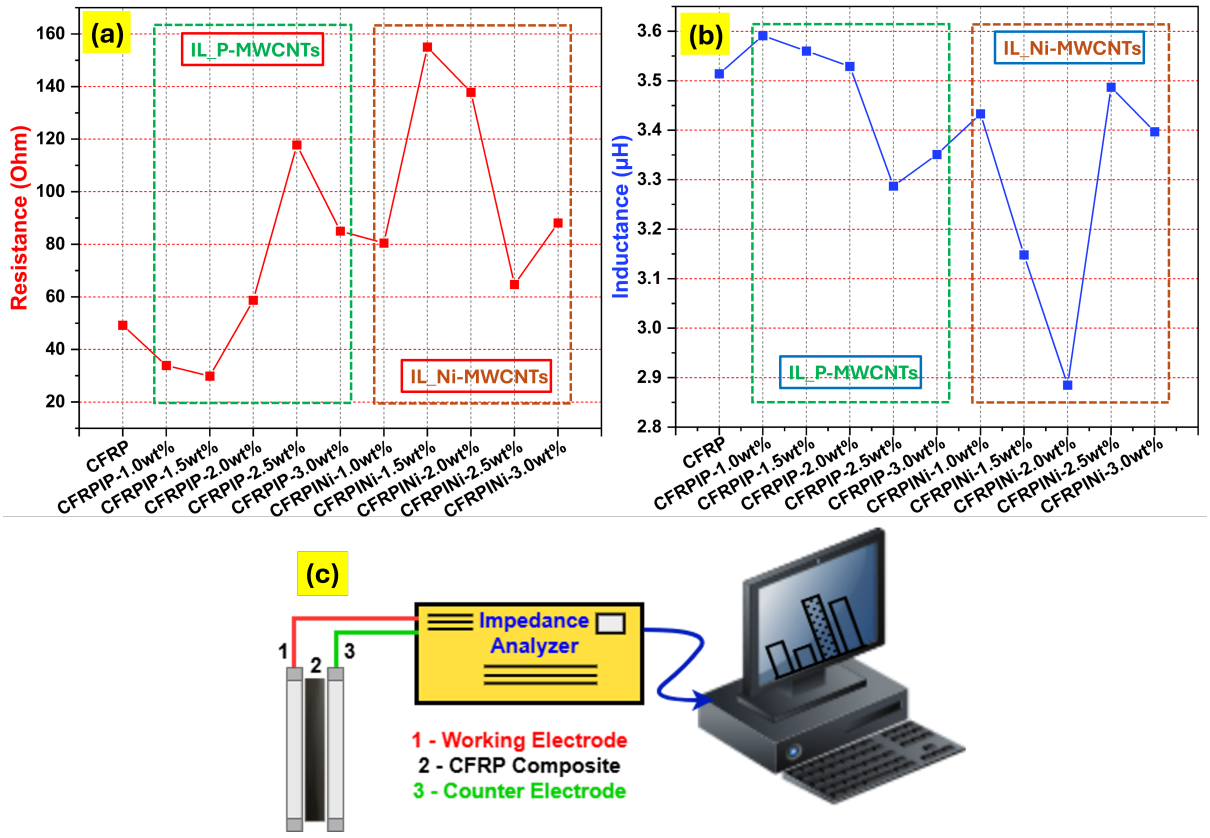

Fig. 3.4 Impedance spectroscopy results depicting (a) resistance, and (b) inductance, of CFRP samples alongside the (c) equivalent R–L circuit model, used to interpret frequency-dependent conduction behavior.

Table 3.3 Impedance spectroscopy results for CFRPs: resistance, inductance, percent error, and equivalent circuit model.

Sample ID	R_1 (Ω)	% Error	L_1 (H)	% Error	Equivalent Circuit
CFRP	49.2	0.069	0.3514×10^{-5}	0.764	R_1L_1
CFRPIP - 1.0 wt %	33.9	0.055	0.3591×10^{-5}	0.426	R_1L_1
CFRPIP - 1.5 wt %	29.89	0.058	0.3560×10^{-5}	0.410	R_1L_1
CFRPIP - 2.0 wt %	58.7	0.067	0.3529×10^{-5}	0.861	R_1L_1
CFRPIP - 2.5 wt %	117.8	0.084	0.3287×10^{-5}	2.237	R_1L_1
CFRPIP - 3.0 wt %	85.0	0.078	0.3351×10^{-5}	1.482	R_1L_1
CFRPINi - 1.0 wt %	80.5	0.075	0.3433×10^{-5}	1.318	R_1L_1
CFRPINi - 1.5 wt %	155.0	0.087	0.3148×10^{-5}	3.149	R_1L_1
CFRPINi - 2.0 wt %	137.8	0.089	0.2885×10^{-5}	3.120	R_1L_1
CFRPINi - 2.5 wt %	64.7	0.071	0.3487×10^{-5}	1.010	R_1L_1
CFRPINi - 3.0 wt %	88.1	0.079	0.3397×10^{-5}	1.543	R_1L_1

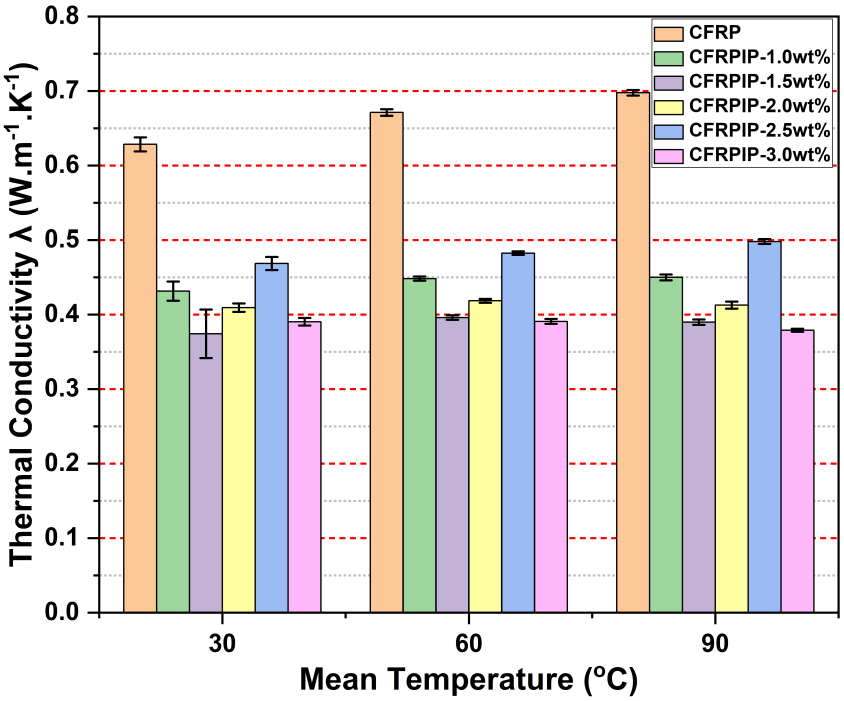

Fig. 3.5 Thermal conductivity of CFRPs containing ionic-liquid-treated pristine MWCNTs measured at multiple temperatures, illustrating the effect of filler content on heat-transfer efficiency.

Thermal conductivity test results of hybrid nanocomposites containing IL treated pristine and IL treated nickel coated MWCNTs are shown in Figures 3.5 & 3.6, respectively. The results measured via a Thermtest GHFM-01 guarded heat-flow meter in accordance with ASTM E1530–19. The reference CFRP sample without nano-fillers showed the optimum thermal

conductivity of 0.698 W m^{-1} K^{-1} at 90 °C. With the addition of MWCNTs, a reduction in thermal conductivity was observed across most samples. For example, CFRPIP-1.0 wt% measured 0.45 W m^{-1} K^{-1}, while CFRPIP-3.0 wt% remained below 0.45 W m^{-1} K^{-1}.

The Ni-coated MWCNT composites provided better thermal conduction as observed in CFRPINi-1.0 wt% achieving 0.5179 W m^{-1} K^{-1}. Although modest, this enhancement is meaningful given the polymeric matrix's inherently low phonon transport capability. Nickel-coated MWCNT systems exhibited slightly higher values, plausibly due to improved phonon coupling at the metal–carbon interface, but mechanical trade-offs limited their overall advantage.

If we observe the two batches of hybrid nanocomposites, a decrease in thermal conductivity upon nanotube addition is observed. The reason can be attributed to several factors. First, the presence of MWCNTs introduces interfacial resistance at the filler-matrix interface, disrupting phonon transport. Second, poor dispersion and the formation of agglomerates hinder the formation of effective thermal pathways. The outcomes may indicate that the bulk thermal conductivity is defined by the individual thermal properties of the whole system. The whole system comprises carbon fibers, epoxy matrix, MWCNTs, ionic liquid, and nickel coating. So, it appears that when low intrinsic thermal conductivity of epoxy matrix is combined with complex orientation of woven carbon fibers, the heat transfer efficiency declines even when high thermal conductive MWCNTs are added.

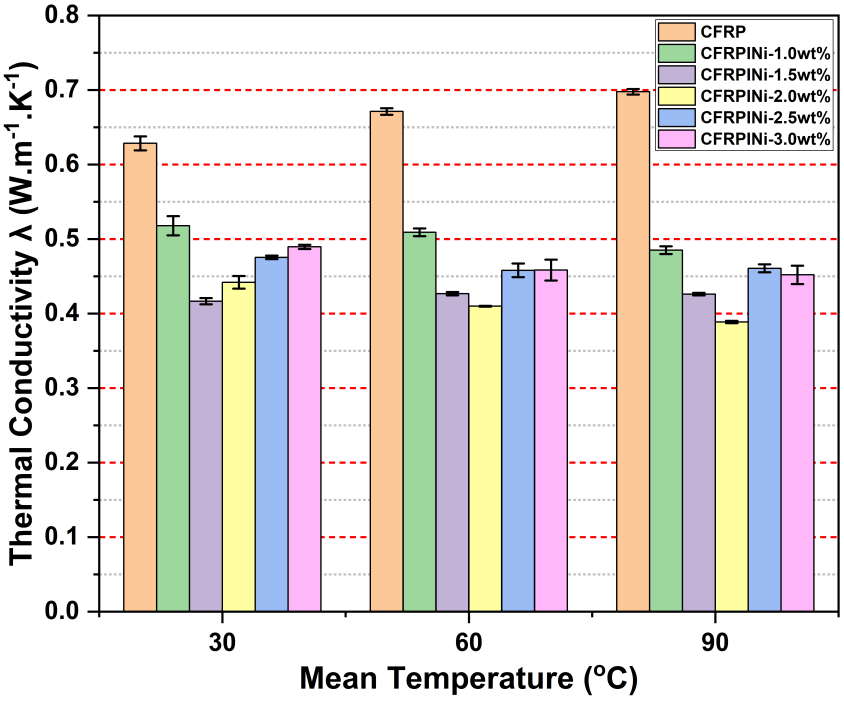

Fig. 3.6 Thermal conductivity of CFRPs reinforced with IL-treated nickel-coated MWCNTs, showing how metal-coated nanotubes influence phonon transport within the composite.

3.1.4 Microscopic and Spectroscopic Analysis

SEM (Figure 3.7) was conducted to carry out the microstructural analysis of the manufactured hybrid nanocomposites. Images of fractured surfaces were taken to observe the fiber impregnation epoxy matrix in samples containing IL-treated MWCNTs as well as samples containing no MWCNTs. In CFRPINi-1.5 wt %, carbon fibers were fully impregnated by the modified resin, indicating good wetting and resin flow during vacuum bagging. Whereas, we also observed voids in the over-loaded composites such as CFRPINi-3.0 wt %, exhibited micro voids due to increased resin viscosity and potential air entrapment during processing. Notably, we observed visible agglomerates of MWCNTs in CFRPIP-2.5 wt % which may appear as stress concentration sites and compromise the homogeneity of the matrix and reduction in the structural performance. These agglomerates of MWCNTs can be seen clearly in (Figure 3.7d). Such entangled network of MWCNTs may lead to better functional performance, but it can cause decline in the structural performance as appeared in Figure 3.1. The void fraction determined by image analysis decreased from ≈ 1.8 % (neat) to < 0.7 % for the 1.5 wt % IL-modified sample, confirming improved wetting and degassing efficiency during resin infusion. Nanotubes also play a role in bridging microcracks and adhering to the fiber surface which could also be an indicative of effective interfacial coupling.

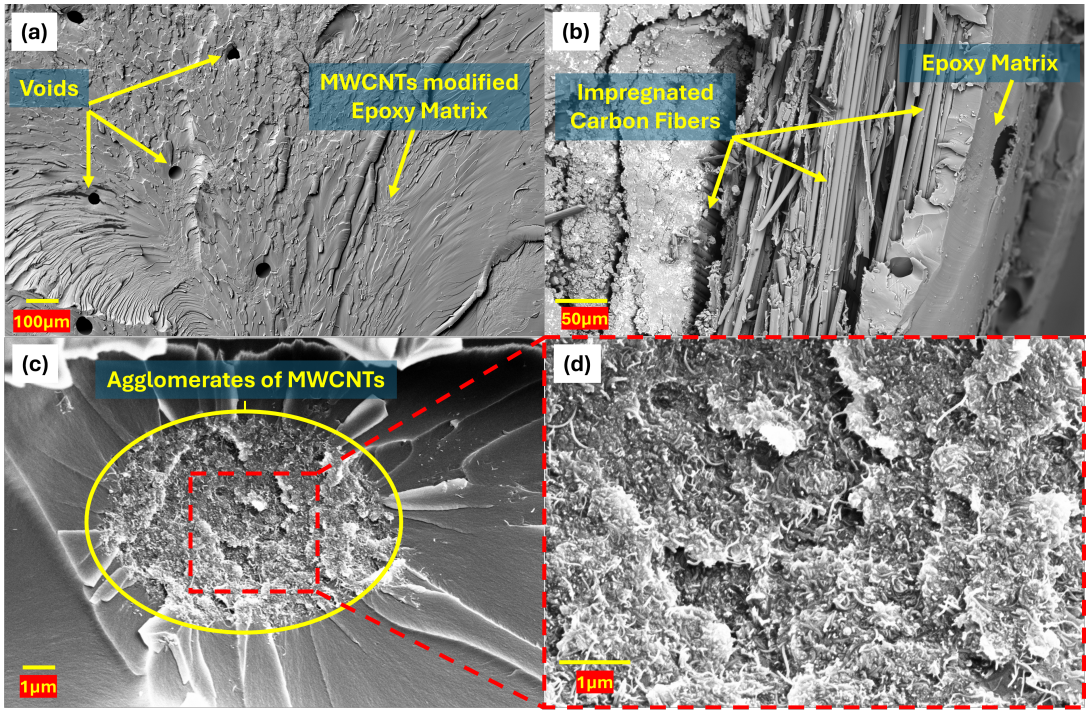

Fig. 3.7 SEM micrographs of fractured CFRP specimens showing voids at high filler loadings, improved resin wetting at optimal concentrations, and visible agglomerates of MWCNTs contributing to stiffness and conductivity variations: (a) voids in CFRPINi-3.0 wt%; (b) uniform epoxy impregnation in CFRPINi-1.5 wt%; (c) MWCNT agglomerates in CFRPIP-2.5 wt%; (d) magnified view of entangled MWCNTs within agglomerates.

We conducted spectroscopic analysis to ensure the presence of ionic liquid on the surface of MWCNTs using Fourier-transform infrared spectroscopy (FTIR). The results are presented in Figure 3.8. The FTIR spectra of IL-treated MWCNTs revealed several characteristic peaks: a broad –OH stretching vibration around 3426 cm^{-1}, C–H stretching at 2923 and 2851 cm^{-1}, and aromatic C=C stretching at 1634 cm^{-1}. Additional peaks at 1390 and 1457 cm^{-1} were associated with imidazolium ring vibrations from the $[BMIM]^+$ cation. Notably, the expected S–N–S stretching modes of the $[Tf_2N]^-$ anion were not strongly present, suggesting that the interaction between the IL and the MWCNTs is predominantly non-covalent in nature. Such outcome of interaction could be beneficial for improving dispersion and interfacial performance without losing structural integrity. The presence of nitrogen and fluorine elements associated with the imidazolium ionic-liquid ($[BMIM][Tf_2N]$) modifier, supporting successful surface adsorption.The functional groups on the surface facilitate better interfacial bonding with the epoxy resin, improving the load transfer efficiency and enabling uniform distribution within the matrix.

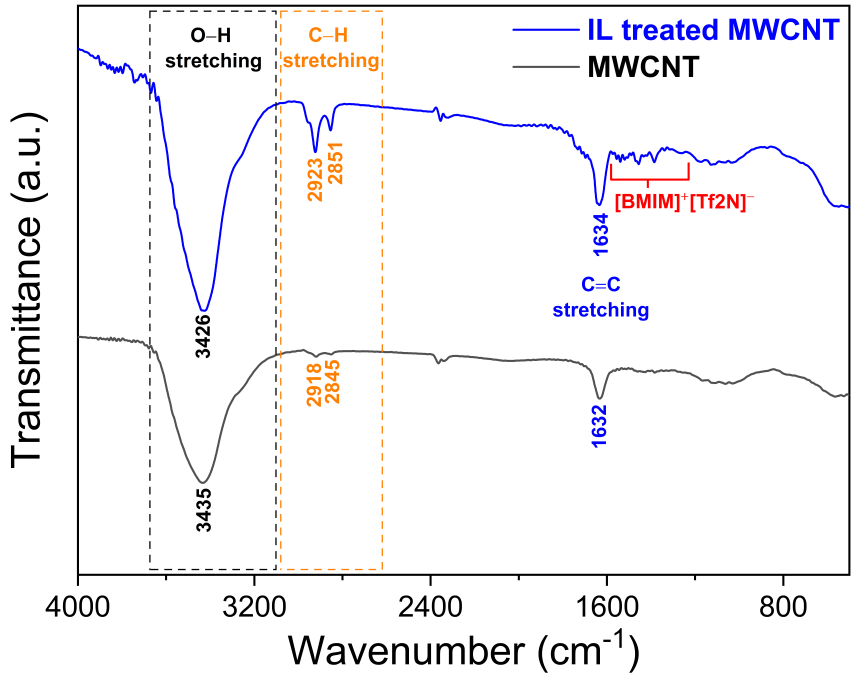

Fig. 3.8 FTIR spectrum of IL-treated MWCNTs showing characteristic absorption bands associated with the imidazolium cation, confirming successful surface functionalization.

3.1.5 Multifunctional Implications and Mechanistic Considerations

The combination of mechanical, electrical, and microstructural findings shows that moderate MWCNT loading along with functionalization of ionic-liquid enhances both stiffness and conductivity without compromising laminate cohesion in manufactured composites. The synergy in the performance may appeared due to two mechanisms: (1) electrostatic and π–π interactions

between ILs and nanotube walls for improving dispersion, and (2) enhanced wetting of carbon fibers with epoxy matrix to reduce micro-void formation.

The damping and conductivity improvements suggest potential applications beyond structural support. The manufactured lightweight enclosures could provide electrostatic-discharge protection and could also be integrated with embedded strain-monitoring networks. Nonetheless, the sensitivity of performance to filler concentration and processing conditions highlights the need for precise control over sonication energy, resin viscosity, and curing profile.

3.1.6 Summary

The CFRP nanocomposites prepared with ionic-liquid-treated MWCNTs exhibit a balanced suite of mechanical and functional improvements:

- Flexural strength: $\approx$ 803 MPa (+150 % vs. neat CFRP)
- Flexural modulus: $\approx$ 88 GPa
- Storage modulus: $\approx$ 18 GPa at 25 °C
- Electrical resistance: $\approx$ 29.9 Ω (at 1.5 wt %)
- Thermal conductivity: $\approx$ 0.52 W m^{-1} K^{-1}

The overall behavior of manufactured hybrid nanocomposites confirms that ionic-liquid-mediated dispersion effectively. It efficiently bridges mechanical and electrical functionality in structural composites. Future optimization should focus on balancing viscosity of the modified matrix and filler dispersion for maximizing repeatability in the large-area prepreg systems for various applications.

3.2 Electrical, Thermal, and Mechanical Analysis of Copper Busbars

In the second study, we investigated the coupled electrical, thermal, and mechanical performance of copper busbars. The busbars are primary conductive pathways between battery cells, modules, and external circuits in EV battery systems. Both computational digital-twin simulations study and experimental evaluation study were carried out under realistic load conditions like fast charging and high acceleration.. The discussion below synthesizes results from voltage-drop characterization, thermal imaging, magnetic-field mapping, and mechanical integrity assessment. We selected three types of copper busbars: Type I (large, laser-welded), Type II (medium, rigid), and Type III (small, geometrically varied), and the results were validated against international safety standards (IEC 60269-1, CISPR 25, ISO 11452).

3.2.1 Electrical Characterization and Voltage Distribution

(Figure 3.9) shows the simulated electric-potential distribution along the Type I busbar under currents between 100 A and 500 A. The potential increased linearly with current, producing voltage drops of 0.009 V (100 A) to 0.047 V (500 A) which is consistent with Ohm's law. The uniform potential gradient across the bar length indicated low resistive loss due to the high conductivity of oxygen-free copper.

Magnetic flux densities ranged from 8 mT to 40 mT but remained below according to CISPR 25 and ISO 11452 thresholds. The symmetry of the flux pattern further indicated that the busbar geometry was effective in avoiding eddy current generation or hotspots associated with magnetic field concentration. This may indicate that it has practical significance for minimizing electromagnetic interference (EMI) with adjacent sensors and control electronics inside battery packs.

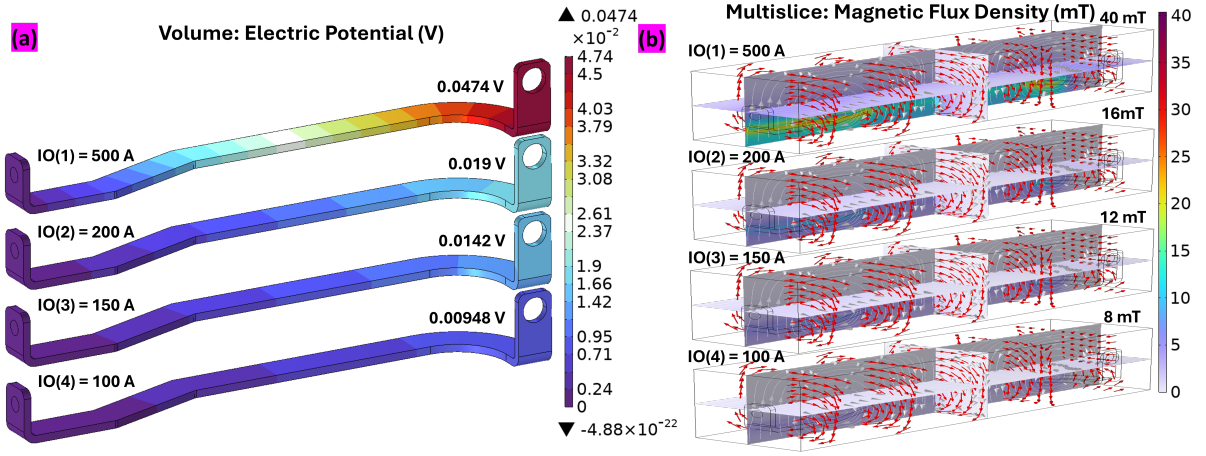

Fig. 3.9 Multiphysics simulation of the Type I laser-welded copper busbar showing (a) electric-potential distribution along the conductor and the resulting (b) magnetic-flux density generated under current loading.

For Type III geometries, we also performed magnetic-flux mapping and simulation at 40 A using an ACS37612 Hall-effect sensor positioned 1.6 mm above the conductor surface. Experimental measurements using ACS37612 Hall sensors (Table 3.4) and simulation data (Figure 3.10) for all three busbars of Type III are also well below the threshold value of magnetic flux density (40 mT) according to CISPR 25 and ISO 11452. Sample A (cavity design) recorded the lowest flux (0.426 mT), Sample B (solid) showed 0.765 mT, and Sample C (narrowed) exhibited 0.69 mT. Solid variants (B and C) of busbars exhibited slightly higher magnetic flux due to current crowding in the middle sections. These outcomes validated the role of geometric features in modulating electromagnetic exposure, supporting the use of physical voids or tapering to minimize localized flux concentration. These results validate the geometric approach of employing strategic cavities or tapers to attenuate local electromagnetic fields in

dense busbar arrays. Moreover, the close agreement with experimental data affirms the accuracy of the Digital Twin framework for predicting field behavior in compact interconnects.

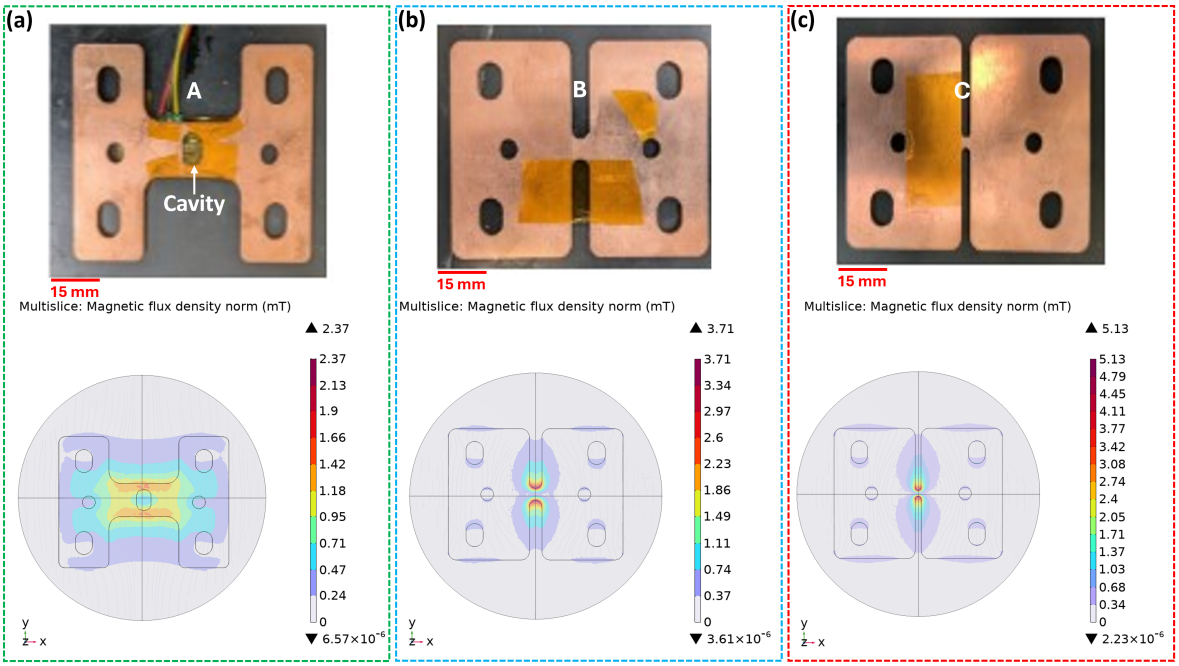

Fig. 3.10 Simulated magnetic-flux density maps for Type III busbars (A–C) at 40 A, illustrating the impact of cavity insertion and cross-section changes on field intensity near the surface: (a) Sample A with central cavity; (b) Sample B with solid geometry; (c) Sample C with narrowed solid geometry.

Table 3.4 Comparison of simulated and measured magnetic flux density values at 1.6 mm from the center of small copper busbars (Type III) under 40 A current.

Sample ID	Variation (mV)	Sensitivity (mV/A)	Magnetic Field (mT) – Sensor	Magnetic Field (mT) – Simulation
A	42.6	1.065	0.426	0.40
B	76.5	1.913	0.765	1.85
C	69.0	1.725	0.690	2.1

3.2.2 Thermal and Thermo-Mechanical Behavior

Thermal simulations (Figure 3.11a) revealed safe operation up to 200 A with temperature increases below 60 °C, while transient peaks at 500 A caused localized heating up to ≈ 273 °C. Such rise in temperature is critical for the weld and bolt contact areas, which are known weak points due to increased resistance and localized Joule heating. Consequently, such scenarios highlight the need for additional cooling mechanisms or improved heat dissipation designs when operating at such high currents for longer durations.

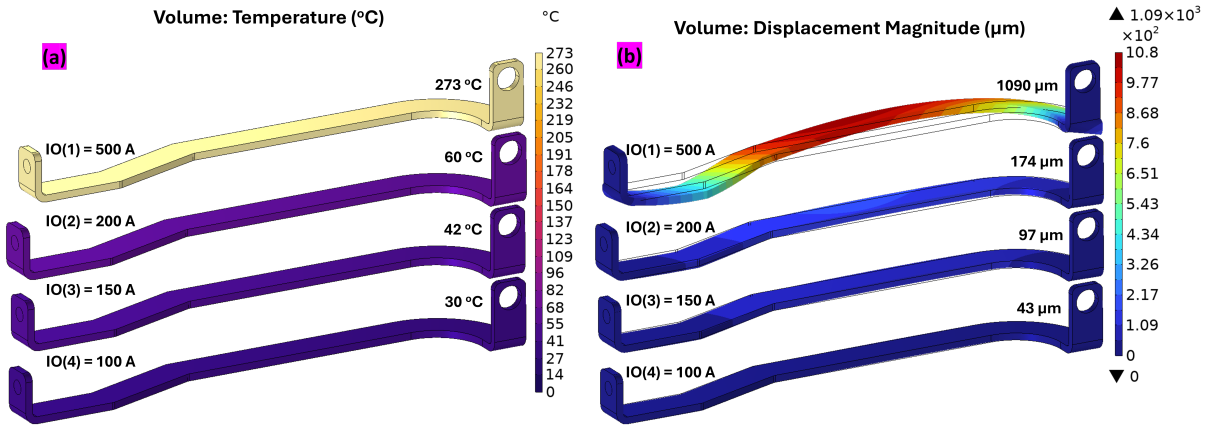

Fig. 3.11 Thermal and thermo-mechanical responses of the Type I busbar under high-current operation showing localized Joule heating and resulting deformation predicted by the digital-twin model: (a) temperature rise due to Joule heating; (b) thermally induced deformation.

Associated thermal expansion led to displacements of 43 μm (100 A) to $\approx$ 1.09 mm (500 A), showing dependency of mechanical strain on the value of current as illustrated in Figure 3.11b. The level of deflection at 500 A, could compromise electrical contacts and compromise mechanical strength by generating microcracks in the soldered or bolted connections over time. These findings validate the importance of reinforcing weld zones, using flexible supports, or modifying geometry to accommodate expansion without stress concentration. The simulation further indicated that such displacement magnitudes, if unmitigated, may slightly misalign mating contacts, warranting design allowances for compliant mounting or periodic torque verification.

3.2.3 Mechanical Testing and Microscopy

The 3-point bending (Figure 3.12), torsion (Figure 3.13), and edge bending tests (Figure 3.14) were performed on the laser-welded Type I busbars. 3-point bend results comparison between the flat copper region and the laser-welded zone revealed a reduction in mechanical strength at the welded region. The maximum force sustained by the unwelded region was 2.43 $\pm$ 0.05 kN, compared to 1.53 $\pm$ 0.11 kN for the welded zone. This indicates g roughly 37 % loss of strength. Similarly, the yield force decreased from 1.60 $\pm$ 0.02 kN to 0.78 $\pm$ 0.05 kN. These outcomes may indicate that these values remain structurally viable under moderate service stresses typical of EV pack installations.

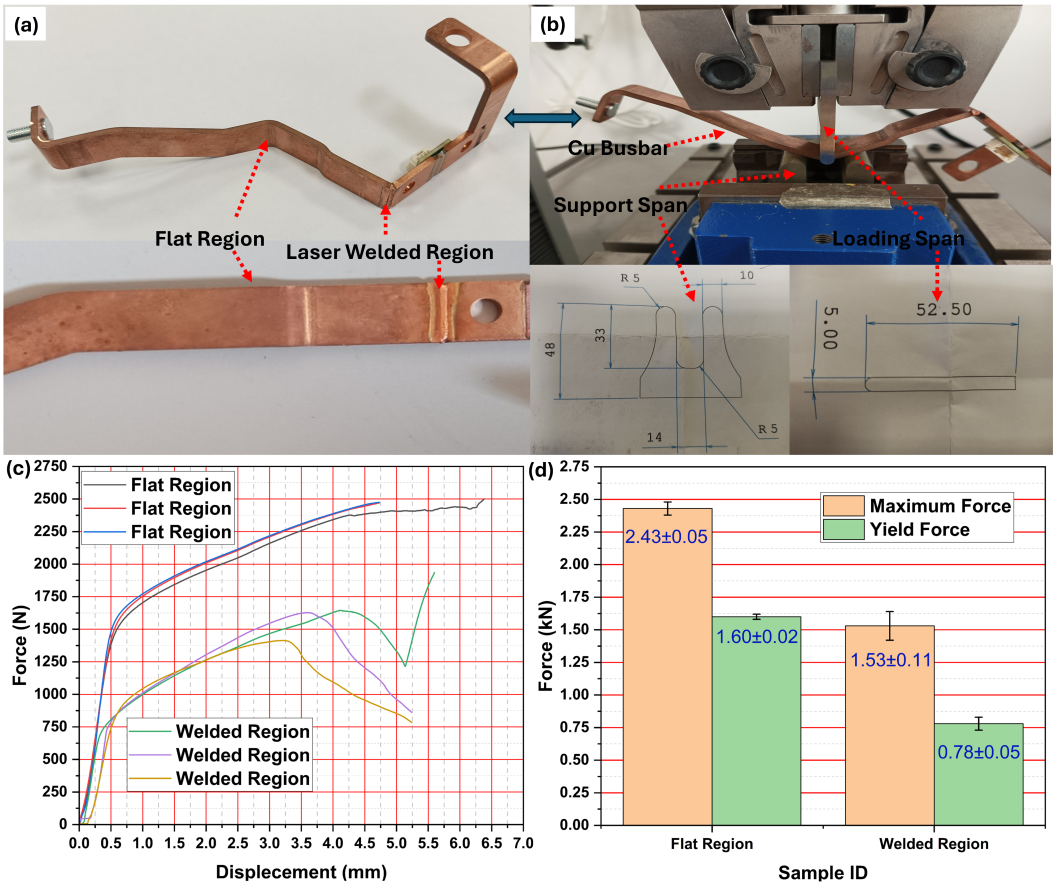

Fig. 3.12 Three-point bending tests of Type I busbars comparing structural performance between unwelded and laser-welded regions, including differences in maximum load and yield behavior: (a, b) test setup; (c, d) comparison of maximum and yield forces for flat and welded regions.

Torsional testing provided further insights into the rotational stiffness of the busbars. Torsional testing using an Instron Torsional Rig revealed an average stiffness of 33.6 Nm rad^{-1}, yielding at $\approx$ 675 Nm and 20° twist. The specimens displayed ductile failure with distinct dimples in fracture surfaces, which may indicate characteristic of localized necking rather than brittle rupture. The moderate reduction in strength relative to bulk copper can be attributed to grain coarsening and void formation induced by rapid heating and cooling during laser welding. Although the values are sufficient for most static loads, these values indicate a reduced resistance to dynamic or cyclic torsional stresses.

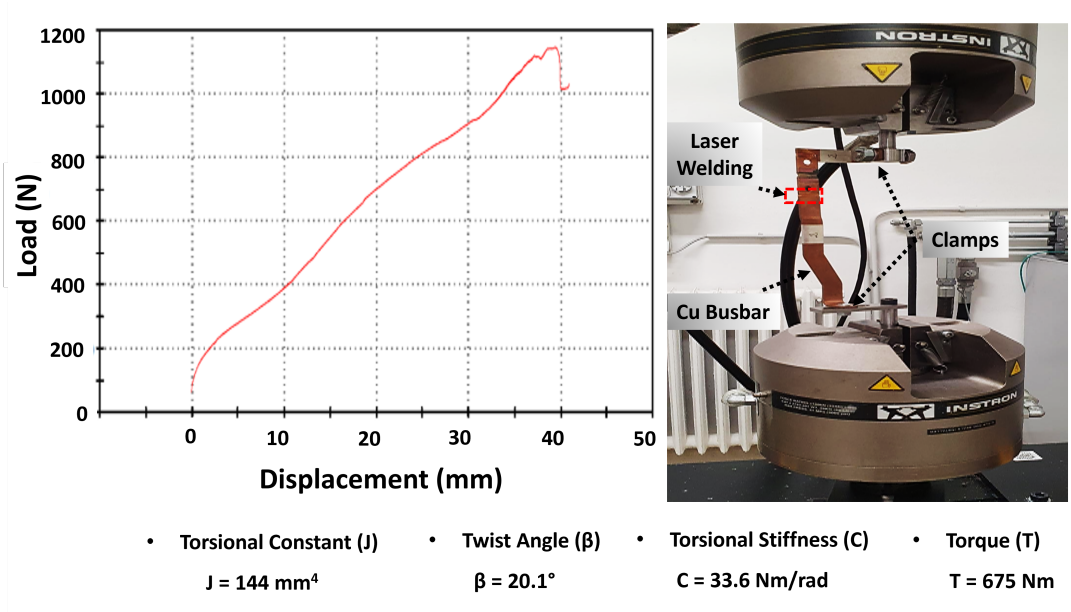

Fig. 3.13 Torsional loading of laser-welded busbars showing the test configuration and recorded torque–rotation response used to assess rotational stiffness and weld integrity.

Bending tests also revealed that the welded region could tolerate up to 362 N before deformation when a bending load is applied. It further highlights the fact that laser welded busbars could be used in EV applications where structural stresses are of moderate level.

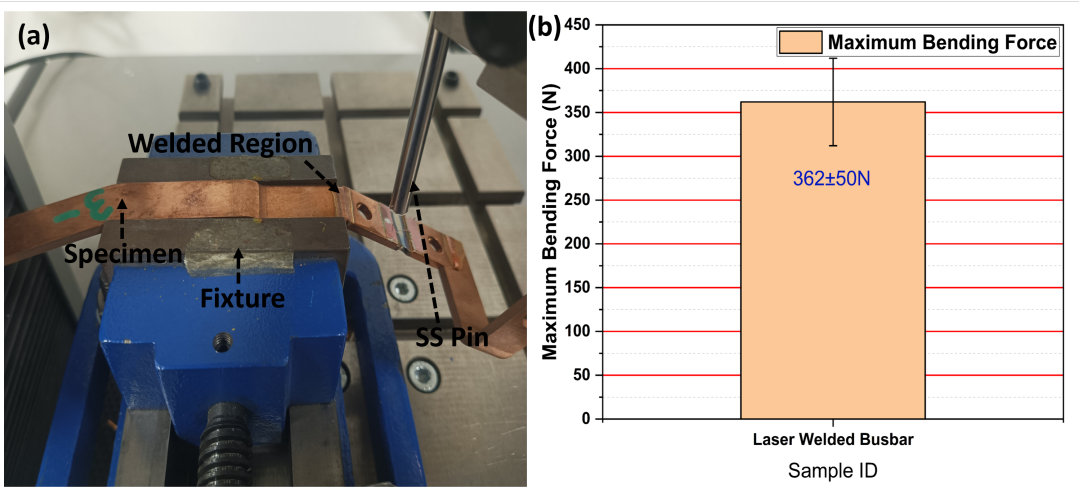

Fig. 3.14 Edge-bending experiment on laser-welded sections of the busbar showing load–displacement response and the influence of the weld zone on local flexibility: (a) test in progress; (b) bar chart comparing bending force required in welded sections.

Optical microscopy of etched cross-sections (Figure 3.15) confirmed coarse, uneven grains in the fusion zone contrasted with the fine-grained base metal. Discrete micro-voids (< 2 %) were observed along the weld boundary, acting as potential nucleation sites for fatigue cracks under cyclic load. However, overall metallurgical quality met BS EN ISO 13919-1 criteria for Class B welds, signifying defect-free fusion.

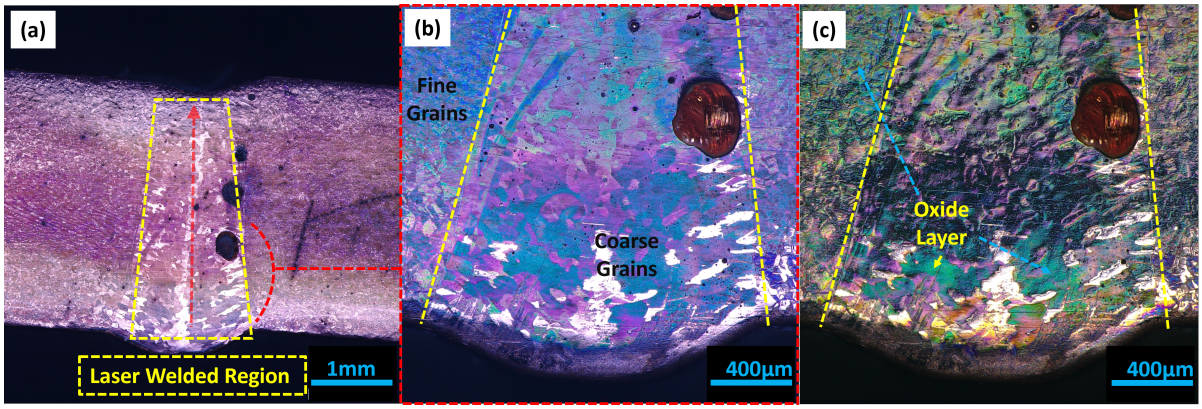

Fig. 3.15 Optical microscopy of etched Type I busbar cross-sections showing grain structures, small voids in the fusion line, and surface oxide features highlighted by differential-interference contrast imaging: (a, b) bright-field image shows grains and voids; (c) DIC image shows oxide layer.

3.2.4 Contact Resistance

The Type II busbars in our study were tested using both two- and four-probe techniques (Figure 3.16, exhibited contact resistances of 12.4 to 18.7 $\mu\Omega$, comfortably below the IEC 60269-1 limit of 20 $\mu\Omega$. We noted slight variations in contact resistance values between specimens which can be attributed to differences in surface oxidation and bolt torque (3.2 Nm). The presence of a thin oxide layer, though increasing surface resistance to some extent, but it could lead to improved corrosion resistance and may not influence the operational performance.

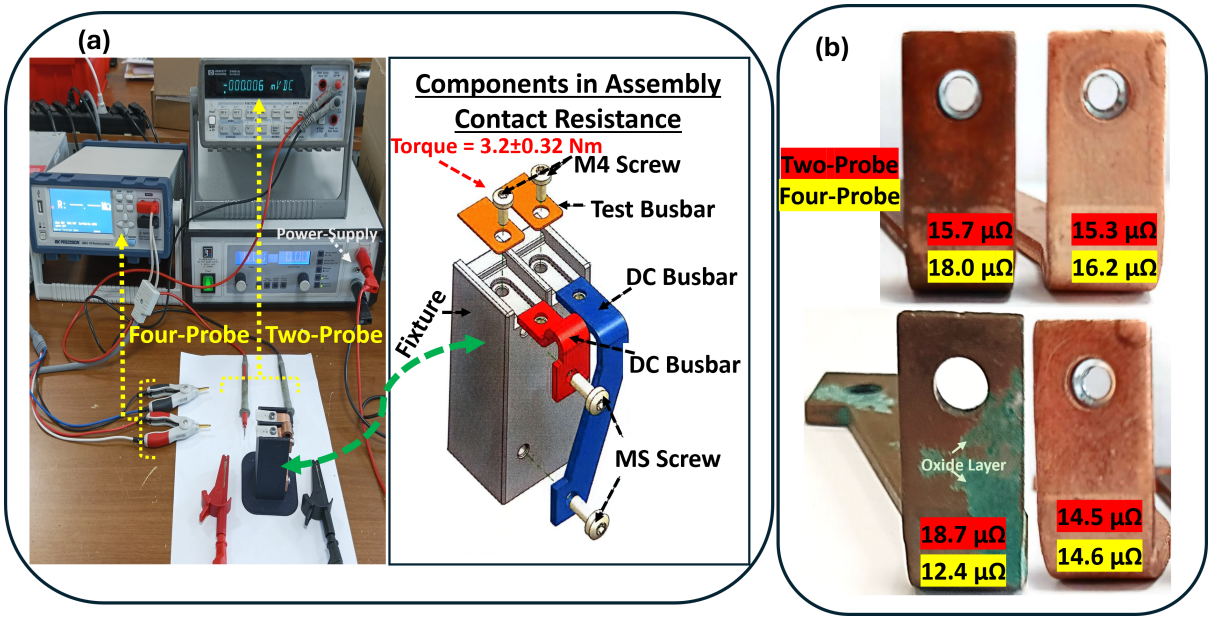

Fig. 3.16 Two-probe and four-probe measurements of Type II busbars, showing the experimental arrangement used to quantify contact resistance under standardized torque conditions: (a) experimental test setup; (b) two- and four-probe results.

3.2.5 Summary

- **Voltage drop:** 0.009 to 0.047 V (100 to 500 A) — linear, low-loss conduction.
- **Contact resistance:** 12.4 to 18.7 $\mu\Omega$ — within IEC 60269-1 limits.
- **Magnetic flux:** 0.43 to 0.77 mT (40 A) — below CISPR 25 limit.
- **Peak temperature:** $\approx$ 273 °C at 500 A; < 60 °C under 200 A.
- **Thermal displacement:** 43 μm $\rightarrow$ 1.09 mm across load range.
- **Torsional stiffness:** 33.6 Nm rad^{-1}; yield $\approx$ 675 Nm.

Keeping in view the outcomes of our test results, it could be suggested that the copper busbars validated through multi-physics modeling and systematic testing exhibit excellent electrical efficiency, thermal tolerance, and structural reliability within the operational envelope of EV battery modules. The integration of digital-twin prediction with empirical data establishes a framework for design optimization and predictive durability assessment. It could help us to reduce the prototyping cost while ensuring compliance with electrical-safety and electromagnetic-compatibility standards.

3.3 Evaluation and Optimization of Reed Sensors

The third experimental phase of our research focused on the fabrication, mechanical optimization, and performance evaluation of reed sensors designed for vibration-prone environments in electric-vehicle (EV) battery systems. The study emphasized how mechanical stabilization through spring integration and geometric reconfiguration affects switching precision, hysteresis, and operational durability. Our study develops an optimized reed sensor for automotive use after investigating effects of magnet orientation using a 3D-printed test fixture of PLA and later another SLS printed housing using PBT was developed to integrate a SS spring to further improve the performance of reed sensor.

In EV battery systems, position and interlock sensors must operate reliably within confined spaces subject to continuous vibration, temperature gradients, and electromagnetic interference. Conventional reed switches—though robust in basic operation—often exhibit contact instability and hysteresis under such conditions. To address these limitations, a mechanically preloaded reed-switch design was developed, combining magnetic actuation with passive damping via an integrated stainless-steel spring. The sensor assembly comprised a KSK-1A66-1530 normally open reed switch (Standex-Meder Electronics, Germany) with a nominal switching voltage of 200 V DC and current rating of 1.2 A. The glass-encapsulated magnetic contacts were actuated by a cylindrical Fe-based magnet (10 mm × 4 mm, surface field $\approx$ 40 mT)

3.3.1 Magnet Orientation and Switching Behavior

In the first phase of our study, we used FDM-printed test assembly to calculate the switching distances of reed sensor at five distinct orientations of magnet as explained in subsection 2.3.3 were tested. Figure 3.17 gives the switching behavior measured for the 5 magnet arrangements. Using each pattern it can be seen that moving the magnet to the right and up gave the shortest travel needed for the sensor to switch. When the magnet was tilted, the sensor turned on at approximately 6.0 - 8.5 mm and released at approximately 7.3–9.2 mm. When the magnet was lifted vertically but kept in the center, activation took place at about 6.2–8.9 mm and release at 7.2–9.6 mm. Changing the location of the magnet to the right, there was a wider variation. A straight right shift produced activation distances between 5.0–8.2 mm and release distances between 6.0–8.9 mm. When the magnet was transferred in a direction both to the right and upward, distances of activation of 5.0–7.9 mm and distances of release of 6.0–8.5 mm were recorded. This combined shift had the best performance with mean activation and release distances close to 7.1 mm and 7.6 mm. The centered was the position closest in spacing to allow the long average release distance. A one-way analysis of variance (ANOVA) with Tukey's test was performed to determine the significance of differences between the five orientations. There was no significant difference between groups in activation distances ($F(4, 45) = 1.86$, $p = 0.135$). The effect of release distances was significant ($F(4, 45) = 3.29$, $p = 0.019$). The post test was used to split the release values into two statistical groups. The right shift - upwards pattern was captured in Group B and displayed a reduced release distance in comparison with the centered pattern, which formed Group A.

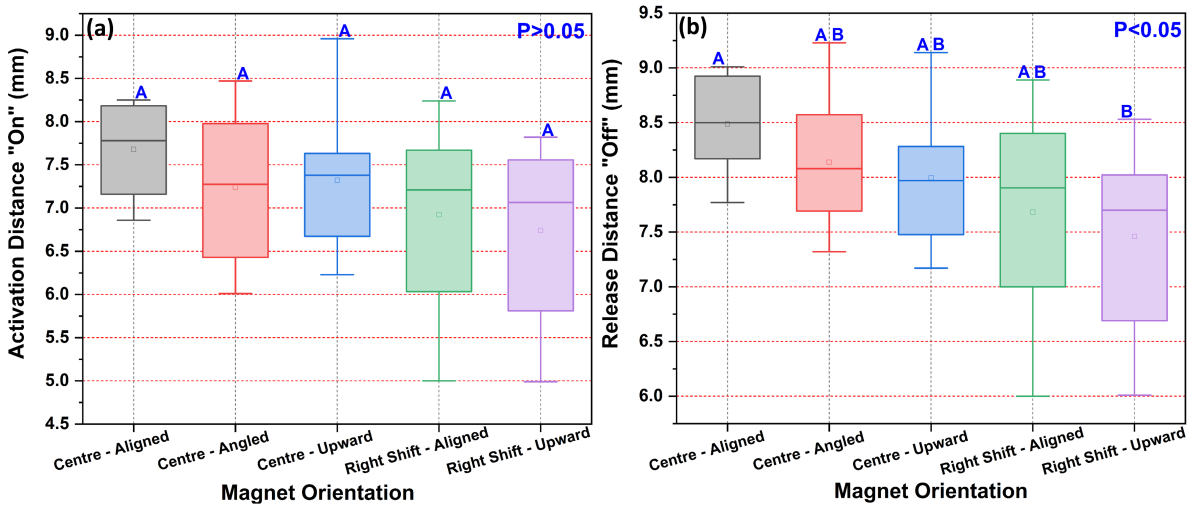

Fig. 3.17 Activation and release distances of reed sensors tested under five magnet orientations, including statistical separations obtained through one-way ANOVA to identify orientation-dependent behavior. Letters indicate statistical groupings for (a) "On" (one-way ANOVA, $p > 0.05$) and (b) "Off" distances (one-way ANOVA, $p < 0.05$). Data are mean ± SD (n = 10).

These results indicate that the position of the magnet influences the release of the sensor, which is relevant to obtain a significant break in the electrical path. The reeds in the glass capsule only close when the magnitude of the magnetic force on the reeds is greater than the stiffness of the blades. That force is dependent on the strength of the field, and the fact that it changes very rapidly near the reed tips. The centered setup results in a balanced field but it also necessitates working the field across the largest gap and thus resulting in the longest switching distances. In the case of a right shift-upward (On: 7.1 mm, Off: 7.6 mm), due to a lateral shift and a vertical shift, one pole is closer to the reeds. The local field becomes stronger and changes more steeply, which increases the force on the blades and allows to switch to a greater distance from the center of the magnet. The angled and upward only positions produce an unbalanced field and may not drive both reeds as well, hence the mid-range and less stable measurements of the two. The behavior is related to the underlying physics of the magnetic interaction and demonstrates that one has to be careful with where the magnet is placed when designing magnet assembly to be inserted into tight automotive layouts.

The changes in the switching distances observed indicate that the consistency of the sensor depends on the way in which a magnet is positioned. Using a magnet of a different flux level would change the sensor response as well. The contents of the material holding the components makes a difference too. The PLA that was fabricated according to FDM provided sufficient stiffness to keep the magnet and sensor in alignment. It is a low mass object with a simple structure which allowed it to measure accurately. This approach had decreased error, reduced cost, enabled quick fabrication and made it possible to test all orientations of the magnet.

3.3.2 Prototype Testing and Spring Integration

The second phase of our study focused on developing and evaluating a spring-integrated reed sensor prototype to enhance mechanical stability and switching consistency. A stainless-steel spring was integrated into a PBT housing via an interference-fit slot, maintaining tension and direct mechanical coupling with the reed switch terminals. The prototype was tested in four configurations, combining two spring orientations, i.e., parallel (0°) and perpendicular (90°) to the terminals, and with two types of terminal geometry as straight and bent which are also shown in Figure 3.18.

Introducing the preloaded spring significantly improved contact stability. Figure 3.18 shows activation–release profiles for all four mechanical configurations. The bent-terminal with rotated-spring design exhibited the best performance, reducing activation hysteresis to 0.4 mm and achieving average activation and release distances of 2.3 mm and 2.7 mm, respectively. When compairing the results of straight-terminal configuration, we observed that with an aligned spring produced significantly higher values as 4.7 mm (activation/ on) and 5.4 mm (release/ off). The outcomes may highlight the significance of magnet orientation, spring orientation, and terminal geometry for effective and reliable performance of reed sensors.

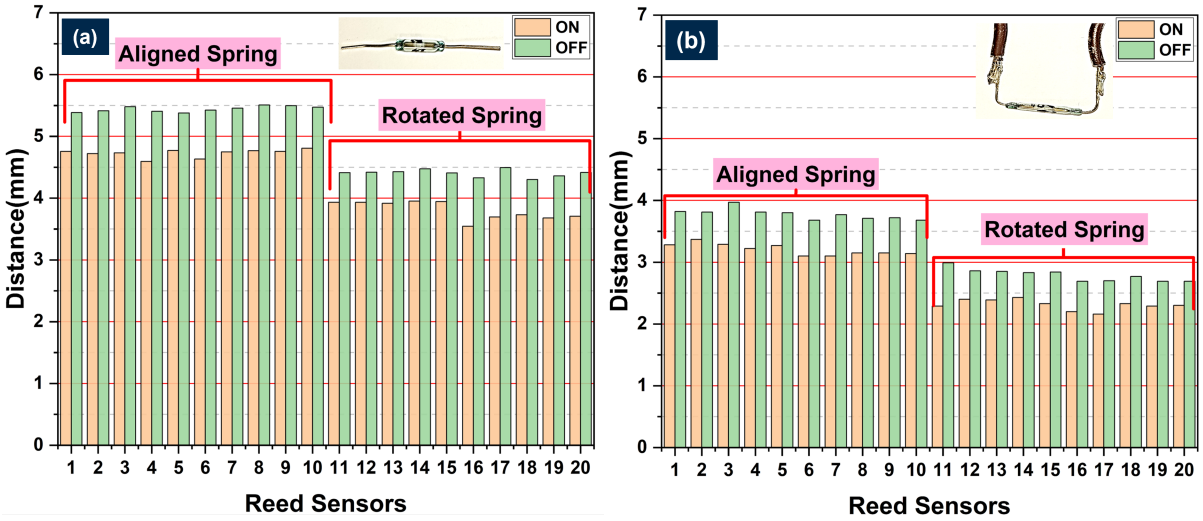

Fig. 3.18 Switching-distance results for reed sensors incorporating straight or bent terminals and two spring orientations, demonstrating the effect of mechanical preloading on sensitivity: (a) straight and (b) bent terminals under aligned and rotated spring orientations.

3.3.3 Practical Integration and Design Considerations

The final sensor prototype with features like compact, lightweight, and manufactured entirely through additive techniques could be installed for various EV applications. Notably, it possess strong potential for integration into battery-module interlock systems, cover-lid detection units, and coolant-level monitoring circuits. The use of SLS-fabricated PBT allows flexible adaptation to various geometries and maintains mechanical integrity even in relatively high temperatures. An example of a reed sensor is shown in (Figure 3.19).

If we focus on the system-level applications, the reed sensor can be combined with micro controllers for state feedback or safety cut-off functions. Its integration into a smart diagnostic network would allow real-time detection of lid closure, isolation breach, or misalignment, which may indicate its importance in improving both safety and maintenance scheduling. For further advancement and for more improved design, one may incorporate embedded shielding to further reduce electromagnetic susceptibility, or alternative actuator magnets with temperature-stable flux densities.

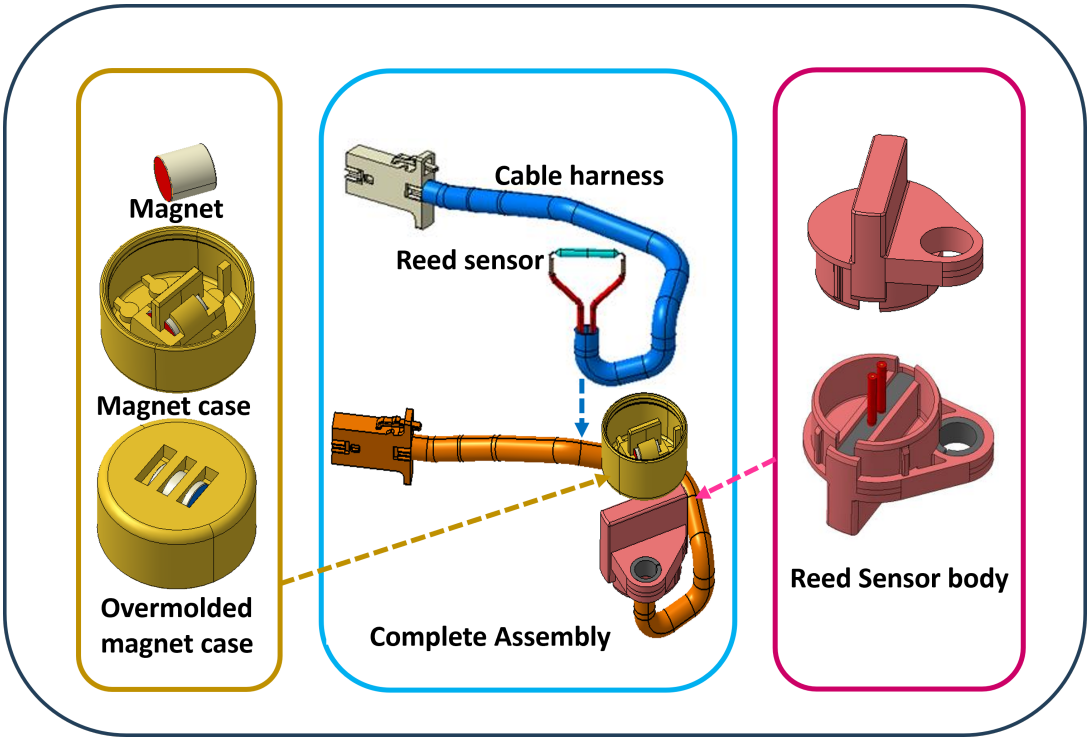

Fig. 3.19 Fully assembled spring-integrated reed-sensor prototype designed for EV applications, showing the compact PBT housing and protected internal components.

3.3.4 Summary

The mechanical optimization of the reed sensors achieved through spring integration and terminal redesign resulted into a reliable and repeatable reed sensor for realistic automotive conditions.

- The baseline study made a comparison of five magnet orientations (defined in Figure 2.6), using the same measurement approach (setup in Figure 2.4 – 2.5).
- The most suitable magnet orientation based on activation and release distances were identified by the baseline results reported in Figure 3.17.
- The design was then improved with a spring stabilized design and four build variants (straight/bent terminals; spring at 0°/ 90°), which are shown and compared in Figure 3.18.
- Comparative results in Figure 3.18 enable the best final configuration bent terminals + rotated spring to be selected.
- The optimized prototype was enable to obtain 2.3 mm activation and 2.7 mm release distances, as reported in Figure 3.18.
- The optimized design also exhibited good repeatability of < 0.1 mm with standard deviation, based on the repeated switching tests in Figure 3.18.

- The device is designed to work between -20 °C to 80 °C as the defined operating conditions for the application.
- The final integrated prototype and packaging state are provided in Figure 3.19 that verify practical feasibility of the configuration of choice.

3.4 Functional Evaluation of Laser-Induced Graphene (LIG) on Bio-Polymer Substrates

The rapid growth of flexible electronics demands scalable, environmentally responsible fabrication techniques and carbon-based materials that avoid reliance on petroleum-derived polymers. In this context, in our fourth experimental study we explored the fabrication and performance of laser-induced graphene (LIG) films on lignin-based biopolymer substrates as a sustainable alternative for conductive patterns and flexible electronic components in electric-vehicle (EV) applications. The aim of our investigation was to optimize laser-processing parameters, examine the influence of coating formulation on electrical and structural properties of LIG film/ foam, and fabrication of interdigitated capacitors (IDCs) using optimized laser parameters and bio-polymer formulations. This work bridges sustainable material design with functional performance optimization and device integration.

3.4.1 Optimization of Laser Processing Parameters

Initial process optimization was conducted to identify laser power and scanning conditions that produce uniform graphitization without substrate degradation. LIG was generated using a 30 W CO_2 pulsed laser (wavelength 10.6 μm), operated at fixed parameters: 450 DPI, 5 kHz frequency, and 200 mm s^{-1} scan speed. Before selection of power sequence of laser, six test regions were irradiated using different power settings: (i) 20 %, (ii) 15 %, (iii)10 %, (iv) 5 %, (v) 3 %, and (vi) a two-pass sequence (3 % followed by 1 %). High powers (20 % and 15 %) caused substrate ablation and film detachment, while moderate power (10 %, and 5 %) produced irregular but partially graphitized surfaces.

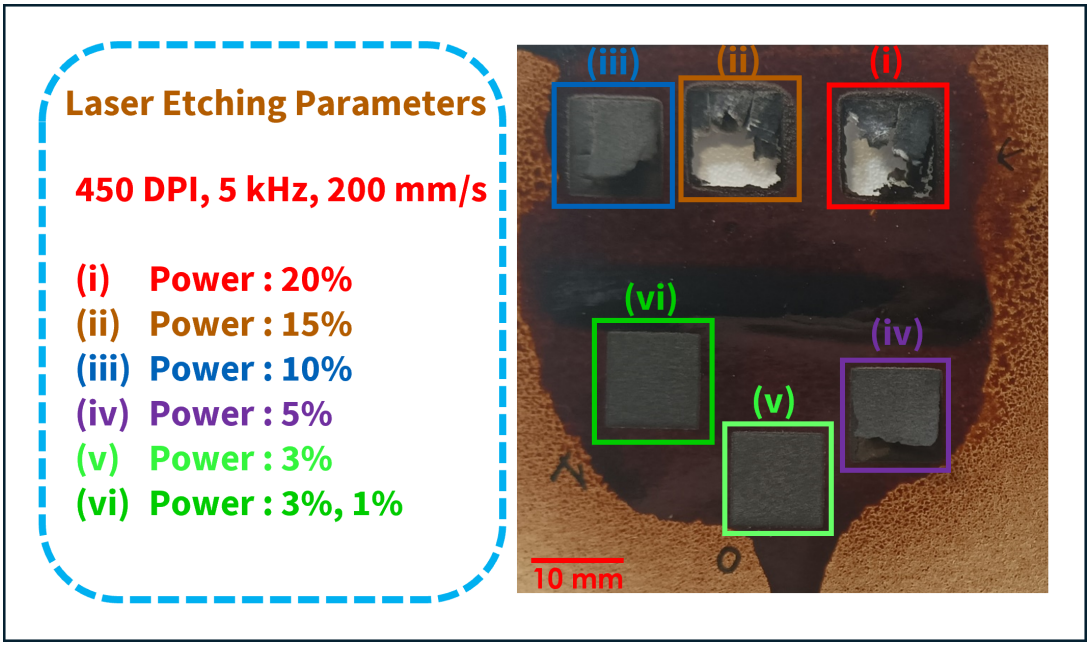

Fig. 3.20 Laser-power optimization for lignin-based LIG, showing differences in pattern uniformity and substrate stability across single- and multi-pass irradiation sequences from 20% to 1% power at 450 DPI, 5 kHz, and 200 mm/s.

At high powers (>10 %), due to severe carbonization and localized delamination it appears that there is excessive energy input and poor thermal confinement. Among the examined sequences, the 3 % settings yielded uniform, dark LIG with improved definition and minimal damage. The two-pass low-power sequence (3 %, 1 %) produced the most consistent surface with high contrast and structural integrity, confirming it as the optimal setting for localized carbonization without thermal degradation. The purpose was to avoid burn through and blistering of LIG film as shown in Figure 3.20. The outcomes of this optimization process may also indicate that a mild multi-pass laser exposure allows gradual lignin carbonization and prevents overheating, thereby preserving substrate integrity.

3.4.2 Influence of Coating Formulation on Conductivity

After optimization of the power of laser and observing the impact of energy modulation on LIG quality, three distinct power sequences were applied: LIG–1 (3% + 1%), LIG–2 (1% + 3% + 1%), and LIG–3 (1% + 1% + 1%) for all nine formulations for optimization of sheet resistance followed by fabrication of complex circuits using most suitable formulation and laser parameters. The purpose of our study was to check the effect of lignin type (EKWZ, SWWZ) and additives (PG, HMF, formaldehyde, and urea, etc.) on sheet resistance values.

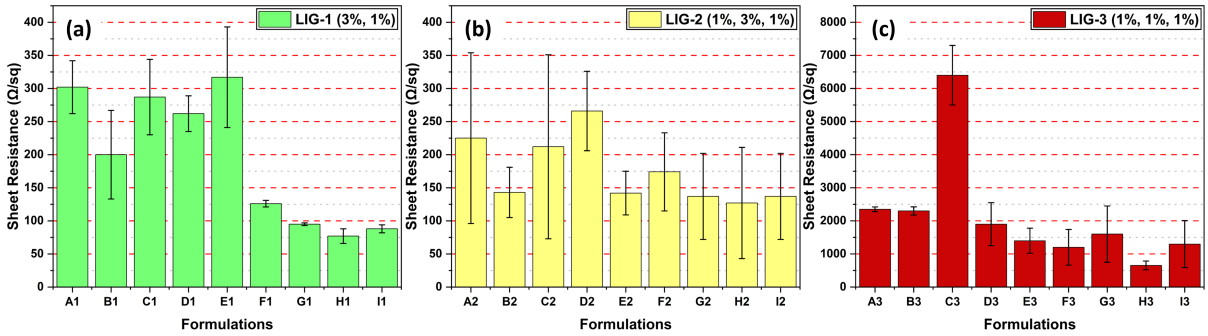

Fig. 3.21 Sheet-resistance comparison of LIG films produced using three laser-power protocols across nine lignin-based formulations, illustrating the combined influence of coating chemistry and energy input: (a) LIG 1 (3% + 1%), (b) LIG 2 (1% + 3% + 1%), and (c) LIG 3 (1% + 1% + 1%).

Figure 3.21 shows that formulations G, H, and I consistently yielded the lowest sheet resistance across all laser protocols, particularly under LIG-1, where values dropped below 100 Ω/sq. These coatings shared moderate PG content (10–20%) and relied on EKWZ or SWWZ lignin (Table 2.1), both contributing to favorable film morphology and thermal response. H1, with 70% PG, remained highly conductive but showed weaker post-wash stability (Figure 3.23). The slightly higher resistance of I, despite containing formaldehyde, suggests that while cross-linked networks support structural retention, they may limit graphitization efficiency when not balanced with carbon-rich soft segments. SWWZ-based formulations (I) demonstrated better conductivity under milder laser conditions, possibly due to more uniform thermal breakdown. So, lignin origin and additive composition directly affected carbon conversion to form LIG and its conductivity, and among all formulations, the formulation with PG systems showed better performance under optimized conditions.

Morphology of the LIG films indicates that the presence of PG likely increased the plasticity of the coating, facilitating localized melting and carbon clustering during graphitization. Over-plasticized films (>70 wt % PG) occasionally exhibited micro-blistering and flake detachment, indicating that mechanical cohesion may limit the extent of formulation optimization. The results outcome further indicate that chemical formulation, as much as laser power, governs the success of LIG generation from lignin-based coatings. Across laser sequences, LIG-1 $\gg$ LIG-2 $\gg$ LIG-3 in conductivity. The first high-energy pulse (3 %) in LIG-1 initiated rapid surface pyrolysis, followed by a mild 1 % refinement that reduced roughness and improved graphitic ordering. In LIG-2, mid-sequence 3 % pulse yielded uneven carbonization and poor reproducibility, while LIG-3 failed to reach the energy threshold needed for full conversion. The optical comparison in Figure 3.22 shows LIG-1 surfaces as dark and continuous, LIG-2 as patchy, and LIG-3 as faint gray.

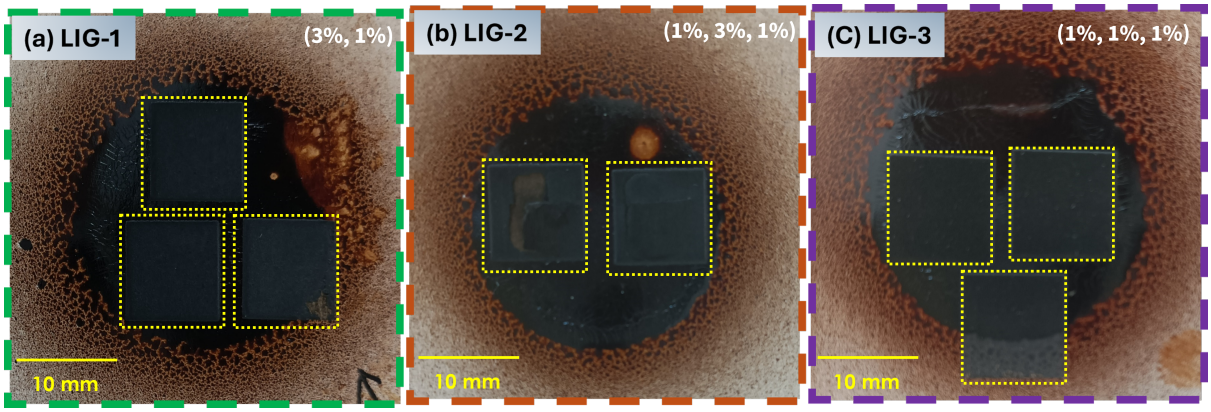

Fig. 3.22 Surface morphology of a 10 mm × 10 mm LIG pattern produced under optimized low-power conditions, showing continuous and well-defined graphitized regions.

3.4.3 Fabrication of LIG-Based Interdigitated Capacitors (IDC)

After optimizing laser parameters and lignin formulations, we shifted to device-level and employed IDCs fabrication on the best-performing coatings (G, H, I) using the LIG-1 protocol. Each IDC consisted of ten interdigitated fingers with a fixed gap of 0.10 ± 0.01 mm, defined directly by the laser path. After performing laser etching, the samples were immersed in deionized water for 2 min to remove unconverted resin and enhance contrast (Figure 3.23). This post-wash treatment improved edge definition and pattern adhesion without affecting conductivity. Optical inspection of IDCs indicates clean pattern edges with no visible cracking in case of formulation I. After drying the specimens in oven, we performed initial electrical tests to ensure that there is no short-circuit between the fingers of IDCs which confirms the basic capacitor functionality.

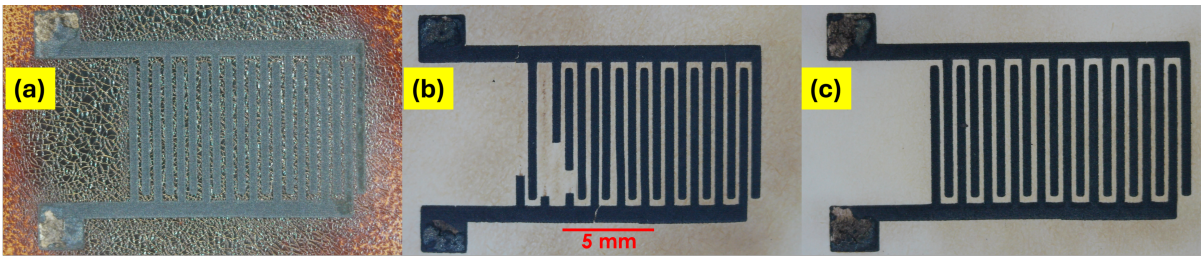

Fig. 3.23 Visual comparison of LIG traces before and after water-washing for two formulations, showing improved surface clarity and structural retention following removal of unconverted coating. (a) before water washing of H (b) after water washing of H, and (c) formulation I.

3.4.4 Mechanistic Interpretation

The structure–property relationship emerges from the synergy between laser-energy input and coating chemistry. Moderate fluences induce rapid pyrolysis of lignin's aromatic units, producing amorphous carbon clusters that reorganize into graphene-like domains. Propylene glycol acts

as a plasticizer that delays mass loss and facilitates uniform carbon layer formation. HMF and formaldehyde contribute cross-linking that stabilizes film geometry but excessive cross-linking impedes carbon conversion. Thus, an optimal balance of soft and rigid additives maximizes conductivity and film adhesion.

The dual-pass laser strategy creates a thermal gradient that first initiates carbonization and then anneals defects, reducing micro-cracks and enhancing lattice ordering. The final LIG structure is a porous, few-layer graphene network anchored to the cellulosic paper via carbonized interfacial bridges, ensuring both electrical continuity and mechanical compliance.

3.4.5 Summary

- **Optimal laser protocol:** LIG-1 (3 % + 1 %) yielded uniform, conductive films without substrate damage.
- **Best formulations:** G, H (20–70 % PG) and I (10 % PG, SWWZ lignin).
- **Minimum sheet resistance:** $< 100\ \Omega\ \mathrm{sq}^{-1}$.
- **Energy consumption:** lower than conventional printing.

Our study demonstrates that controlled laser irradiation of lignin-PG coatings enables formation of mechanically robust and highly conductive graphene-like films. Notably, we can say that such films can be directly patterned into functional electronic elements without masks or solvents, offering a sustainable pathway for low-cost flexible electronics and EV sensor integration.

3.5 Chapter 3 Summary

This chapter presented a comprehensive evaluation of the four key component studies which form technical foundations of our PhD research: ionic-liquid-modified CFRP nanocomposites, digitally optimized copper busbars, mechanically stabilized reed sensors, and lignin-derived laser-induced graphene films. Each system demonstrated measurable improvements in its respective performance domain. The cumulative findings confirm that sustainable materials design, predictive modeling, and cross-component synergy can together yield lighter, safer, and more efficient energy-storage architectures for electric vehicles. These outcomes form the conceptual basis for the system-level integration.

Chapter 4

System-Level Integration and Discussion

4.1 Functional Coupling Across Subsystems

The component innovations that are presented in this work i.e. CFRP nanocomposites, copper busbars, reed sensors, lignin-based laser induced graphene (LIG) address different domains of EV battery design. They are a modular platform that integrates structural, electrical and sensing functionality together in a single system.

At the structure level, ionic-liquid-modified CFRPs are able to provide the mechanical stiffness of enclosure panels needed while taking part in electrical dissipation and vibration damping. The electrical domain benefits from the digital optimization of copper busbar for minimal resistive losses and temperature increase for better energy efficiency during charge/discharge. The sensing layer mounts by mechanically stabilized reed switches is responsible for the principle of accurate feedback on the position, safety interlocking shaking and thermal fluctuation. The electronics layer which represents the LIG circuitry allows for lightweight, sustainable components that can be used in the diagnostic process and be embedded directly within the housing.

The synergy of these layers stemmed from their joint importance on multi-functionality, i.e., each sub-system meets its main purpose while providing auxiliary benefits such as reducing weight, energy efficiency or environmental compatibility.

4.2 Comparative Performance Assessment

4.2.1 Structural Integrity

The flexural strength of the CFRP laminates was found to be around 803 MPa and their modulus is close to 88 GPa, which is more than the level found in conventional aluminum alloys that have been used in similar enclosures. The incorporation of 3 wt% MWCNTs enhanced not only

the load carrying capacity, but also improved damping performance of battery modules. These improvements totally allow for the use of thinner enclosure panels, which reduces the overall system weight without any loss of mechanical protection.

4.2.2 Electrical Efficiency

Digital twin analysis of copper busbars proved that for current range of 100 A to 500 A corresponding voltage drop which is in the range of 0.009 V to 0.047 V is well within the limit of the industry use. With the simulation framework, parametric optimization allows the adjustment of busbar cross-sections as well as the weld geometry and the finalization of the cooling strategies before the physical prototyping. Such predictive capability allows for quicker development times and high consistency in terms of performance when operating in transient conditions with high current levels.

4.2.3 Sensing and Control

The mechanically stabilized reed sensors activated and released with 2.3 millimeters and 2.7 millimeters with little variance (< 0.1 millimeters). These metrics compare to a 60 percent reduction in hysteresis compared to unmodified designs. The small form factor, additively manufactured housings can be easily integrated into module lids/ busbar brackets and offer high levels of mechanical feedback for interlock and isolation functions.

4.2.4 Sustainable Electronics

LIG-based interdigitated capacitors attained on lignin coatings presented sheet resistance less than 100 Ω sq^{-1} and stable capacitance on the frequency range up to 100 kHz. The low-energy (energy input is approximately 12 kWh m^{-2}) and solvent-free laser process allows the laser process to be scaled for environmentally conscious manufacture. These devices could be modified to strain, humidity or temperature sensing when used in coupled condition with very simple readout electronics.

4.3 Contribution in Modular Battery-Pack Architecture

The results provide support for the conception of a battery-pack layout in which each layer makes a contribution to battery performance and sustainability:

1. **Outer structural shell** – Stiffness, insulation and vibration damping CFRP nanocomposite panels.

2. **Power-distribution layer** – Copper busbars that are optimized using digital twin simulations to have an efficient current routing design across the board and minimize the thermal gradient throughout.

3. **Sensor array** – Spring stabilized reed switches for the mechanical feedback and system safety measures.

4. **Embedded Circuitry** – LIG-based flexible electronics printed onto internal polymer or paper substrates to provide a means of diagnostics on a real time basis.

This multilayer design philosophy allows this high functional density, and still makes the assembly as easy as possible. It also makes it easier to disassemble and recycle, as components can be separated by what material they are made of and would not require complicated adhesives or coatings.

4.4 Durability, Reliability, and Scalability

Each of the subsystems needs to meet automotive qualification standards before commercial integration. The CFRP composites need a long-term thermal-aging testing in order to validate long-term modulus retentions. The busbars although electrically efficient had localised softening at welds; reconnection of reinforcement strategies should follow the results of finite element thermal cycling and fatigue analysis. The reed sensors were successfully tested with laboratory vibration testing but still need to be tested in the combined environment stress (temperature, humidity, and electromagnetic interfacing). The LIG devices have to be tested for stability under constant bias and exposure to electrolyte vapours.

From a manufacturing point of view, the four processes that are possible, i.e. vacuum bagging, laser welding, additive manufacturing and laser etching all have the advantage of being scalable with currently available industrial equipment, thus, it is a strong point in favor of easy transition from lab to pilot scale production.

4.5 Sustainability and Life-Cycle Considerations

Environmental performance is an implicit measure of engineering success. The replacement of aluminum and solvent-based polymers with CFRP and lignin substrate allows meaningful energy consumption and chemical emission reductions. The LIG process removes dangerous solvents and allows local and customized circuit manufacturing, and less waste. Copper busbars, although being energy intensive to manufacture, are 100% recyclable, and the resulting increase in efficiency indirectly reduces the system energy losses.

A life-cycle assessment LCA including these aspects would be likely to provide evidence of cumulative (material, manufacturing, operational phase) environmental benefits. By designing with functionality as well as recyclability, the proposed architecture is in accordance with the EU and UNECE directive level aiming for circular economy in accordance with the automobile industry.

4.6 Limitations and Opportunities

The major limitation in the present study is that there is no fully integrated prototype with simultaneous operations of all the subsystems. Differences in the curing cycles, thermal expansion, and electrical potential between layers may be an integration challenge. In the future, a way of hybrid manufacturing, which enables co-cure of composite panels with sensors embedded inside their parts and conductible traces, should be explored.

Further refinement of the digital-twin model leading to the inclusion of mechanical damping and fatigue parameters would increase its predictive value to lifetime estimation. The LIG electronics, although they work sufficiently, could benefit from controlled atmosphere processing and gain conductivity and stability. Likewise, wider testing of Reed Switch endurance to temperature-humidity environment will complete their reliability credentials.

4.7 Broader System Perspective

The integration framework proposed here is a representation of the path to be followed to achieve multifunctional, sustainable design in advanced mobility systems. It shows the convergence of high mechanical performance, electrical reliability and environmentally appropriate functionality emerges by means of interdisciplinary material choice and digital design.

By combining experimental evaluation with computational modeling, the methodology under development shortens the development cycles while permitting the augmentation of predictive accuracy. This approach can go beyond the EV battery packs and apply to other high-density electro-mechanical assemblies such as aerospace energy modules, stationary energy storage units and renewable energy converters.

Chapter 5

Conclusions and Future Work

5.1 Overview

This doctoral research investigated the use of a multidisciplinary technique that would enhance the performance of electric vehicle (EV) battery system by having innovations in the materials used and the design of components, as well as processing into environmentally conscious use. The investigation covered four inter-linked domains: (i) multifunctional carbon fibre reinforced polymer (CFRP) composites with ionic liquid treated carbon nanotubes; (ii) digital twin modeling and experimental evaluation of copper busbars; (iii) mechanical optimization of reed sensors for use in vibration prone environments; (iv) sustainable laser induced graphene (LIG) circuits using lignin-based biopolymer on paper substrates.

Each of the studies delivered independent technical innovations as well as advancements towards an integrated and modular framework for next-generation EV battery technologies. The collective results show that the combination of light-weight structural materials, predictive digital modeling, mechanical refinement and sustainable electronics can result in a high performance and environmentally consistent battery system.

5.2 Summary of Key Findings

(i) Multifunctional CFRP Nanocomposites

Incorporation of Pristine Multi-walled Carbon Nanotubes (MWCNTs) Treated by ionic liquid [BMIM][Tf_2N] Enhances Flexural Strength up to 803 MPa and Modulus up to 88 GPa and reduces electrical resistance to $\approx$ 30 Ω. The improvement was attributed to better nanotube dispersion and adhesion at the interface which was supported by the dynamic mechanical analysis ($E' \approx$ 18 GPa) and SEM-FTIR characterization. The work proved the feasibility of designing

the CFRP enclosures to satisfy simultaneously the structural and electrical requirements for battery modules.

(ii) Digital-Twin Optimization of Copper Busbars
A coupled electrical-thermal-mechanical simulation that was developed in COMSOL Multiphysics 6.3. accurately predicted (from 0.009 V to 0.047 V) voltage drop, and temperature rise (around 273 °C at 500 A) for different busbar geometries; The model's outputs correlated closely (within ±6 %) with experimental data. Mechanical and metallurgical evaluations revealed high weld integrity with minor strength reduction in the fusion zone. The digital-twin approach therefore enables data-driven optimization, reducing prototyping cycles and improving thermal reliability.

(iii) Mechanically Stabilized reed Sensors
Mechanical redesign of reed-switch housings and with a stainless-steel spring and bent-terminal geometry, reduced the activation distance by approximately 60 %, i.e. achieved consistent actuation at 2.3 mm with < 0.1 mm standard deviation. The sensors retained stable operation confirming suitability for EV battery monitoring. The results demonstrate that simple mechanical adjustments can yield significant improvements in reliability for low-power, contact-based sensors.

(iv) Sustainable LIG Electronics on Lignin Substrates
Laser-induced graphene patterns fabricated under a 3 % + 1 % (LIG-1) power sequence produced conductive films with sheet resistances below 100 Ω sq^{-1}. Devices fabricated as interdigitated capacitors exhibited stable performance up to 100 kHz and mechanical flexibility over 100 bending cycles. The solvent-free, low-energy process ($\approx$ 0.2 kWh m^{-2}) validated a sustainable route for flexible electronics compatible with circular manufacturing principles.

5.3 Integrated Contributions

The four studies provide a repeatable methodology of coupling the structural, electrical, and sustainability goals within the EV battery design. The thesis contributes:

1. **Material-level innovation** – Demonstration of the dispersion of Multifunctional CFRPs using ionic liquid supported MWCNTs.
2. **Digital engineering methodology** – Installation of an validated multiphysics digital twin for predictive thermal-electrical modeling.
3. **Mechanical reliability enhancement** – Design development of a miniaturized vibration tolerant reed sensor fabricated by additive manufacturing.

4. **Sustainable process integration** – Presenting an environmentally convenient (eco-efficient) fabrication pathway of LIG as a process integration for components display.

These advancements generate new rules for component engineering with EV battery systems. It represents the work in addition to isolated optimizing and represents a way forward to an integrated design in terms of function and functionality for the future of vehicle electrification.

5.4 Limitations

While the research has achieved the main targets of the project, there are a number of limitations that have to be recognized:

- **Scale-up effects:** Fabrication of nanocomposites was restricted to laboratory-scale laminates; uniformity of the processes and void levels in large panels must be validated.
- **Joint reliability:** The insufficiency of mechanical weakening phenomenon at laser weld busbar joints requires further improvement through post weld treatment or hybrid joining.
- **Environmental testing:** Reed sensors were not tested under combined temperature-humidity cycles which could have an affect on long term reliability.
- **Electrical stability:** For LIG devices accelerated aging tests are needed to determine the conductivity retention under bias as well as exposure to humidity or electrolyte vapors.
- **System integration:** A fully functional prototype with the combination of all four subsystems was not assembled in the project time frame; therefore the compatibility within interfaces is still to be verified experimentally.

The above constraints provide a road map for targeted improvements in the fully functional battery pack model as well as open window for future research to meet the sustainability goals.

5.5 Recommendations for Future Work

1. **Integrated Module Development:**
   Fabrication of battery-module prototype having CFRP housings and other structural parts, modified busbar designs, reed sensors with integrated spring, and LIG based devices, to check the real-world integration challenges which include thermal mismatch, EMC/ EMI shielding, and mechanical performance.

2. **Advanced Modeling:**
   Expand digital twin to fatigue, vibration, and electrochemical–thermal behavior etc., to develop lifetime prediction and predictive maintenance modeling of the components.

3. **Sustainability Analysis:**
   Conduct a complete life cycle assessment (LCA) of materials, manufacturing and operational phases on environmental impacts and compare to the standard aluminum-polymer assemblies.

4. **Material Circularity and Recycling:**
   Investigate recyclable epoxy matrices or bio-based resins that are compatible with carbon fibres, ionic liquids in order to achieve an even greater end of life recover-ability

5. **Industrial Collaboration:**
   Get involved with automotive manufacturers and Tier-1 suppliers in a process study for scalability, standards, such as UN ECE R100, and ISO 26262, and economical for mass production.

5.6 Final Remarks

This thesis shows that cross-disciplinary innovation, such as, materials science, mechanical engineering & sustainability can lead to real-world progress in EV battery system design. By using both experimental research and study using simulations, the work offers a blueprint for future development of multifunctional and resource-efficient components.

The methodologies and findings presented herein provide the foundation for a new generation electric vehicle technologies in which, instead of performing safety and sustainability compete each other, they could coexist. Further improvement and integration of such approaches are expected to foster the gradual shift towards cleaner, smarter and durable energy-storage options for the global transport sector.

References

[1] Yi Wan and Jun Takahashi. Development of carbon fiber-reinforced thermoplastics for mass-produced automotive applications in japan. *Journal of Composites Science*, 5(3):86, 2021.

[2] K Srinivasa Kishore and K Venkata Subbaiah. Carbon fiber and carbon fiber reinforced epoxy composites for automotive applications-a review. *Journal of Advanced Research in Applied Sciences and Engineering Technology*, 29(3):272–282, 2023.

[3] Kinjalkumar Patel, Prasad Potluri, Zeshan Yousaf, and Arthur Wilkinson. Multi-scale reinforcement of epoxy composites-use of carbon fibre fabrics coated with an epoxy binder containing mwcnts for improved interlaminar fracture resistance. *Composites Part B: Engineering*, 165:109–119, 2019.

[4] Xiang Ren, Muhammad M Sherif, Yaoyao Wei, Yuhui Lyu, Yamin Sun, and Osman E Ozbulut. Effect of corrosion on the tensile and fatigue performance of cfrp strand sheet/steel double strap joints. *Engineering Structures*, 260:114240, 2022.

[5] Kathleen Moyer, Chuanzhe Meng, Breeanne Marshall, Osama Assal, Janna Eaves, Daniel Perez, Ryan Karkkainen, Luke Roberson, and Cary L Pint. Carbon fiber reinforced structural lithium-ion battery composite: Multifunctional power integration for cubesats. *Energy Storage Materials*, 24:676–681, 2020.

[6] Jaehoon Choi, Omid Zabihi, Russell J Varley, Bronwyn Fox, and Minoo Naebe. High performance carbon fiber structural batteries using cellulose nanocrystal reinforced polymer electrolyte. *ACS Applied Materials & Interfaces*, 14(40):45320–45332, 2022.

[7] Sónia Simões. High-performance advanced composites in multifunctional material design: State of the art, challenges, and future directions. *Materials*, 17(23):5997, 2024.

[8] Maria Francesca Pernice, Guocheng Qi, Evgeny Senokos, David B Anthony, Sang Nguyen, Maria Valkova, Emile S Greenhalgh, Milo SP Shaffer, and Anthony RJ Kucernak. Mechanical, electrochemical and multifunctional performance of a cfrp/carbon aerogel structural supercapacitor and its corresponding monofunctional equivalents. *Multifunctional Materials*, 5(2):025002, 2022.

[9] Konstantina Zafeiropoulou, Christina Kostagiannakopoulou, Anna Geitona, Xenia Tsilimigkra, George Sotiriadis, and Vassilis Kostopoulos. On the multi-functional behavior of graphene-based nano-reinforced polymers. *Materials*, 14(19):5828, 2021.

[10] Sifiso John Skosana, Caroline Khoathane, and Thomas Malwela. Driving towards sustainability: A review of natural fiber reinforced polymer composites for eco-friendly automotive light-weighting. *Journal of Thermoplastic Composite Materials*, 38(2):754–780, 2025.

[11] M Senthil Kumar, G Sakthivel, R Jagadeeshwaran, J Lakshmipathi, M Vanmathi, T Mohanraj, and Yesgat Admassu. Development of eco-sustainable silica-reinforced natural hybrid polymer composites for automotive applications. *Advances in Materials Science and Engineering*, 2022(1):5924457, 2022.

[12] Sarita Choudhary, Manoj Kumar Sain, Vikas Kumar, Praveen Saraswat, and Manish Kumar Jindal. Advantages and applications of sisal fiber reinforced hybrid polymer composites in automobiles: A literature review. *Materials Today: Proceedings*, 2023.

[13] David Blanco, Eva Maria Rubio, Raquel Maria Lorente-Pedreille, and Maria Ana Saenz-Nuno. Lightweight structural materials in open access: latest trends. *Materials*, 14(21):6577, 2021.

[14] Manojit Ghosh, Arkajit Ghosh, and Avinava Roy. Renewable and sustainable materials in automotive industry. *Encyclopedia of Renewable and Sustainable Materials*, 2020:162–179, 2020.

[15] Mengyuan Hao, Xin Qian, Yonggang Zhang, Jiaming Yang, Chunjie Li, Haoting Gong, Xuefei Wang, Piaopiao Wang, Li Liu, and Yudong Huang. Thermal conductivity enhancement of carbon fiber/epoxy composites via constructing three-dimensionally aligned hybrid thermal conductive structures on fiber surfaces. *Composites Science and Technology*, 231:109800, 2023.

[16] Mathew Olurotimi Adeoti, Tamba Jamiru, Taoreed Adesola Adegbola, Ibrahim Suleiman, Mohammed Abdullahi, and Basiru Philip Aramide. Selection criteria of polymer nanocomposites for electrical energy storage applications: A concise review. *Express Polymer Letters*, 19(2), 2025.

[17] Subin Antony Jose, Nicholas Cowan, Matthew Davidson, Giovanni Godina, Ian Smith, Justin Xin, and Pradeep L Menezes. A comprehensive review on cellulose nanofibers, nanomaterials, and composites: Manufacturing, properties, and applications. *Nanomaterials*, 15(5):356, 2025.

[18] Norizan Mohd Nurazzi, MR Muhammad Asyraf, Abdan Khalina, Norli Abdullah, Fatimah Athiyah Sabaruddin, Siti Hasnah Kamarudin, So'bah Ahmad, Annie Maria Mahat, Chuan Li Lee, HA Aisyah, et al. Fabrication, functionalization, and application of carbon nanotube-reinforced polymer composite: An overview. *Polymers*, 13(7):1047, 2021.

[19] Zihong Wu, Yan Zhao, Kang Yang, Juan Guan, Shaokai Wang, Yizhuo Gu, Min Li, Yiyu Feng, Wei Feng, and Robert O Ritchie. Enhancing the mechanical performance of fiber-reinforced polymer composites using carbon nanotubes as an effective nano-phase reinforcement. *Advanced materials interfaces*, 10(3):2201935, 2023.

[20] Vraj Shah, Jaydip Bhaliya, Gautam M Patel, and Kalim Deshmukh. Advances in polymeric nanocomposites for automotive applications: A review. *Polymers for Advanced Technologies*, 33(10):3023–3048, 2022.

[21] Ruoxi Chen, Yucheng Zhou, and Xiaodong Li. Cotton-derived fe/fe3c-encapsulated carbon nanotubes for high-performance lithium–sulfur batteries. *Nano Letters*, 22(3):1217–1224, 2022.

[22] Goteti Dhanaraju, Raj Kumar Pittala, B Satish Ben, Vinay Atgur, NR Banapurmath, MA Umarfarooq, Tabrej Khan, and Balbir Singh. Enhanced mechanical performance and damping behavior of cfrp composites through exfoliated mwcnt functionalization. *Nanocomposites*, 10(1):184–200, 2024.

[23] Avery D Brown, Charles E Bakis, and Edward C Smith. Effect of carbon nanotube surface treatment on the dynamic mechanical properties of a hybrid carbon/epoxy composite laminate. *Composites Science and Technology*, 231:109807, 2023.

[24] Shambhu Kumar, Akhilendra Singh, and Mayank Tiwari. Numerical and analytical modelling of effective thermal conductivity of multi-walled carbon nanotubes polymer nanocomposites including the effect of nanotube orientation and interfacial thermal resistance. *Nanocomposites*, 9(1):30–42, 2023.

[25] Junjie Chen. Electrical and thermal properties of epoxy matrix composite materials reinforced with multi-walled carbon nanotubes under different weight fraction conditions. *Authorea Preprints*, 2023.

[26] Giovanni Spinelli, Rosella Guarini, Liberata Guadagno, Luigi Vertuccio, and Vittorio Romano. Thermo-mechanical and thermo-electric properties of a carbon-based epoxy resin: An experimental, statistical, and numerical investigation. *Materials*, 17(14):3596, 2024.

[27] Cheng Zhang, Youquan Ling, Xueqin Zhang, Mei Liang, and Huawei Zou. Ultra-thin carbon fiber reinforced carbon nanotubes modified epoxy composites with superior mechanical and electrical properties for the aerospace field. *Composites Part A: Applied Science and Manufacturing*, 163:107197, 2022.

[28] Maziyar Sabet. Advanced functionalization strategies for carbon nanotube polymer composites: achieving superior dispersion and compatibility. *Polymer-Plastics Technology and Materials*, 64(4):465–494, 2025.

[29] NM Nurazzi, FA Sabaruddin, MM Harussani, SH Kamarudin, M Rayung, MRM Asyraf, HA Aisyah, MNF Norrrahim, RA Ilyas, N Abdullah, et al. Mechanical performance and applications of cnts reinforced polymer composites—a review. *Nanomaterials*, 11(9):2186, 2021.

[30] Hossein Mozaffarinasab and Masoud Jamshidi. Surface modification of carbon nanotubes by a bifunctional amine silane; effects on physical/mechanical/thermal properties of epoxy nanocomposite. *Progress in Organic Coatings*, 179:107521, 2023.

[31] Bidita Salahuddin, Shaikh N Faisal, Tajwar A Baigh, Mohammed N Alghamdi, Mohammad S Islam, Bing Song, Xi Zhang, Shuai Gao, and Shazed Aziz. Carbonaceous materials coated carbon fibre reinforced polymer matrix composites. *Polymers*, 13(16):2771, 2021.

[32] Yan Cao, Naeim Farouk, Nasser Mortezaei, Alexei Valerievich Yumashev, Majid Niaz Akhtar, and Arash Arabmarkadeh. Investigation on microwave absorption characteristics of ternary mwcnts/cofe2o4/feco nanocomposite coated with conductive pedot-polyaniline co-polymers. *Ceramics International*, 47(9):12244–12251, 2021.

[33] Muhammad Asif Zahoor Raja, Mohammad Sabati, Nabeela Parveen, Muhammad Awais, Saeed Ehsan Awan, Naveed Ishtiaq Chaudhary, Muhammad Shoaib, and Hani Alquhayz. Integrated intelligent computing application for effectiveness of au nanoparticles coated over mwcnts with velocity slip in curved channel peristaltic flow. *Scientific Reports*, 11(1):22550, 2021.

[34] Christopher Igwe Idumah. Novel advancements in green and sustainable polymeric nanocomposites coatings. *Current Research in Green and Sustainable Chemistry*, 4:100173, 2021.

[35] Kamila Domagała, Mario Borlaf, Jacqueline Traber, Dariusz Kata, and Thomas Graule. Purification and functionalisation of multi-walled carbon nanotubes. *Materials Letters*, 253:272–275, 2019.

[36] Raj Vardhan Patel, Anshul Yadav, and Jerzy Winczek. Physical, mechanical, and thermal properties of natural fiber-reinforced epoxy composites for construction and automotive applications. *Applied Sciences*, 13(8):5126, 2023.

[37] Mian Muhammad-Ahson Aslam, Hsion-Wen Kuo, Walter Den, Muhammad Usman, Muhammad Sultan, and Hadeed Ashraf. Functionalized carbon nanotubes (cnts) for water and wastewater treatment: preparation to application. *Sustainability*, 13(10):5717, 2021.

[38] Xin Sun, Jiacheng Bao, Kai Li, Morris D Argyle, Gang Tan, Hertanto Adidharma, Kaihang Zhang, Maohong Fan, and Ping Ning. Advance in using plasma technology for modification or fabrication of carbon-based materials and their applications in environmental, material, and energy fields. *Advanced Functional Materials*, 31(7):2006287, 2021.

[39] Hana Jung, Hoi Kil Choi, Yuna Oh, Hyunkee Hong, and Jaesang Yu. Enhancement of thermo-mechanical stability for nanocomposites containing plasma treated carbon nanotubes with an experimental study and molecular dynamics simulations. *Scientific reports*, 10(1):405, 2020.

[40] Sha Yu, Yun Wu, Qi Xue, Jun-Jie Zhu, and Yuanzhen Zhou. A novel multi-walled carbon nanotube-coupled coni mof composite enhances the oxygen evolution reaction through synergistic effects. *Journal of Materials Chemistry A*, 10(9):4936–4943, 2022.

[41] Maan Hayyan, Khalid M Abed, Amirah Azzouz, Adeeb Hayyan, and Mahmood KH AL-Mashhadani. Natural deep eutectic solvent-functionalized multiwall carbon nanotubes for lead removal from wastewater. *Chemical Engineering and Processing-Process Intensification*, 205:109961, 2024.

[42] Arya Uthaman, Hiran Mayookh Lal, Chenggao Li, Guijun Xian, and Sabu Thomas. Mechanical and water uptake properties of epoxy nanocomposites with surfactant-modified functionalized multiwalled carbon nanotubes. *Nanomaterials*, 11(5):1234, 2021.

[43] M Arif Fikri, AK Pandey, M Samykano, K Kadirgama, Mathew George, R Saidur, Jeyraj Selvaraj, Nasrudin Abd Rahim, Kamal Sharma, and VV Tyagi. Thermal conductivity, reliability, and stability assessment of phase change material (pcm) doped with functionalized multi-wall carbon nanotubes (fmwcnts). *Journal of Energy Storage*, 50:104676, 2022.

[44] Fatih Turan, Mehmet Guclu, Koray Gurkan, Ali Durmus, and Yener Taskin. The effect of carbon nanotubes loading and processing parameters on the electrical, mechanical, and viscoelastic properties of epoxy-based composites. *Journal of the Brazilian Society of Mechanical Sciences and Engineering*, 44(3):93, 2022.

[45] Asieh Sadat Kazemi, Zahra Ebrahim Nataj, Yaser Abdi, and Mohammad Ali Abdol. Tuning wettability and surface order of mwcnts by functionalization for water desalination. *Desalination*, 508:115049, 2021.

[46] Vishal Dutta, Ritesh Verma, C Gopalkrishnan, Min-Hao Yuan, Khalid Mujasam Batoo, R Jayavel, Ankush Chauhan, Kun-Yi Andrew Lin, Ravindran Balasubramani, and Suresh Ghotekar. Bio-inspired synthesis of carbon-based nanomaterials and their potential environmental applications: a state-of-the-art review. *Inorganics*, 10(10):169, 2022.

[47] Kelvii Wei Guo. Carbon nanotubes synthesized by green/eco-friendly technique potential for bioenergy applications. *Nanomaterials in Biofuels Research*, pages 251–274, 2020.

[48] Elham Ezzatzadeh, Fatemeh Sheikholeslami-Farahani, Khadijeh Yadollahzadeh, and Sobhan Rezayati. Highly efficient reusable carboxy group functionalized imidazolium salts for a simple and cost-effective preparation of pyrano [2, 3-d] pyrimidinone derivatives. *Combinatorial Chemistry & High Throughput Screening*, 24(9):1465–1475, 2021.

[49] Ederson R Abaide, Cristiano C Muller, Crisleine P Draszewski, Marcus V Tres, Marcio A Mazutti, and Giovani L Zabot. Chemistry of ionic liquid, switchable solvents, supercritical carbon dioxide and sub/supercritical water. *Advanced Nanotechnology and Application of Supercritical Fluids*, pages 165–198, 2020.

[50] Maryam Meshksar, Fatemeh Afshariani, and Mohammad Reza Rahimpour. Industrial applications of green solvents for sustainable development of technologies in organic synthesis. *Applications of Nanotechnology for Green Synthesis*, pages 435–455, 2020.

[51] Andromachi Tzani, Maria-Anna Karadendrou, Styliani Kalafateli, Vasiliki Kakokefalou, and Anastasia Detsi. Current trends in green solvents: biocompatible ionic liquids. *Crystals*, 12(12):1776, 2022.

[52] Julia L Shamshina and Paula Berton. Ionic liquids as designed, multi-functional plasticizers for biodegradable polymeric materials: a mini-review. *International Journal of Molecular Sciences*, 25(3):1720, 2024.

[53] Kirti Mishra, Nishu Devi, Samarjeet Singh Siwal, Qibo Zhang, Walaa F Alsanie, Fabrizio Scarpa, and Vijay Kumar Thakur. Ionic liquid-based polymer nanocomposites for sensors, energy, biomedicine, and environmental applications: roadmap to the future. *Advanced Science*, 9(26):2202187, 2022.

[54] Pranjal Ray and Meenakshi Pilania. The application and influence of ionic liquids in nanotechnology. *Materials Today: Proceedings*, 47:2835–2838, 2021.

[55] Liping Wei, Lin Wang, Ziwen Cui, Yingjun Liu, and Aihua Du. Multifunctional applications of ionic liquids in polymer materials: a brief review. *Molecules*, 28(9):3836, 2023.

[56] Karolina Matuszek, Samantha L Piper, Alina Brzęczek-Szafran, Binayak Roy, Saliha Saher, Jennifer M Pringle, and Douglas R MacFarlane. Unexpected energy applications of ionic liquids. *Advanced Materials*, 36(23):2313023, 2024.

[57] Kuilin Peng, Jie Lin, Deshuai Yang, Fangjia Fu, Zhongyang Dai, Guobing Zhou, and Zhen Yang. Molecular-level insights into interfacial interaction–nanostructure relationships of imidazolium-based ionic liquids around carbon nanotube electrodes. *Industrial & Engineering Chemistry Research*, 61(37):14051–14065, 2022.

[58] Tomás Pinheiro, Ricardo Correia, Maria Morais, João Coelho, Elvira Fortunato, M Goreti F Sales, Ana C Marques, and Rodrigo Martins. Water peel-off transfer of electronically enhanced, paper-based laser-induced graphene for wearable electronics. *ACS nano*, 16(12):20633–20646, 2022.

[59] R. M. Morais, D. H. Vieira, M. D. S. Ozório, G. L. Nogueira, A. Rollo, J. Kettle, and N. Alves. Green, biodegradable, and flexible resistive heaters-based upon a novel laser-induced graphene manufacturing process. *Advanced Sustainable Systems*, 8(10):2400166, 2024.

[60] João Coelho, Ricardo F Correia, Sara Silvestre, Tomás Pinheiro, Ana C Marques, M Rosário P Correia, Joana Vaz Pinto, Elvira Fortunato, and Rodrigo Martins. based laser-induced graphene for sustainable and flexible microsupercapacitor applications. *Microchimica Acta*, 190(1):40, 2023.

[61] Nan Zhao, Hanwen Zhang, Shuhong Yang, Yisheng Sun, Ganggang Zhao, Wenjun Fan, Zheng Yan, Jian Lin, and Caixia Wan. Direct induction of porous graphene from mechanically strong and waterproof biopaper for on-chip multifunctional flexible electronics. *Small*, 19(43):2300242, 2023.

[62] Housseinou Ba, Christophe Sutter, Vasiliki Papaefthimiou, Spyridon Zafeiratos, Armel Bahouka, Yannick Lafue, Lam Nguyen-Dinh, Thierry Romero, and Cuong Pham-Huu. Foldable flexible electronics based on few-layer graphene coated on paper composites. *Carbon*, 167:169–180, 2020.

[63] Jesper Edberg, Robert Brooke, Omid Hosseinaei, Andreas Fall, Kosala Wijeratne, and Mats Sandberg. Laser-induced graphitization of a forest-based ink for use in flexible and printed electronics. *npj Flexible Electronics*, 4(1):17, 2020.

[64] Tomás Pinheiro, Sara Silvestre, João Coelho, Ana C Marques, Rodrigo Martins, M Goreti F Sales, and Elvira Fortunato. Laser-induced graphene on paper toward efficient fabrication of flexible, planar electrodes for electrochemical sensing. *Advanced Materials Interfaces*, 8(22):2101502, 2021.

[65] Bohdan Kulyk, Marina Matos, Beatriz FR Silva, Alexandre F Carvalho, António JS Fernandes, Dmitry V Evtuguin, Elvira Fortunato, and Florinda M Costa. Conversion of paper and xylan into laser-induced graphene for environmentally friendly sensors. *Diamond and related materials*, 123:108855, 2022.

[66] Faisal Mahmood, Hanwen Zhang, Jian Lin, and Caixia Wan. Laser-induced graphene derived from kraft lignin for flexible supercapacitors. *ACS omega*, 5(24):14611–14618, 2020.

[67] Ali Ghavipanjeh and Sadegh Sadeghzadeh. Simulation and experimental evaluation of laser-induced graphene on the cellulose and lignin substrates. *Scientific Reports*, 14(1):4475, 2024.

[68] Maykel dos Santos Klem, Rodrigo Abreu, Tomás Pinheiro, João Coelho, Neri Alves, and Rodrigo Martins. Electrochemical deposition of manganese oxide on paper-based laser-induced graphene for the fabrication of sustainable high-energy-density supercapacitors. *Advanced Sustainable Systems*, 8(12):2400254, 2024.

[69] Xinzhi Sun, Xiaojuan Liu, and Feng Li. Sulfur-doped laser-induced graphene derived from polyethersulfone and lignin hybrid for all-solid-state supercapacitor. *Applied Surface Science*, 551:149438, 2021.

[70] Xining Zang, Caiwei Shen, Yao Chu, Buxuan Li, Minsong Wei, Junwen Zhong, Mohan Sanghadasa, and Liwei Lin. Laser-induced molybdenum carbide–graphene composites for 3d foldable paper electronics. *Advanced Materials*, 30(26):1800062, 2018.

[71] Hye-ran Moon and Byunghoon Ryu. Review of laser-induced graphene (lig) produced on eco-friendly substrates. *International Journal of Precision Engineering and Manufacturing-Green Technology*, 11(4):1279–1294, 2024.

[72] Kaichen Xu, Zimo Cai, Huayu Luo, Yuyao Lu, Chenliang Ding, Geng Yang, Lili Wang, Cuifang Kuang, Jingquan Liu, and Huayong Yang. Toward integrated multifunctional laser-induced graphene-based skin-like flexible sensor systems. *ACS nano*, 18(39):26435–26476, 2024.

[73] Sara L Silvestre, Maria Morais, Raquel RA Soares, Zachary T Johnson, Eric Benson, Elisabeth Ainsley, Veronica Pham, Jonathan C Claussen, Carmen L Gomes, Rodrigo Martins, et al. Green fabrication of stackable laser-induced graphene micro-supercapacitors under ambient conditions: toward the design of truly sustainable technological platforms. *Advanced Materials Technologies*, 9(16):2400261, 2024.

[74] Rajesh Kumar, Raghvendra Pandey, Ednan Joanni, and Raluca Savu. Laser-induced and catalyst-free formation of graphene materials for energy storage and sensing applications. *Chemical Engineering Journal*, 497:154968, 2024.

[75] Bohdan Kulyk, Beatriz FR Silva, Alexandre F Carvalho, Paula Barbosa, Ana V Girão, Jonas Deuermeier, António JS Fernandes, Filipe ML Figueiredo, Elvira Fortunato, and Florinda M Costa. Laser-induced graphene from paper by ultraviolet irradiation: humidity and temperature sensors. *Advanced Materials Technologies*, 7(7):2101311, 2022.

[76] Yanan Wang, Yong Wang, Peipei Zhang, Fu Liu, and Sida Luo. Laser-induced freestanding graphene papers: A new route of scalable fabrication with tunable morphologies and properties for multifunctional devices and structures. *Small*, 14(36):1802350, 2018.

[77] Yeongju Jung, JinKi Min, Joonhwa Choi, Junhyuk Bang, Seongmin Jeong, Kyung Rok Pyun, Jiyong Ahn, Yeongtak Cho, Seunghun Hong, Sukjoon Hong, et al. Smart paper electronics by laser-induced graphene for biodegradable real-time food spoilage monitoring. *Applied Materials Today*, 29:101589, 2022.

[78] Rodrigo Abreu, Maykel dos Santos Klem, Tomás Pinheiro, Joana Vaz Pinto, Neri Alves, Rodrigo Martins, Emanuel Carlos, and Joao Coelho. Direct laser writing of mnox decorated laser-induced graphene on paper for sustainable microsupercapacitor fabrication. *FlatChem*, 46:100672, 2024.

[79] Sathaniswarman Remesh, Narasimhaa Naidu Loganathan, Veeradasan Perumal, Mark Ovinis, Saravanan Karuppanan, Thomas Nesakumar Jebakumar Immanuel Edison, Pandian Bothi Raja, Mohamad Nasir Mohamad Ibrahim, Natarajan Arumugam, and Raju Suresh Kumar. A high performance selectively grown nano-octahedral mn3o4 on lignin derived laser scribed graphene for microsupercapacitor applications. *Journal of Energy Storage*, 77:109920, 2024.

[80] Hanwen Zhang, Yisheng Sun, Qianwei Li, and Caixia Wan. Upgrading lignocellulose to porous graphene enabled by deep eutectic solvent pretreatment: insights into the role of lignin and pseudo-lignin. *ACS Sustainable Chemistry & Engineering*, 10(35):11501–11511, 2022.

[81] Samuel Katwesigye, Mohamed E El-Khouly, Nieves López-Salas, and Ahmed SG Khalil. Value-added utilization of biowaste-derived lignin towards the synthesis of oxygen-enriched hierarchical laser-induced graphene and its application as a micro-supercapacitor. *Journal of Energy Storage*, 105:114752, 2025.

[82] J Rinne, O Seffer, S Nothdurft, J Hermsdorf, S Kaierle, and L Overmeyer. Investigations on the weld metal composition and associated weld metal cracking in laser beam welded steel copper dissimilar joints. *Journal of Materials Processing Technology*, 296:117178, 2021.

[83] Kyunghyun Kim and Jung-Il Choi. Effect of cell-to-cell variation and module configuration on the performance of lithium-ion battery systems. *Applied Energy*, 352:121888, 2023.

[84] Rui FV Sampaio, Maximilian FR Zwicker, João PM Pragana, Ivo MF Bragança, Carlos MA Silva, Chris V Nielsen, and Paulo AF Martins. Busbars for e-mobility: State-of-the-art review and a new joining by forming technology. *Mechanical and industrial engineering: Historical aspects and future directions*, pages 111–141, 2021.

[85] Mélanie Despeisse, Björn Johansson, Jon Bokrantz, Greta Braun, Arpita Chari, Xiaoxia Chen, Qi Fang, Clarissa A González Chávez, Anders Skoogh, Johan Stahre, et al. Battery production systems: state of the art and future developments. In *IFIP International Conference on Advances in Production Management Systems*, pages 521–535. Springer, 2023.

[86] P Jeno Paul, P Anitha, S Akash, Alex Shaju, Antony Joy, and Erin Xavier Dcoutho. Design and development of triple energy storage system (tess) for electric vehicle application. In *2024 Second International Conference on Smart Technologies for Power and Renewable Energy (SPECon)*, pages 1–6. IEEE, 2024.

[87] Björn Johansson, Mélanie Despeisse, Jon Bokrantz, Greta Braun, Huizhong Cao, Arpita Chari, Qi Fang, Clarissa A González Chávez, Anders Skoogh, Henrik Söderlund, et al. Challenges and opportunities to advance manufacturing research for sustainable battery life cycles. *Frontiers in Manufacturing Technology*, 4:1360076, 2024.

[88] Joddumahanthi Vijaychandra and Łukasz Knypiński. A comprehensive review on challenges and possible solutions of battery management systems in electric vehicles. *2024 Progress in Applied Electrical Engineering (PAEE)*, pages 1–6, 2024.

[89] Bastian Mayer, Michael Schier, and Horst E Friedrich. Stand-alone battery thermal management for fast charging of electric two wheelers—integrated busbar cooling. *World Electric Vehicle Journal*, 10(2):37, 2019.

[90] Orhan Kalkan. Thermal performance improvement of an air-cooled 18650 nmc battery module: A novel busbar design that acts as a turbulator. *Journal of Energy Storage*, 88:111613, 2024.

[91] Omkar Mypati, Tariq Anwaar, Desham Mitra, Surjya Kanta Pal, and Prakash Srirangam. Characterization and modelling of al and cu busbar during charging and discharging of li-ion battery for electric vehicles. *Applied Thermal Engineering*, 218:119239, 2023.

[92] Prashant Kumar Choudhary, Shiv Chauhan, Raja Chengalvarayan, and Ranga Srinivas Gunti. Study on optimization of ultrasonic welding process parameters of al-cu bimetallic busbar for use in battery electric vehicle (ev). In *2023 IEEE International Transportation Electrification Conference (ITEC-India)*, pages 1–10. IEEE, 2023.

[93] Nikhil Kumar, Iain Masters, and Abhishek Das. In-depth evaluation of laser-welded similar and dissimilar material tab-to-busbar electrical interconnects for electric vehicle battery pack. *Journal of Manufacturing Processes*, 70:78–96, 2021.

[94] Vasco Basto Gomes, Mohammad Mehdi Kasaei, Ricardo JC Carbas, Eduardo AS Marques, and Lucas FM da Silva. A new joining by forming process for busbar-prismatic cell interconnections in electric vehicle batteries. *The International Journal of Advanced Manufacturing Technology*, pages 1–28, 2025.

[95] Abhishek Das, Anup Barai, Iain Masters, and David Williams. Comparison of tab-to-busbar ultrasonic joints for electric vehicle li-ion battery applications. *World Electric Vehicle Journal*, 10(3):55, 2019.

[96] Roman Gr Maev, Volf Leshchynsky, Emil Strumban, Mircea Pantea, Brian J Robert, and Thomas P Brackett. Tab-to-busbar interconnects formed by dual flow cold spraying. In *International Thermal Spray Conference*, volume 84536, pages 597–603. ASM International, 2023.

[97] Shun-bo Zhang, Fen Nie, Jin-peng Cheng, Han Yang, and Qiang Gao. Optimizing the air flow pattern to improve the performance of the air-cooling lithium-ion battery pack. *Applied Thermal Engineering*, 236:121486, 2024.

[98] Abhishek Das, TR Ashwin, and Anup Barai. Modelling and characterisation of ultrasonic joints for li-ion batteries to evaluate the impact on electrical resistance and temperature raise. *Journal of Energy Storage*, 22:239–248, 2019.

[99] Tobias Werling, Peter Geuting, Patrick Höschele, Christian Ellersdorfer, and Wolfgang Sinz. Investigation of the electro-mechanical behavior of automotive high voltage busbars under combined electrical load with varying indenter geometry and environmental conditions. *Journal of Energy Storage*, 32:101861, 2020.

[100] Iqbal Husain. *Electric and hybrid vehicles: design fundamentals*. CRC press, 2021.

[101] Mohsen Soori, Behrooz Arezoo, and Roza Dastres. Digital twin for smart manufacturing, a review. *Sustainable Manufacturing and Service Economics*, 2:100017, 2023.

[102] Luca Lattanzi, Roberto Raffaeli, Margherita Peruzzini, and Marcello Pellicciari. Digital twin for smart manufacturing: A review of concepts towards a practical industrial implementation. *International Journal of Computer Integrated Manufacturing*, 34(6):567–597, 2021.

[103] Chris Schwarz and Ziran Wang. The role of digital twins in connected and automated vehicles. *IEEE Intelligent Transportation Systems Magazine*, 14(6):41–51, 2022.

[104] Dimitrios Piromalis and Antreas Kantaros. Digital twins in the automotive industry: The road toward physical-digital convergence. *Applied System Innovation*, 5(4):65, 2022.

[105] Ahmet Mete Muslu, Vanessa Smet, and Yogendra Joshi. Multi-physics modeling of a power electronics package with integrated cooling. In *2021 27th International Workshop on Thermal Investigations of ICs and Systems (THERMINIC)*, pages 1–6. IEEE, 2021.

[106] Chenxi Ling, Leyu Wang, Cing-Dao Kan, and Chi Yang. Thermal–electrical–mechanical coupled finite element models for battery electric vehicle. *Machines*, 12(9):596, 2024.

[107] Omri Tayyara. *Multi-Scale Thermal Design and Optimization of High-Power Converters for Electric Vehicle Fast Chargers*. PhD thesis, University of Toronto (Canada), 2022.

[108] Riccardo Torchio, F Conte, A Martin, N Bianchi, M De Soricellis, F Toso, F Pase, M Scarpa, M Filippini, M Lurtz, et al. Design and experimental validation of a multiphysics twin of a high voltage ev motor. *IEEE Transactions on Transportation Electrification*, 2024.

[109] Alexander Fill, Tobias Mader, Tobias Schmidt, Arber Avdyli, Mike Kopp, and Kai Peter Birke. Experimental investigations on current and temperature imbalances among parallel-connected lithium-ion cells at different thermal conditions. *Journal of Energy Storage*, 51:104325, 2022.

[110] Nasim Saber, Christiaan Petrus Richter, and Runar Unnthorsson. Review of thermal management techniques for prismatic li-ion batteries. *Energies*, 18(3):492, 2025.

[111] Aravind Venugopal and Femi Robert. Laminated busbar optimization concerning physical aspects, materials, and structural modifications. In *2022 International Conference on Power, Energy, Control and Transmission Systems (ICPECTS)*, pages 1–5. IEEE, 2022.

[112] KW See, Guofa Wang, Yong Zhang, Yunpeng Wang, Lingyu Meng, Xinyu Gu, Neng Zhang, KC Lim, L Zhao, and Bin Xie. Critical review and functional safety of a battery management system for large-scale lithium-ion battery pack technologies. *International Journal of Coal Science & Technology*, 9(1):36, 2022.

[113] Lukas Radomsky, Robert Keilmann, Dirk Ferch, and Regine Mallwitz. Challenges and opportunities in power electronics design for all-and hybrid-electric aircraft: a qualitative review and outlook. *CEAS Aeronautical Journal*, 15(4):751–764, 2024.

[114] Saranarayanan Ramachandran and AK Lakshminarayanan. An insight into microstructural heterogeneities formation between weld subregions of laser welded copper to stainless steel joints. *Transactions of Nonferrous Metals Society of China*, 30(3):727–745, 2020.

[115] Chi-Hsuan Lin, Wei-Chen Huang, Yu-Cheng Ke, and Jenn-Ming Song. Electrochemical analysis of surface oxide layers of various copper films in microelectronics. In *2021 IEEE CPMT Symposium Japan (ICSJ)*, pages 61–64. IEEE, 2021.

[116] Kenza Kamli, Zakaria Hadef, Baghdadi Chouial, and Bouzid Hadjoudja. Thickness effect on electrical properties of copper oxide thin films. *Surface Engineering*, 35(1):86–90, 2019.

[117] Efe Savran, Esin Karpat, and Fatih Karpat. Energy-efficient anomaly detection and chaoticity in electric vehicle driving behavior. *Sensors*, 24(17):5628, 2024.

[118] Bi Wu, Shi Qiu, and Wenhe Liu. Addressing sensor data heterogeneity and sample imbalance: A transformer-based approach for battery degradation prediction in electric vehicles. *Sensors*, 25(11):3564, 2025.

[119] S Meenakshi Ammal, M Kathiresh, and R Neelaveni. Artificial intelligence and sensor technology in the automotive industry: An overview. *Automotive embedded systems: key technologies, innovations, and applications*, pages 145–164, 2021.

[120] Heba M Fahmy, Hagar Ismail Helmy, Fatma Elzahraa Ali, Nourhan Essam Motei, and Marwa Saeed Fathy. Industrial applications of sensors. In *Handbook of Nanosensors: Materials and Technological Applications*, pages 1–34. Springer, 2023.

[121] Chukwulenwenwa John Orie. Sensor technologies perception for intelligent vehicle movement systems on nigeria road network. In *The Colloquium*, volume 10, pages 194–208, 2022.

[122] Fernando Molano Ortiz, Matteo Sammarco, Luis Henrique MK Costa, and Marcin Detyniecki. Applications and services using vehicular exteroceptive sensors: A survey. *IEEE Transactions on Intelligent Vehicles*, 8(1):949–969, 2022.

[123] De Jong Yeong, Gustavo Velasco-Hernandez, John Barry, and Joseph Walsh. Sensor and sensor fusion technology in autonomous vehicles: A review. *Sensors*, 21(6):2140, 2021.

[124] George-Călin Seriţan, Costel-Ciprian Raicu, and Bogdan-Adrian Enache. Single-wire control and fault detection for automotive exterior lighting systems. *Sensors*, 23(14):6521, 2023.

[125] Raj Krishan Ghosh, Anindya Banerjee, Prasenjit Aich, Deborsi Basu, and Uttam Ghosh. Intelligent iot for automotive industry 4.0: Challenges, opportunities, and future trends. *Intelligent Internet of Things for healthcare and industry*, pages 327–352, 2022.

[126] Dauren Dzhambulovich Issabekov, Zhassulan Bakutzhanovich Mussayev, Vadim Pavlovich Markovskiy, Aleksandr Petrovich Kislov, and Dariya Sansyzbayevna Urazalimova. Reed switch overcurrent protection: New approach to design. *Energies*, 17(11):2481, 2024.

[127] Nicolae Ioan Gross and Paul Svasta. Current implementations of fluid level sensors from an automotive safety perspective. In *2022 IEEE 28th International Symposium for Design and Technology in Electronic Packaging (SIITME)*, pages 209–213. IEEE, 2022.

[128] Lowell Welburn, Amir Milad Moshref Javadi, Luong Nguyen, and Salil Desai. Prospects and trends in biomedical microelectromechanical systems (mems) devices: A review. *Biomolecules*, 15(6):898, 2025.

[129] Konrad T Kloch, Pawel Kozak, and Andrzej Mlyniec. A review and perspectives on predicting the performance and durability of electrical contacts in automotive applications. *Engineering Failure Analysis*, 121:105143, 2021.

[130] Jangmuk Lim, Hansu Kim, Jae Kyun Kim, Sung Joon Park, Tae Hee Lee, and Sang Won Yoon. Numerical and experimental analysis of potential causes degrading contact resistances and forces of sensor connectors for vehicles. *IEEE Access*, 7:126530–126538, 2019.

[131] ME Kalinkina, AG Korobeynikov, OI Pirozhnikova, NA Shmakov, and VL Tkalich. Designing of reed switches for sensors and security alarm devices. In *IOP Conference Series: Materials Science and Engineering*, volume 1100, page 012009. IOP Publishing, 2021.

[132] Zherui Zhang, Yichen Wu, Lingbin Xie, Xianjun Zhu, and Longlu Wang. Engineering group vi transition metal dichalcogenides for designing various sensors. *Advanced Materials Technologies*, 10(11):2402018, 2025.

[133] Kamrul Hassan, Tran Thanh Tung, Pei Lay Yap, Hadi Rastin, Nathan Stanley, Md Julker Nine, and Dusan Losic. Fractal design for advancing the performance of chemoresistive sensors. *ACS sensors*, 6(10):3685–3695, 2021.

[134] Sourov Roy, ANM Wasekul Azad, Somen Baidya, Mohammed Khorshed Alam, and Faisal Khan. Powering solutions for biomedical sensors and implants inside the human body: A comprehensive review on energy harvesting units, energy storage, and wireless power transfer techniques. *IEEE Transactions on Power Electronics*, 37(10):12237–12263, 2022.

[135] Longfei Zhou, Jenna Miller, Jeremiah Vezza, Maksim Mayster, Muhammad Raffay, Quentin Justice, Zainab Al Tamimi, Gavyn Hansotte, Lavanya Devi Sunkara, and Jessica Bernat. Additive manufacturing: a comprehensive review. *Sensors*, 24(9):2668, 2024.

[136] Yijie Jiang, Md Nurul Islam, Rui He, Xiaozhou Huang, Peng-Fei Cao, Rigoberto C Advincula, Narendra Dahotre, Pei Dong, H Felix Wu, and Wonbong Choi. Recent advances in 3d printed sensors: materials, design, and manufacturing. *Advanced Materials Technologies*, 8(2):2200492, 2023.

[137] R Anumodh, Balbir Singh, and Mohammad Zuber. Morphing applications in automobiles: a review. *International Journal of Vehicle Design*, 85(1):1–31, 2021.

[138] Mihailo Jovanović, Tomás de J Mateo Sanguino, Milanko Damjanović, Milena Đukanović, and Nikolas Thomopoulos. Driving sustainability: carbon footprint, 3d printing, and legislation concerning electric and autonomous vehicles. *Sensors*, 23(22):9104, 2023.

[139] Laura Tronci and Assunta Marrocchi. Green gold: Prospects of lignin in organic electronics and bioelectronics. *RSC Sustainability*, 2(12):3769–3781, 2024.

[140] Adebayo Olusegun Aderibigbe, Peter Efosa Ohenhen, Nwabueze Kelvin Nwaobia, Joachim Osheyor Gidiagba, and Emmanuel Chigozie Ani. Advanced sensing techniques in electro-mechanical systems: surveying the rise of smart sensors and their implications for system robustness. *Engineering Science & Technology Journal*, 4(6):323–340, 2023.

[141] Md Merajul Islam. Lignocellulosic biomass-based materials: a promising resource for viable energy storage. *Sustainable Energy & Fuels*, 8(9):1823–1871, 2024.